Dissertation zur Erlangung des Doktorgrades
an der Fakultät für Geowissenschaften der
Ludwig-Maximilians-Universität München

Deformation and reactions in mylonitic pegmatites from the Austroalpine basement south of the western Tauern Window

vorgelegt von:

Felix Hentschel

München

11. September 2019

Erstgutachterin:	Prof. Dr. Claudia A. Trepmann
Zweitgutachter:	PD Dr. Thomas Kunzmann
Mündliche Prüfung:	06.02.2020

Abstract

The fabric of granitoid rocks deformed at greenschist-facies conditions is of great importance, as it often records episodic deformation and metamorphic reactions associated with the seismic cycle in the continental crust. These rocks are mainly composed of feldspar and quartz and thus the deformation behavior of these minerals and their interplay is crucial for our understanding of crustal rheology.

In this dissertation mylonitic pegmatites from the Austroalpine basement south of the western Tauern Window were sampled and analyzed to evaluate the interplay between deformation and accompanying reactions at greenschist-facies conditions. Additionally, the quartz microstructures from a major shear zone in this area, the Defereggen-Antholz-Vals (DAV) shear zone, are compared with quartz microstructures from the Silvretta basal thrust.

In the first part the microstructure and -texture of albite and K-feldspar from these mylonitic pegmatites were investigated by light microscopy, electron microscopy and electron backscatter diffraction to evaluate feldspar deformation mechanisms at greenschist facies conditions. The mylonites are characterized by alternating quartz and albite layers, surrounding K-feldspar and tourmaline porphyroclasts. K-feldspar is mostly deformed by fracturing, with the fractures being sealed by polyphase aggregates indicating dissolution-precipitation creep. Additionally, K-feldspar is replaced by albite at its rim, forming cuspate phase boundaries. Albite porphyroclasts are replaced at boundaries parallel to the foliation by fine-grained monophase albite aggregates of small strain-free new grains mixed with deformed fragments. As indications of effective dislocation climb and dynamic recovery are missing, this grain size reduction is interpreted to be the effect of coupled dislocation glide and fracturing. This strain-induced replacement and subsequent growth results, together with granular flow, in the monophase albite layers. The associated quartz layers show characteristics of dislocation creep by the presence of subgrains, undulatory extinction and sutured grain boundaries. Observations indicate that grain size reduction by strain-induced replacement of albite (associated dislocation glide and microfracturing, i.e. low-temperature plasticity) followed by growth and granular flow, simultaneous with dislocation creep of quartz, are dominating in the formation of the mylonitic microstructure.

The second part is concerned with replacement reactions that accompany deformation at greenschist-facies conditions. Variscan monazite (Mnz1) and xenotime (Xen1) partially break down into apatite-allanite/epidote coronas. In the corona core, monazite and xenotime single crystals show domains with different composition and age. Monazite (Mnz1) and xenotime (Xen1) dating by electron microprobe (EPM) reveals an age of 250-287 Ma, representing the magmatic age of the pegmatites. These are partly replaced by secondary monazite (Mnz2) and xenotime (Xen2), yielding age populations of $\sim$ 200 Ma and of 60 $\pm$ 20 Ma. The same crystallographic orientation of primary and secondary monazite and xenotime indicates interface-coupled dissolution-precipitation reactions. Allanite U/Th-Pb dating by laser ablation inductively coupled mass spectrometry (LA-ICP-MS) in the corona revealed an age of $\sim$ 60 Ma, indicating that the replacement reactions are associated to corona formation. The corona core is surrounded by an inner zone of isometric apatite grains, enriched in light rare earth elements (LREE-Ap), surrounded by prismatic allanite (Aln), epidote enriched in heavy rare earth elements (HREE-Ep) and REE-poor epidote (Ep) grains. Compared to coronas around monazite,

apatite has higher HREE contents (HREE-Ap) and no allanite occurs in coronas around xenotime. The amount of replacement is low in monazite inclusions in tourmaline but high within the mylonitic foliation. This dependence of the degree of replacement on the local microfabric indicates that fluid availability along grain boundaries in the matrix and cracks controls the reaction advancement, by allowing the elementary mass transfer required for the corona reaction (e.g. input of Ca, Al, Si, Fe). The shape of the coronas aligned within the foliation of the pegmatites and the deflected foliation around the coronas, without the outer rim of prismatic epidote showing signs of deformation, indicate that the main stage of corona formation took place during deformation. Thus, the corona microstructure documents replacement reactions of a single reactant into multiple distinct mineral growth zones by dissolution and precipitation processes at non-isostatic, greenschist-facies conditions, which prevailed in the area to the north of the DAV at the inferred time of $\sim$ 60 Ma. The reactions ceased before being completed and REE gradients within single grains, within the corona and on thin section scale are preserved. Therefore, restricted and/or episodic transport of REE in the fluid phase and/or availability of fluid are suggested.

The last part pertains to the microfabric of quartz in shear zones, which records a switch from low-temperature plasticity at transient high stress to recrystallization at relaxing stresses at greenschist facies conditions. For that, rocks from two shear zones from the Austroalpine basement, the DAV shear zone and the Silvretta basal thrust, were analyzed. In both examples the development of new grains happened dominantly by subgrain rotation and subsequent strain-induced grain-boundary migration in areas of localized high strain developed during initial low-temperature plasticity. The findings suggest that new grains develop at almost random crystallographic orientations at fast rates of stress relaxation (i.e. at low stress), as indicated by recrystallized quartz zones in the Silvretta fault rocks. In contrast, at slow rates of stress relaxation, new grains develop at moderately high stresses with crystallographic preferred orientations characterized by a high Schmid factor for basal-<a> glide, as indicated by vein quartz samples from the DAV shear zone. Both recorded histories with transient peak stresses and different rates of stress relaxation are interpreted to be related to seismic activity of the fault systems.

The deformation and reaction fabric in the analyzed samples all record episodic processes, consistent with deformation just below the seismogenic layer in the continental crust. Feldspar and quartz both show microfabrics indicative of low-temperature plasticity, highlighting the non-steady state nature of their deformation.

Contents

1 Introduction

1.1 Motivation

The seismogenic zone is that region of the lithosphere where earthquakes can nucleate (e.g. Marone & Scholz, 1988; Scholz, 1998, 2002). The base of the seismogenic zone in the continental crust is coinciding with the temperature-depth region characterized by greenschist-facies metamorphic conditions and marks the transition from dominantly pressure-dependent, localized deformation ("schizosphere", Scholz, 2002) to temperature and strain-rate-controlled, distributed deformation ("plastosphere", Scholz, 2002) for continental crustal rocks. This transition occurs at approximately 300 ± 50 °C or 15–20 km (Scholz, 1998), corresponding to the onset of crystal plasticity of quartz. During earthquakes, i.e. during coseismic slip in the schizosphere, very high stresses are induced in the uppermost plastosphere (Trepmann, 2002; Ellis & Stöckhert, 2004), followed by postseismic relaxation with decaying stresses (Nüchter & Ellis, 2010). The deformation behavior of granitoid rocks and their main rock-forming minerals, feldspar and quartz, at greenschist-facies conditions is therefore of fundamental importance.

Whereas the deformation behavior of quartz at these conditions has been well investigated in the past (e.g. Hirth & Tullis, 1994; Stöckhert et al., 1999; Trepmann & Stöckhert, 2003; Trepmann et al., 2007; Kjøll et al., 2015), the feldspar deformation behavior at greenschist-facies conditions, especially related to the seismic cycle, is much less understood. The deformation behavior of both K-feldspar and plagioclase is difficult to assess, because both minerals are crystallographically and chemically very versatile (see Chapter 2). Compared to compositionally and structurally more restricted minerals like quartz, the response of feldspars to stress shows a complex interplay between brittle, plastic and dissolution-precipitation processes (e.g. Tullis & Yund, 1987; Mehl & Hirth, 2008).

Especially, the role of dislocation creep of feldspar for the deformation at greenschist-facies conditions is poorly understood. Because diffusion in feldspars is relatively slow (e.g. Korolyuk & Lepezin, 2009), pure crystal-plastic behavior, for which dislocation climb is crucial, should not be active at greenschist-facies conditions (e.g. Tullis & Yund, 1987) and in experiments it has been found to be dominant only at T > 900 °C (Rybacki & Dresen, 2004). Nonetheless feldspar-rich mylonites, deformed at greenschist-facies conditions, often show features that are usually associated with dislocation creep, e.g. porphyroclasts surrounded by small grains (e.g. Tullis & Yund, 1985) and monophase layers (e.g. Stünitz & Fitz Gerald, 1993). Furthermore, crystallographic-preferred orientations (CPOs) of fine-grained aggregates (usually taken to indicate dislocation creep) of feldspar have been reported to be related to inheritance (Jiang et al., 2000) or crystallographically preferred dissolution-precipitation/growth (Menegon et al., 2008).

Episodic deformation related to the seismic cycle has been observed to trigger metamorphic reactions and dissolution-precipitation processes (e.g. Wintsch & Yeh, 2013; Putnis et al., 2017). This is expected, as seismic deformation leads to localized and episodic fluid availability (e.g. Küster & Stöckhert, 1999; Nüchter & Stöckhert, 2008; Billia et al., 2013). The interplay between episodic deformation and reactions, yet, is not well understood.

Mylonitic pegmatites from the Austroalpine basement to the south of the western Tauern Window were chosen to investigate the deformation and accompanying reactions of granitoids under greenschist-facies conditions. These pegmatites were used because they were deformed at greenschist-facies conditions during the Alpine orogeny (Stöckhert, 1987; Mancktelow et al., 2001). Additionally, they are mineralogically relatively simple, consisting mainly of albitic plagioclase, K-feldspar, quartz and white mica and show a wide range of feldspar deformation microstructures. Deformation accompanying mineral reactions in these pegmatites are indicated by the occurrence of coronas around monazite and xenotime, which further gives the possibility to constrain the age of deformation.

These are the aims of the research presented in this thesis:

1. The correlation of the characteristic microstructures of feldspar to specific processes responsible for their formation (Chapter 5). Additionally, the discussion of the rheology of these rocks and the implications for the local deformation history.
2. To evaluate metamorphic replacement reactions of monazite and xenotime, foremost the formation of corona microstructures and to establish the structural relationship between these and the mylonitic foliation of the samples (Chapter 6). Dating of the corona-forming minerals will be used to shed light on the age of deformation in the studied area, which still remains unclear (e.g. Mancktelow et al., 2001).
3. To assess the stress history of the Defereggen-Antholz-Vals (DAV) shear zone, as recorded by quartz microfabrics (Chapter 7). The results will be compared to the stress history of the Silvretta basal thrust.

1.2 Structure of this thesis

After this introduction, some background about feldspars is given in chapter 2. Chapter 3 presents an introduction to the geology of the Austroalpine basement south of the western Tauern Window and the Silvretta nappe. As most of the field work was done in the former area, the geologic overview on it is more in depth. All used analytical methods are presented in chapter 4.

The research presented in this thesis (chapters 5 to 7) consists of studies that are already published in or have been submitted to peer-reviewed publications. Chapter 5 is concerned with the deformation behaviour of feldspars at greenschist-facies conditions and is based mainly on mineralogical and textural analysis of mylonitic pegmatites from the Austroalpine basement south of the western Tauern Window. This study is published as Hentschel et al. (2019). Chapter 6 presents a study on corona structures developed around monazite and xenotime in the same deformed pegmatites already presented in chapter 5. Here, geochemical, microstructural and geochronological techniques are used to unravel how and when these structures formed. In chapter 7 quartz microstructures from two different fault zones, one from the Austroalpine basement south of the western Tauern Window and one from the Silvretta nappe, are analysed by textural analysis and transmission electron microscopy (TEM). This study is published as Trepmann et al. (2017). Chapter 8 is a conclusion of all presented research.

1.2.1 Author contributions

Chapter 5:

"Hentschel, F.; Trepmann, C.; Janots, E. (2019): Deformation of feldspar at greenschist facies conditions – the record of mylonitic pegmatites from the Pfunderer Mountains, Eastern Alps, *Solid Earth*, 10(1): 95–116, doi: 10.5194/se-10-95-2019".

FH was mainly responsible for data acquisition and interpretation. The field work was done by FH. FH and CT developed the underlying conceptual idea of the study. FH prepared the figures and the manuscript with contributions from EJ and CT.

Chapter 6:

"Hentschel, F.; Janots, E.; Trepmann, V.; Magnin, V.; Lanari, P. (in prep): Coronas around monazite and xenotime recording incomplete replacement reactions and compositional gradients during greenschist facies metamorphism and deformation".

FH, EJ and CT designed this study. The field work was done by FH. Microprobe dating of monazite and xenotime was done by VM, FH and EJ. PL performed the allanite dating. FH prepared the figures and the manuscript with contributions from EJ and CT.

Chapter 7:

"Trepmann, C.; Hsu, C.; Hentschel, F.; Döbler, K; Schneider, C; Wichmann, V. (2017): Recrystallization of quartz after low-temperature plasticity – The record of stress relaxation below the seismogenic zone. *Journal of Structural Geology*, 95: 77–92, doi: 10.1016/j.jsg.2016.12.004".

CT and FH designed the study. Samples were taken by KD, SC, WV and CT. Microfabric analyses were preformed by CT, CH and FH. The manuscript was compiled by CT and FH.

2 Properties of feldspars

2.1 Crystallography

The different feldspar minerals are low-symmetry framework silicates. Cavities inside their tetrahedral framework are filled with cations, mostly K^+, Na^+ and Ca^{2+}. In all feldspars (Si, Al)-tetrahedrons form four-membered rings, which in turn connect to layers and to so called crankshafts in three dimensions (Fig. 2.1). The general high-temperature feldspar structure has monoclinic space group C2/m and two distinguishable tetrahedral sites T_1 and T_2 (e.g. Putnis, 2008). Two different distortions happen to this structure at lower temperatures:

1. The smaller cations Na and Ca cannot support the framework structure at lower temperatures. This leads to a collapse of the framework and lowering of the symmetry to triclinic. Only albite-rich plagioclase can crystallize in the monoclinic HT-structure. More Ca-rich plagioclases are always triclinic up to their melting temperature. This collapse is displacive and instantaneous. Potassium on the other hand can fully stabilize the framework at all temperatures (e.g. Ribbe, 1983).
2. Al-Si ordering leads to further distinction of tetrahedral sites and the loss of symmetry elements. For K-feldspar this leads to the triclinic space group $C\bar{1}$. Plagioclase either keeps space group $C\bar{1}$ (albitic) or transforms into $I\bar{1}$ (Ca-rich). As this ordering involves diffusion, it is a much slower process compared to the structural collapse (e.g. Ribbe, 1983).

These two structural distortions are not independent of each other (i.e. they are coupled). For example, albite should transform to C2/m if heated above 980 °C, but any degree of order present would prevent this. As ordering is much slower it is the rate controlling process during the formation of low-temperature crystal structures in feldspars.

2.1.1 K-Feldspar $KAlSi_3O_8$

The potassium cation in K-feldspar is big enough to support the framework structures also at low temperatures (e.g. Kroll & Ribbe, 1983). Al-Si ordering therefore is the more important structural process. It is not possible to order 1 Al and 3 Si over two tetrahedral sites. The needed distinction of four different sites leads to loss of the mirror plane and the diad axis and the transformation from C2/m to $C\bar{1}$. This transformation starts at temperatures below 450 °C and begins with local, distributed ordering. The overall crystal structure is still monoclinic and such a K-feldspar is usually called orthoclase. Complete ordering finally produces microcline feldspar. The C2/m to $C\bar{1}$ transformation also produces the cross-hatched twinning typical for microcline feldspars.

2.1.2 Plagioclase

The real structure of plagioclase is determined by the interplay between the structural collapse around the small (Na, Ca) cation and Al-Si ordering (e.g. Smith, 1983a). The temperature of the structural collapse increases with increasing An-content. In pure albite it happens at 980 °C. Ordering begins at $\sim$ 700 °C, but does not change symmetry

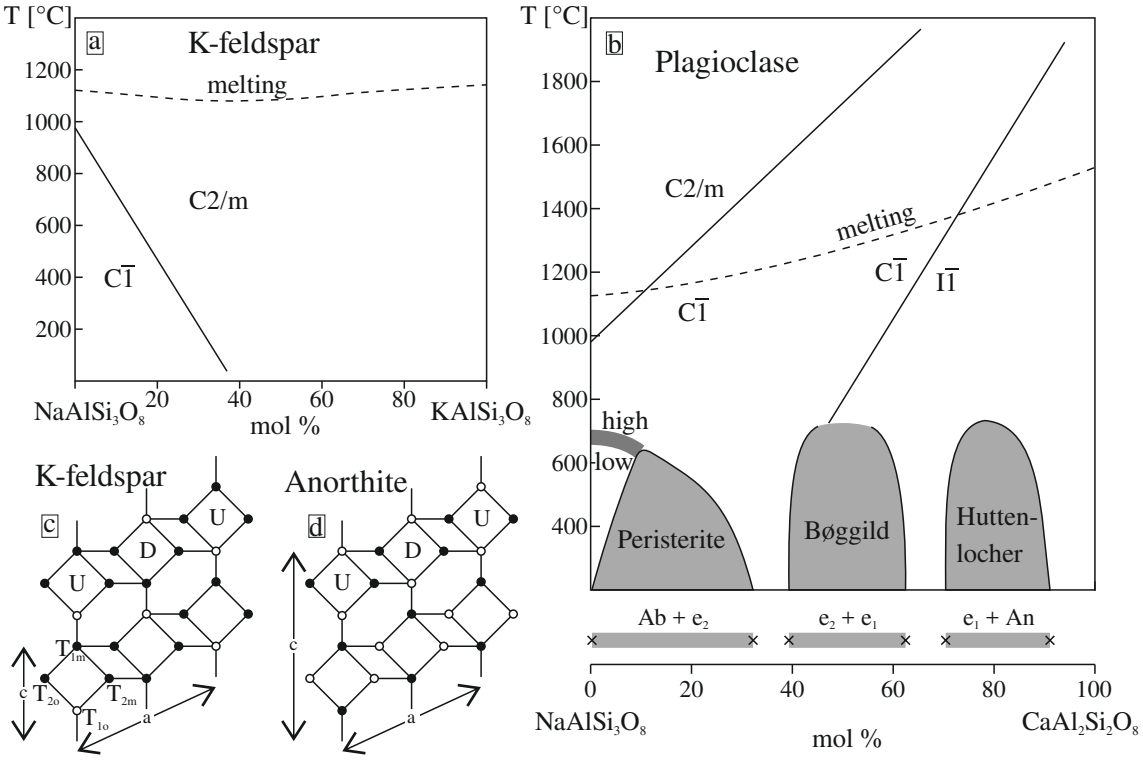

Figure 2.1: (a) Phase diagram of K-feldspars, showing the symmetry of T-dependent modifications (modified after Putnis, 2008). **(b)** Phase diagram of plagioclase feldspars, showing the symmetry of T-dependent modifications and low-temperature two-phase fields. (c, d) Structures of K-feldspar and anorthite

as it was already lowered by structural collapse. Ordered albite is called low albite and is the standard modification of $NaAlSi_3O_8$ found in plutonic and metamorphic rocks. Pure anorthite has an almost fully ordered structure, as disorder would lead to more Al-O-Al bonds at higher Al:Si ratios. In between, the structure changes from $C\bar{1}$ for the Na-rich side of the phase diagram towards $I\bar{1}$ for the Ca-rich side. No perfect ordering schemes for intermediate plagioclases exist that can reconcile Al-Si & Na-Ca ordering with local charge balance. Therefore, incommensurate structures, which provide compromises to these requirements, with wavelengths of about 50 Å, exist.

Two such structures seem to be energetically or kinetically favoured in intermediate plagioclases, e_1 & e_2. Most natural plagioclases below 700 °C form submicroscopic intergrowths between either albite & e_2 ("Peristerite intergrowth"), e_1 & e_2 ("Bøggild intergrowth") and e_1 & anorthite ("Huttenlocher intergrowth"). Smith (1983a) suggests that only the ordered structures of An_0 & An_{100} are stable at low temperatures and all intermediate structures regularly found are kinetically stabilized.

2.2 Chemistry

The general formula of feldspars is AT_4O_8, where T = Si, Al and A = K, Na in Alkali feldspars and A = Na, Ca in Plagioclase feldspars (e.g. Smith, 1983b). The A cation charge-balances the aluminosilicate framework. Alkali feldspars usually exsolve into Na-

rich and K-rich parts upon cooling, dependent on the cooling rate, forming exsolution lamellae (Fig. 2.2). Exsolution happens either by heterogeneous nucleation or spinodal exsolution. Exsolution in plagioclases is more complex and involves albite, anorthite and kinetically stable intermediate "e"-structures.

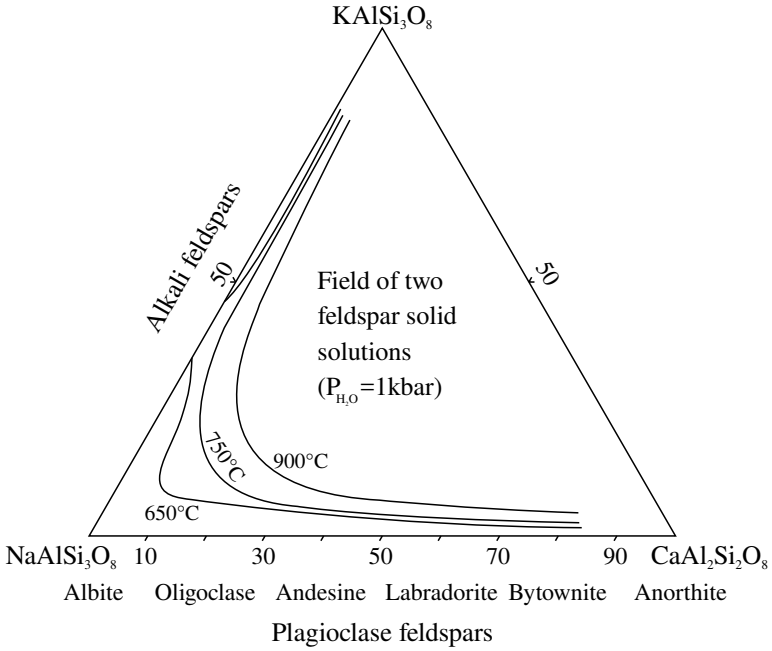

Figure 2.2: Ternary phase diagram of feldspars showing limited temperature dependent solubility (modified after Putnis, 2008).

Many plagioclases between An_2 and An_{16} occur as intergrowths of $\sim An_0$ and $\sim An_{25}$ ("Peristerite intergrowth"). This exsolution has also been observed in naturally metamorphosed albite schists, where oligoclase can form a separate phase, beginning at low metamorphic grade (see review in Smith (1983a)). The Bøggild and Huttenlocher exsolutions are more complicated and have only been described as intergrowths from very high grade metamorphic rocks (Smith, 1983a).

Apart from these main elements, the T sites can be partially occupied by B, Ga, Ge, Fe^{2+}, Fe^{3+} and Mg. Small amounts of Ti and P have been reported to enter the T sites in natural samples (Smith, 1983b). The A site can be occupied by Rb, NH_4, Cs, Sr, Pb, Ba, Eu and La. Iron enters K-feldspar only as Fe^{3+}, but in plagioclase it may be present as Fe^{3+} and Fe^{2+}, dependent on the oxygen fugacity. Feldspars with a few wt% excess of Al or Si have been synthesized. But natural samples commonly show only a very small deviation from the AT_4O_8 general formula (Smith, 1983b).

2.3 Dislocations and slip systems in plagioclase

Most albite-rich plagioclases crystallize in space group $C\bar{1}$. This structure allows for several possible Burgers vectors (Table 2.1). The frequency of dislocations usually correlates inversely with the length of its Burgers vector. b[001] is the shortest Burgers vector in the $C\bar{1}$ structure (Marshall & Mclaren, 1977; Olsen & Kohlstedt, 1984). Olsen & Kohlstedt (1984) found that [001]-screw dislocations were dominant in their analysed

samples. They also found that these screw dislocations are associated with (010)-slip planes. (010) is one of the most densely packed planes in the plagioclase structure. These observations are in agreement with many studies (experimental: e.g. Marshall & Mclaren, 1977; Stünitz et al., 2003; natural: Olsen & Kohlstedt, 1984; Montardi & Mainprice, 1987; Kruse & Stünitz, 2001) who found that (010)[001] is the dominant slip system in plagioclase feldspars. Several authors also found crystallographic preferred orientations of plagioclase aggregates that can be interpreted in terms of (010)[001]-slip, i.e. (010)-planes subparallel to the foliation and [001] parallel to the lineation in mylonites (e.g. Kruhl, 1987; Olesen, 1987; Shaocheng & Mainprice, 1988).

Table 2.1: Dislocations and slip systems in plagioclase

Dislocations		**Slip systems**			
b	$\|\|b\|\|$ in Å	Burgers vector	Slip plane	observed	sources
[001]	7.1	[001]	(010)	very often	OK, MM, SFGT
1/2[110]	7.6	1/2[110]	(001), $(1\bar{1}\bar{1})$	often	OK, MM, SFGT
$1/2[1\bar{1}0]$	7.6	[101]	(010)	rare	OK
[101]	8.1	$1/2[1\bar{1}0]$	(001), $(11\bar{1})$	rare	OK
[100]	8.2	$1/2[11\bar{2}]$	$(11\bar{1})$	rare	OK
1/2[112]	8.8	$1/2[1\bar{1}2]$	(110)	rare	OK
$1/2[1\bar{1}2]$	8.8	$1/2[1\bar{1}1]$	(011)	rare	MM
		[101]	$(10\bar{1})$	rare	MM

OK = Olsen & Kohlstedt (1984); MM = Montardi & Mainprice (1987);
SFGT = Stünitz et al. (2003)

2.3.1 Dislocation generation and movement

Deformation experiments on single crystals of plagioclase have shown that dislocations are mainly associated with fractures and deformation bands, which might represent healed microfractures (Mclaren & Pryer, 2001; Stünitz et al., 2003). During plastic deformation further dislocations are produced by the interaction of different glide systems, which leads to the formation of jogs and the multiplication of dislocations by a Frank-Read source meachanism (Montardi & Mainprice, 1987).

Dislocation glide is expected to be easier in albite than in more An-rich plagioclases, because dissociation of dislocations should not be possible in the ordered $C\bar{1}$ structure, not hindering cross slip of screw dislocations (Tullis, 1983).

2.4 Recovery and recrystallization in feldspars

Recovery means the removal or rearrangement of dislocations into ordered structures – low angle grain boundaries – to reduce the internal strain energy of a grain (e.g. Doherty et al., 1997; Passchier & Trouw, 2005). This prevents strain-hardening during deformation. To form low angle grain boundaries dislocation climb and therefore diffusion is required. NaSi $\leftrightarrow$ CaAl interdiffusion rates for plagioclase are very low (Yund, 1986;

Korolyuk & Lepezin, 2009). At the presence of water, the diffusion coefficient is several magnitudes higher, which might account for the hydrolitic weakening observed in experiments (e.g. Rybacki & Dresen, 2004). A few studies report subgrains in albite deformed at greenschist facies conditions, sometimes together with shear bands (Fitz Gerald & Stünitz, 1993; Eberlei et al., 2014). TEM studies, on the other hand, show that sufficient dislocation climb to produce subgrains has been found to be active only at temperatures from the middle amphibolite upward (e.g. White, 1975; Stünitz et al., 2003).

Gardner et al. (2017) suggest that replacement of magmatic plagioclase by one of more albite rich composition leads to the formation of growth dislocations, which can lead to the formation of subgrains and grain size reduction.

The experiments by Tullis & Yund (1985) show that feldspars may show grain boundary migration at conditions, where recovery is not active. Grain boundaries move into areas of higher dislocation density, which form during incipient microfracturing (Tullis & Yund, 1987). Ongoing deformation can then produce roundish plagioclase porphyroclasts surrounded by very fine grained recrystallized tails (Tullis & Yund, 1985). In the review of studies on natural deformed feldspar by Fitz Gerald & Stünitz (1993) however, it is noted that grain boundary migration is actually active at higher temperatures ($>$ 550 °C) than subgrain rotation. This might be because the microstructures observed by Tullis & Yund (1985) are only transient and might not be observable after high strain deformation.

Dislocation creep, i.e. dislocation glide and dislocation climb, can produce crystallographic preferred orientations (CPOs) in mineral aggregates. CPOs for feldspar have been reported from many high temperature shear zones, mainly in amphibolites and gabbros. A database of 172 CPOs is presented by Satsukawa et al. (2013). Only few studies report CPOs for plagioclase from greenschist facies shear zones. Shigematsu & Tanaka (2000) found a CPO for plagioclase that they interpret in terms of dislocation creep. They estimate temperatures to have been $<$ 500 °C during deformation, but their estimate depends only on the Ab-content of K-feldspar. The glide system they derive is not one of the known ones for plagioclase. Prior & Wheeler (1999) and Jiang et al. (2000) report CPOs of high strain albite aggregates from the Combin zone in the Western Alps, a greenschist facies shear zone. Their CPOs vary between aggregates and cannot be explained by active glide systems during dynamic recrystallization. They interpret them as inheritance from fromer porphyroclasts, though the exact mechanism of inheritance remains unclear.

2.4.1 Chemical change as a driving force for recrystallization

Many studies observe a difference in chemical composition between host and recrystallized plagioclase grains. If the rocks have been deformed at lower temperatures than the plagioclases crystallized, the equilibrium composition of recrystallized grains should be more albite-rich, a feature which is regularly observed (e.g. White, 1975; Stünitz et al., 2003; Rosenberg & Stünitz, 2003). This chemical driving force might theoretically have an influence on grain boundary mobility, when an area with the ”old” composition and higher dislocation density is consumed (Stünitz, 1998). There should be no significant

influence on subgrain rotation, because it does not produce a difference in composition. Stünitz (1998) calculated that in general, the chemical influence on grain boundary mobility is small. This small difference might have a stronger influence, if a fluid film is present at the grain boundary. In Stünitz' (1998) comparison to natural samples, the highest differences in composition between new and old grains where for grains that were formed by heterogeneous nucleation ("neocrystallization"). Stünitz (1998) considers that the driving force from the reduction in strain energy might have an impact on the ease of heterogeneous nucleation. Yund & Tullis (1991) found that recrystallization by grain boundary migration greatly enhanced the kinetics of exchange reactions between plagioclase grains of different composition.

2.5 Mechanical twinning in feldspar

Mechanical twinning in plagioclases can occur in two different ways: (1) albite twinning, with (010) as the glide plane and the projection of the b axis on (010) as the glide direction; and (2) pericline twinning, where the b axis is the glide direction and the rhombic section is the glide plane (e.g. Tullis, 1983). In the ordered low albite structure $C\bar{1}$ mechanical twinning should not be possible, as it would destroy the Si/Al-ordering. In intermediate plagioclases twinning should be easier at higher temperatures, where the structures are more disordered. Similarly, mechanical twinning K-feldspar should not be possible and has not been observed except for some unclear exceptions (Tullis, 1983).

Albite and pericline twinning should appear equally often, as the resolved shear stress is the same for any stress direction, but characterization of twinning in natural samples is difficult because of identification errors and the difficult distinction between mechanical and growth twins. Commonly cited criteria (e.g. Spry, 1969) for recognizing mechanical twins are: (1) very fine-scale polysynthetic twins, (2) bent and/or tapered twins and (3) twinning limited to certain areas of high strain, like grain boundaries.

Complete mechanical twinning of a plagioclase grain can produce up to 7 % shortening. Mechanical twinning in plagioclase is widespread but does not produce much strain and may be produced by local stress concentrations.

2.6 Grain size reduction in feldspar-rich mylonites

The formation of shear zones and related mylonitic rocks requires strain localization and is generally associated and probably dependent on a marked grain size reduction (e.g. White et al., 1980). Apart from crystal plastic mechanisms, grain size reduction of feldspar porphyroclasts mostly happens by two ways: fracturing and nucleation of new grains ("neocrystallization"). Each of these processes might happen in one rock at the same time and it has been observed that fracturing and crystal plasticity in feldspars are often interdependent (Tullis & Yund, 1987; Mclaren & Pryer, 2001). Neocrystallisation of plagioclase and/or other minerals also are enhanced by fracturing (e.g. Fitz Gerald & Stünitz, 1993).

2.6.1 Microfracturing

All feldspars have a perfect cleavage after (001) and one good cleavage after (010) (Tröger, 1982). Thus microfracturing is an important deformation mechanism for plagioclase and K-feldspar at most metamorphic conditions. There is some evidence that K-feldspar will fracture more easily than plagioclase at the same conditions (Tullis, 1983), but detailed studies are lacking.

As thermally activated mechanisms like dislocation climb are difficult in feldspars, microfracturing is especially important at low metamorphic grades. At very low temperatures, where microcracking is the dominant deformation mechanism for both quartz and feldspar, feldspar is much weaker than quartz (Tullis & Yund, 1977).

The importance of fracturing on the rheology of feldspar- and quartz-rich rocks depends on the proportions of these two minerals. If quartz is dominating recrystallized layers of quartz will usually surround relatively undeformed feldspar porphyroclasts. On the other hand, if feldspars form a stress-supporting framework, they will fracture readily and decrease in grain size. Fractures will usually form along the two good cleavages but extension and shear fractures are also observed (e.g. Andrews, 1984). Some extensional fractures in granitic mylonites might also form during cooling, as thermal expansion in feldspars is very anisotropic (Tullis, 1983).

Microfractures also provide pathways for fluids during deformation. Thus they facilitate the precipitation/neocrystallization of usually fine-grained reaction products which in turn might lead to strain weakening (e.g. Fitz Gerald & Stünitz, 1993; Menegon et al., 2013). In feldspars microfractures are often associated with dislocations and are considered to be main nucleation site for dislocations at the onset of deformation (Mclaren & Pryer, 2001; Stünitz et al., 2003). High stresses at sites of high dislocation density might in turn also faciliate microcracking. Because of these two reasons microfracturing is often observed to be important only at the onset of deformation and is often followed by other mechanisms like recrystallization (Tullis & Yund, 1992) or neocrystallization (Fitz Gerald & Stünitz, 1993).

Concentrated microfracturing ("micro-crush zones") might also lead to optically visible structures that are usually associated with crystal plastic mechanisms, like undulous extinction or shear bands (Tullis & Yund, 1992; Mclaren & Pryer, 2001; Stünitz et al., 2003). Care must thus be taken, when these microstructures are interpreted, especially for rocks deformed at low temperatures.

2.6.2 Syn-deformational reactions in deforming granitic mylonites

Syn-deformational reactions can have various influences on the rheological properties of the rocks they occur in. Most studies on this have concentrated on mechanical weakening produced by reactions. Mechanical weakening is occurring by two main mechanisms: either the product phases are mechanically weak or the smaller grain size of product phases leads to a switch in deformation mechanism to grain size sensitive mechanisms like diffusion-assisted grain boundary sliding (e.g. Handy, 1989; Rubie, 1990).

Mineral reactions happen because of chemical disequilibrium, either because of the deforming rocks moving to different P-T conditions or of an incoming fluid phase that is

not in equilibrium with the rock's mineral phases. Additionally, a fluid phase can also trigger reactions at low metamorphic conditions, which would otherwise not happen due to sluggish reaction kinetics.

K-feldspar

Several studies report the importance of such reaction weakening for both K-feldspar and plagioclase at different metamorphic conditions during deformation. Menegon et al. (2013), for example, report the nucleation of phases like amphibole and biotite during granulite facies deformation. The resulting fine-grained mixture of product phases subsequently deformed by diffusion creep to produce high strains.

Another common reaction affecting K-feldspar in deforming granitoids is the production of myrmekite. Myrmekite is an intergrowth of vermicular quartz and plagioclase (Abart et al., 2014). Its formation is thought to be promoted by the increase in permeability and subsequent fluid influx during deformation (e.g. Menegon et al., 2006). These authors also conclude that myrmekite formation contributes to reaction-softening by producing fine-grained phase mixtures. Most studies observe myrmekite during amphibolite-facies and higher conditions (e.g. Ree et al., 2005), but is has also been found as a contributing factor at greenschist facies conditions (Tsurumi et al., 2003). Care must be given when connecting myrmekite formation to deformation, as myrmekite have also been observed as a product of sub-solidus metasomatic replacement in granites (Abart et al., 2014).

The replacement of K-feldspar by albite is a widely observed reaction in deforming granitoids at low temperatures. Different types of replacement structures have been reported, which can be divided into two groups: microstructures produced by neocrystallisation of albite and ones produced by interface-coupled dissolution of K-feldspar and precipitation of albite. Neocrystallisation produces distinct albite grains without any crystallographic relationship to the replaced K-feldspar. They often appear in strings and patches inside the host grain and may be related to fractures (e.g. Fitz Gerald & Stünitz, 1993; Menegon et al., 2013). Interface-coupled dissolution-precipitation on the other hand produces different microstructures. The dissolution of the parent phase and immediate, spatially coupled precipitation of the daughter phase leads to a strong structural coherence across the reaction interface, i.e. host-control on the orientation of the new phase (Putnis, 2009). Compatible microstructures for the replacement of K-feldspar by albite have been found in natural (Plümper & Putnis, 2009) and experimental (Hövelmann et al., 2010; Norberg et al., 2011) investigations. Apart from orientation-control on the new albite, these studies have found that the new phase might be porous and contain muscovite inclusions. Norberg et al. (2011) also found associated microcracking in the K-feldspar adjacent to the reaction front. The dissolution of K-feldspar has been found to be orientation-dependent (Norberg et al., 2011). This produces characteristic saw tooth-shaped protrusions of albite growing into the host K-feldspar (Hövelmann et al., 2010; Norberg et al., 2011).

Plagioclase

Several workers have stressed the importance of reactions on grain size reduction and concurrent reaction softening for plagioclase porphyroclasts (e.g. Fitz Gerald & Stünitz, 1993; Hippertt, 1998). At greenschist facies conditions plagioclase is often replaced by more albitic plagioclase, muscovite and CaAl-silicates. Fitz Gerald & Stünitz (1993) conclude that the nucleation of albitic plagioclase might be the most important process to form fine-grained albite aggregates in granitic mylonites.

This already indicates that the reactivity and thus the importance of reactions on the

rheology of plagioclase-rich rocks is dependent on the albite content of the original plagioclase. This is because plagioclase with lower albite contents are more stable at lower temperatures. And indeed there are no studies to be found observing some influence of reactions on albite under low temperature conditions.

2.7 High strain deformation of quartzo-feldspathic rocks

Numerous studies have been done on feldspar and quartz rich mylonites from shear zones over a big temperature range. Two different types of microstructures in such rocks are often described: mylonites that have alternating quartz layers and feldspar layers and mylonites with a polyphase quartz-feldspar matrix. In the latter type additional minerals like muscovite may occur in the matrix as well. Both types might also appear in one sample (Fliervoet, 1995).

The polyphase matrix is often attributed to fine grained reaction products replacing plagioclase and K-feldspar, mostly albite, quartz and muscovite (Fitz Gerald & Stünitz, 1993). Fliervoet (1995) describes that a polyphase matrix was developed in the mylonites that experienced the highest strain in the Redbank Deformed Zone. His findings suggest that the polyphase matrix was not only a product of reactions but of some form of mechanical mixing during higher strain deformation. High strain deformation of such polyphase fine-grained aggregates is often explained by grain boundary sliding. This needs some accommodation mechanism to be active. At high temperatures this might be diffusion (Rosenberg & Stünitz, 2003; Menegon et al., 2013), but at greenschist facies conditions pure volume diffusion is too slow in feldspars to be efficient. Fitz Gerald & Stünitz (1993) propose dissolution and precipitation under the presence of a fluid phase as a likely accommodation mechanism at these conditions. These authors also observe that such polyphase aggregates behaved softer than pure quartz layers during high strain deformation.

Many studies, however, report on mylonites that rather contain monophase plagioclase layers that alternate with quartz layers or other minerals in non-granitic rocks (Jiang et al., 2000; Shigematsu & Tanaka, 2000; Mukai et al., 2014). Plagioclase layers can only develop, when the plagioclase content of the rock is sufficiently high. If the feldspar content is too low, quartz forms layers around un- or only slightly deformed porphyroclasts. The rheology of such rocks is then dominated by dislocation creep of quartz.

When a plagioclase matrix is developed, it is often described as "mortar texture" (e.g. White, 1975). Roundish plagioclase porphyroclasts are surrounded by a very fine grained (10–50 μm) plagioclase matrix (Tullis, 1983; Rybacki & Dresen, 2004). Similar microstructures have also been produced experimentally (Tullis & Yund, 1985, 1987). Porphyroclasts of plagioclase are often not flattened ("Augen"), when compared to quartz (Tullis & Yund, 1987). The experiments by Tullis & Yund (1985) and Tullis & Yund (1987) showed that this peculiar microstructure can be obtained by both cataclastic flow at low temperatures and by dislocation creep at higher temperatures. Moreover, microfracturing in the cataclastic regime can produce microstructures that are often associated with dislocation creep, like undulous extinction and core-and-mantle structures. The apparent undulous extinction is actually produced by micro-crush zones, without any dislocation activity (Tullis & Yund, 1987).

Several creep mechanisms may operate in monophase mineral aggregates: cataclastic flow, dislocation creep, diffusion creep and grain boundary sliding. Several of them might be active in a rock at the same time and the dominant mechanisms might be very difficult to infer from microstructural observations alone (Fliervoet, 1995; Rybacki & Dresen, 2004). Cataclastic flow is dominant at the lowest metamorphic conditions and there plagioclase is actually weaker than quartz (Tullis, 1983).

At higher temperatures there is a transition to one of the above creep mechanisms. According to Tullis (1983) the transition from cataclastic flow to dislocation creep should be complete at middle amphibolite facies conditions. Rybacki & Dresen (2004) constructed deformation mechanism maps for feldspar aggregates for high temperature creep with data from several experimental studies. They found that diffusion creep should dominate at most metamorphic grades for the small grain sizes regularly observed in mylonites (10–50 μm). In general, diffusion creep should be favoured at higher temperatures, lower stresses, higher water contents and especially smaller grain sizes compared to dislocation creep (Tullis & Yund, 1991; Rybacki & Dresen, 2004). Tullis & Yund (1985, 1991) found that samples deformed experimentally by dislocation creep show variable high dislocation density, a strong CPO, many 120° triple junctions and a very narrow grain size distribution. Aggregates deformed by diffusion creep show grain growth, open pores and gaps along grain boundaries and a lower free dislocation density.

Grain boundary sliding ("granular flow") involves grains sliding against each other (e.g. Stünitz & Fitz Gerald, 1993). This needs some sort of accommodation mechanism, plastic or diffusive mass transfer. Microstructures produced by grain boundary sliding should have a preferred orientation of grain boundaries at a low angle to the foliation plane (Stünitz & Fitz Gerald, 1993). Stünitz & Fitz Gerald (1993) found that mylonitic granites deformed at greenschist facies conditions mostly deformed by grain boundary sliding accommodated by dissolution precipitation processes. They also observe that local microfracturing can still be an accomodation mechanism, when the stresses at asperities are very high. Grain boundary sliding has also been inferred to be the main deformation mechanism by Jiang et al. (2000) for an albite aggregate naturally deformed at greenschist facies conditions.

3 Geological introduction

The mylonitic pegmatites, discussed in chapters 5 and 6, come from the Austroalpine basement south of the western Tauern Window in the Eastern Alps (yellow box in Fig. 3.1). Quartz-rich gneisses from this area are also used for a comparison with quartz-rich gneisses from the Silvretta crystalline, also part of the Austroalpine basement (blue box in Fig. 3.1) in chapter 7. The Alps resulted from the closure of the Penninic Ocean and multiphase collisions of several microplates and the European plate during the Cretaceous up to the Oligocene (Pfiffner, 2015). The Austroalpine basement in both areas represents a part of the Apulian plate, which was thrust over Penninic and Helvetic units that now form the Tauern and Lower Engadine Windows, respectively. Austroalpine units occur almost exclusively in the Eastern Alps, while they have been mostly eroded in the Western Alps (Schmid et al., 2004).

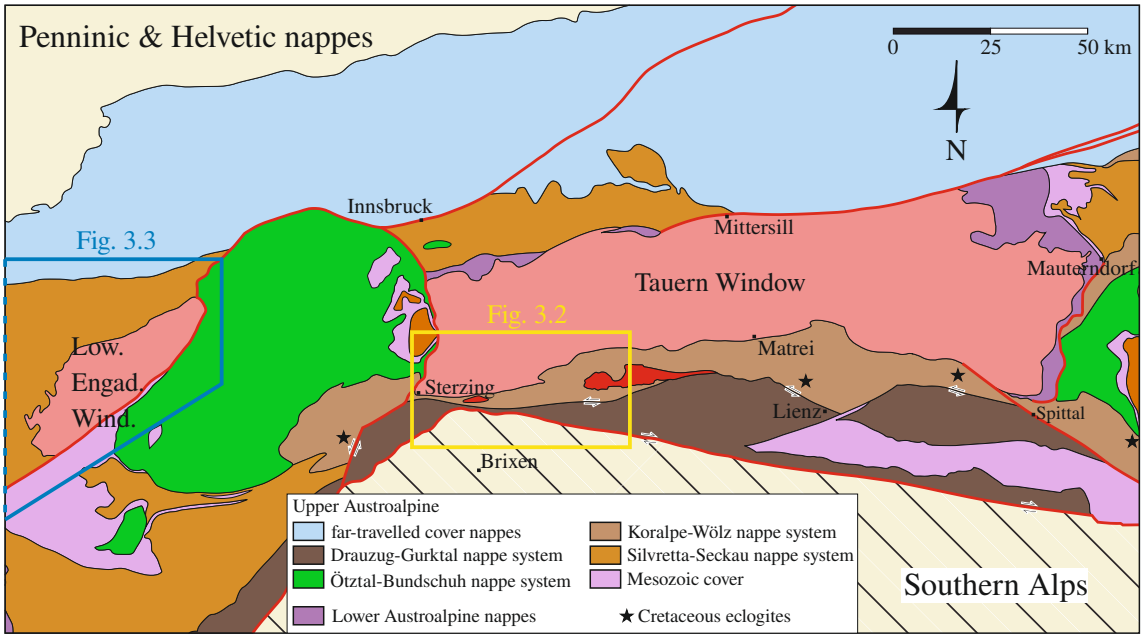

Figure 3.1: Geological map of the Eastern Alps (modified after Schmid et al., 2004, 2013). Detailed maps of the yellow- and magenta-colored insets are shown in Fig. 3.2 and 3.3, respectively

The Austroalpine in the Eastern Alps consists of several nappes, which were stacked during Cretaceous times ("Eo-Alpine" orogeny). The Austroalpine nappes comprise polymetamorphic basement rocks and Mesozoic cover sediments. Henceforth the terminology of Schmid et al. (2004) and Schmid et al. (2013) concerning the structure and units of the Austroalpine basement nappes will be followed. The Austroalpine units are roughly divided into the Lower and Upper Austroalpine. Both the Silvretta units and the basement units south of the western Tauern Window belong to the Upper Austroalpine. Also belonging to the Upper Austroalpine are Palaeozoic (Grauwackenzone) and Mesozoic (Northern Calcareous Alps) cover units. These were detached from their basement and stacked in the Cretaceous (Eisbacher et al., 1990).

The Upper Austroalpine basement can be divided into four structurally different nappes.

These are, from structurally highest to lowest, the *Drauzug-Gurktal nappe system*, the *Ötztal-Bundschuh nappe system*, the *Koralpe-Wölz nappe system* and the *Silvretta-Seckau nappe system*. All of these units experienced greenschist to eclogite facies metamorphism during Cretaceous nappe stacking and were partially overprinted (except the *Drauzug-Gurktal nappe system*) during Tertiary Alpine tectonometamorphism.

3.1 The Austroalpine basement south of the western Tauern Window

The Austroalpine basement south of the western Tauern Window can be roughly divided into a northern and a southern block that are separated by the Defereggen-Antholz-Vals (DAV) shear zone (Fig. 3.2). Along the Periadriatic fault the Austroalpine basement is elevated relative to the Southern Alps. The northern block consists mainly of metapsammopelitic rocks interlayered with marbles, quartzites and amphibolites. The southern block comprises a monotonous suite of psammopelitic gneisses (Kleinschrodt, 1987).

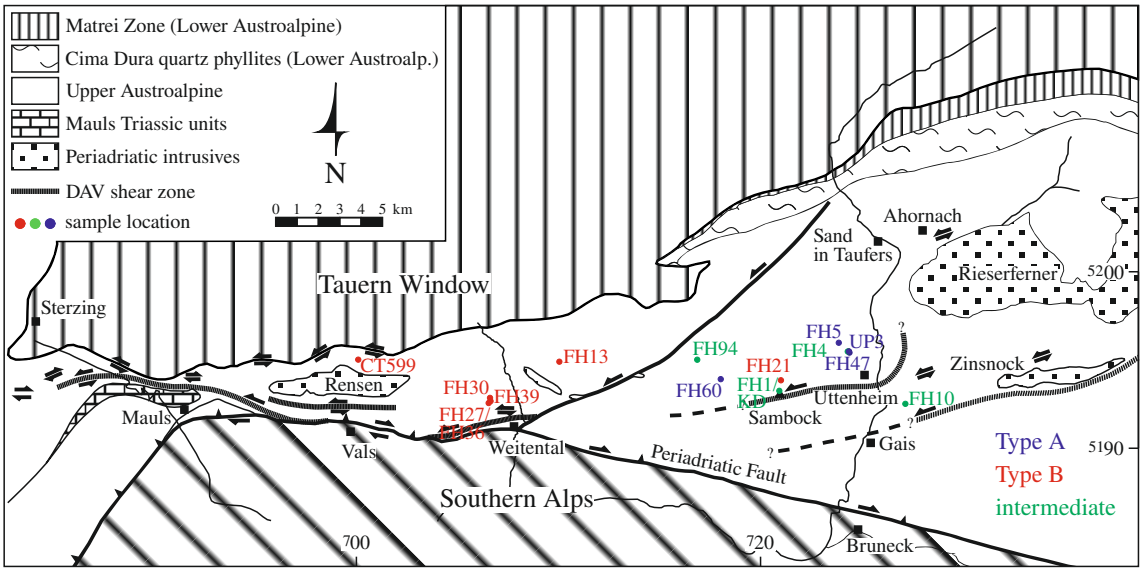

Figure 3.2: Geological map of the Austroalpine basement south of the western Tauern Window (modified after Mancktelow et al., 2001). The sample numbers are colored according to the type of albite-quartz matrix (see chapter 5 and appendix A2).

The paragneisses that now form most of the Austroalpine basement were intruded by huge masses of felsic plutonics in the Ordovician (Siegesmund et al., 2006; Schulz et al., 2008). During the Variscan orogeny the rocks experienced multiphase metamorphism and deformation. Metamorphic conditions reached the middle amphibolite facies (Stöckhert, 1985; Schulz et al., 2008). In the Permian felsic pegmatites, containing muscovite and/or tourmaline, intruded. Samples of the pegmatites from Uttenheim were dated at $\sim 262 \pm 7$ Ma (Rb/Sr WR) by Borsi et al. (1980). This age is quite similar to other occurrences throughout the Austroalpine (e.g. Schuster & Stüwe, 2008; Knoll et al., 2018). According to Stöckhert (1987) these pegmatites crystallised from water-rich anatectic melts originating from late-Variscan HT-metamorphism. Most authors today rather assign the pegmatite formation to a separate Permian HT/LP-event, which is widespread in the Austroalpine (e.g. Schuster & Stüwe, 2008; Spiess et al., 2010).

Most of the Austroalpine units experienced metamorphism and deformation during the Cretaceous Eo-Alpine orogeny (Schmid et al., 2004). This however is not as clear for the Austroalpine south of the Tauern Window (Schulz et al., 2008). In the synoptic work of Schmid et al. (2004) the block north of the DAV is part of the *Koralpe-Wölz nappe system* and the southern block part of the *Drauzug-Gurktal nappe system*. In the general model of Eo-alpine nappe stacking the *Koralpe-Wölz nappe system* experienced high pressure/high temperature-metamorphism as the *Drauzug-Gurktal nappe system* was thrusted above it and eclogites were formed (e.g. Schuster, 2004). Most of these eclogites are only found east and west of the Tauern Window. Only two locations of Cretaceous eclogites are known south of the Tauern Window: from the Schobergruppe and the Polinik unit (Fig. 3.1; Hoinkes et al., 1999). From these two areas also 90–60 Ma mica-cooling ages for metapelites are known (Schulz et al., 2008). Stöckhert (1984) analysed white mica in pegmatites from Uttenheim. These yielded ages of 102 ± 2 Ma, which the author ascribes to cooling after metamorphism and deformation in the upper greenschist facies during the "Old Alpine" event. Schulz et al. (2008) found no indications for high-grade Cretaceous metamorphism in the adjacent Northern-Defereggen-Patzeck-Group, which corresponds to the northern block of the area studied here. Additionally, they found mostly Permian and Carboniferous monazites in their study area south of the DAV shear zone. They conclude that the regional extent and distribution of the Eo-Alpine overprint are not well known yet (Schulz et al., 2008).

During the Tertiary Alpine orogeny the northern block experienced conditions of the lower greenschist facies – about 350 ± 50 °C & 4.5 ± 1.5 kbar (Stöckhert, 1987). In the southern block temperatures did not exceed 300 °C and only brittle deformation prevailed (Kleinschrodt, 1987). 30–35 Ma ago several plutons (Riesenferner, Rensen) intruded the Austroalpine, mostly along the Periadriatic fault system (Steenken et al., 2002; Wagner et al., 2006).

3.1.1 Alpine deformation

Shear zones and folds in the Austroalpine units in the study area (northern block) are heterogeneously developed (Mancktelow et al., 2001). Nonetheless, the orientation of structural features is quite constant: ENE strike of the foliation with a more-or-less steep dip. Stretching, intersection and fold axis lineations are nearly horizontal. The sense of shear is consistently sinistral, where determinable (Mancktelow et al., 2001; Forer et al., 2009). There is an irregular gradation to increasing intensity of Alpine overprint towards the Tauern Window (Mancktelow et al., 2001; Döhler, 2012).

The first definite timing of deformation is given by the earliest mylonitic fabric, which overprints the Permian pegmatites (Stöckhert, 1987; Schulz, 1994). There are no direct indications for Permian and/or Jurassic deformation, which occur in other parts of the Austroalpine (Mancktelow et al., 1999, 2001). Stöckhert (1987) and Schulz (1994) distinguished between an "Old Alpine" deformation at 450 ± 50 °C (Stöckhert, 1987) and a younger overprint from 280 °C at the DAV sensu stricto to upper greenschist facies conditions to the north (Stöckhert et al., 1999). Those workers made their distinction on the basis of metamorphic conditions during deformation. They took recrystallization of feldspar and annealed quartz fabrics in mylonites as characteristic for the older event (Stöckhert, 1987). Brittle deformation of feldspar and dynamic recrystallization

of quartz to a small grain size indicate the younger event (Kleinschrodt, 1987; Stöckhert et al., 1999). Based on quartz c-axis orientations Schulz (1994) maintains that the older deformation was mostly coaxial and the younger non-coaxial with a sinistral sense of shear. For both the coarse- and fine-grained fraction of white mica from deformed pegmatites from Uttenheim Stöckhert (1984) obtained concordant Cretaceous K/Ar ages. This is similar to ages reported by Borsi et al. (1973) for pegmatites from Weitental further to the west. However, the K/Ar bulk extraction technique cannot resolve mixed ages and thus there is still some uncertainty on these results. Clearly established though is that sinistral shearing and mylonitisation were active during the emplacement of the Periadriatic plutons around 35–30 Ma ago (Müller et al., 2000; Mancktelow et al., 2001; Wagner et al., 2006). According to Mancktelow et al. (2001) there was a change in regional kinematics to a dextral transpressive regime coeval with emplacement. This led to dextral brittle movement along the Periadriatic fault in the Miocene. This change is coeval with lateral escape of the Eastern Alps and rapid exhumation of the Tauern Window and the surrounding Austroalpine (Mancktelow et al., 2001; Schmid et al., 2013).

In their systematic study of deformation structures along the DAV Mancktelow et al. (2001) found that the distinction between Eoalpine higher grade and DAV lower grade events is not applicable in many occasions. They found microstructures formerly used to distinguish both events in one sample without a clear hiatus between them, which suggests that temperatures were higher at the beginning of deformation. These workers further point out that sinistral shearing would also be in accordance with regional tectonics during the Cretaceous (Mancktelow et al., 2001). Assessment of the deformation history is further complicated by several temperature/depth gradients. Firstly, temperature conditions are gradually increasing towards the Tauern Window as indicated by the microfabric and isotopic ages (e.g. Kleinschrodt, 1987; Stöckhert, 1987; Schulz, 1994; Mancktelow et al., 2001; Müller et al., 2000). Secondly, the amount of uplift and erosion since coeval intrusion of magmatic bodies is increasing from about 10 km in an eastern area of the Rieserferner pluton to about 15 to 25 km in the Rensen area in the west, well documented by geochronological data (e.g. Steenken et al., 2002) and represented by metamorphic overprint of subvolcanic of dikes in the west and largely preserved magmatic fabrics in the east (Trepmann et al., 2004).

3.2 The Silvretta nappe

The Silvretta nappe (Fig. 3.3) represents one of the Upper Austroalpine basement nappes (Froitzheim et al., 1994; Schmid et al., 2004). It covers about 1600 km^2, and is mainly composed of Pre-Variscan and Variscan paragneisses, orthogneisses and amphibolites (Thöni, 1981, 1988; Maggetti & Flisch, 1993; Schweinehage, 2000) and is characterized by kilometer-long folds ("Schlingentektonik").

After extensive Variscan metamorphism and deformation the Silvretta units where affected by continuous extensional tectonics during the Permian (Maggetti & Flisch, 1993). This resulted in the formation of numerous basaltic dykes and volcanic deposits (Mercolli & Oberhänsli, 1988). This was followed by platform formation and sedimentation of dolomites in the Jurassic period (Maggetti & Flisch, 1993).

Based on petrographic and geochronological investigations, the Alpine metamorphic peak

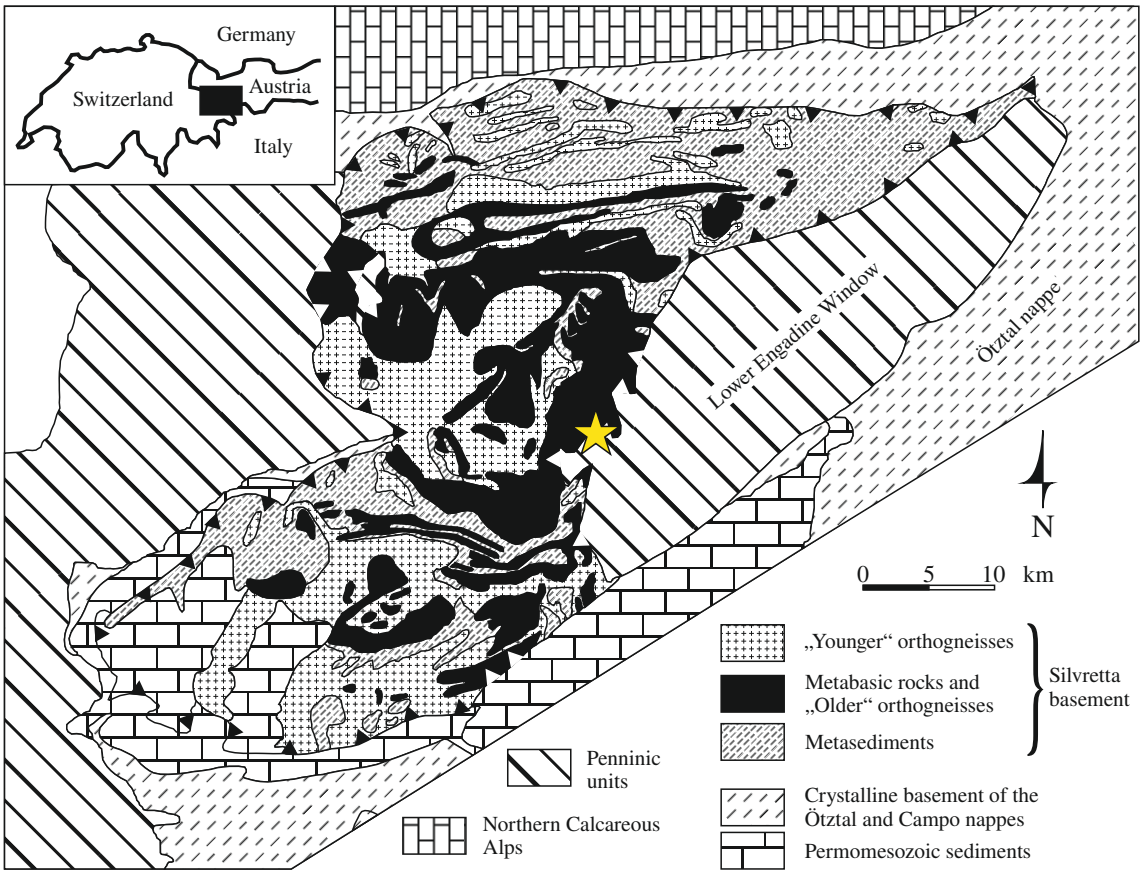

Figure 3.3: Geological map of the Silvretta nappe (modified after Schweinehage, 2000). The location of the samples discussed in chapter 7 is marked with a yellow star

conditions at about 110–90 Ma in the Silvretta crystalline sheet systematically increase from W to E, with temperatures reaching 350–540 °C at the contact zone to the Lower Engadine window (Thöni, 1981; Hurford et al., 1989; Maggetti & Flisch, 1993). This peak of Eo-alpine metamorphism was followed by uplift and detachment from its original substratum. The Silvretta nappe was thrust over Penninic units during the Alpine orogeny (Laubscher, 1983), which are now exposed in the adjacent Engadine Window. Fault rocks of the Silvretta basal thrust comprise pseudotachylytes, mylonites and ultramylonites (e.g. Masch & Koch, 1992; Schmutz, 1995). It is generally assumed that pseudotachylytes formed during the detachment of the Silvretta nappe (Laubscher, 1983; Thöni, 1988; Masch & Koch, 1992; Schmutz, 1995). Schmutz (1995) suggested that the substratum was of similar composition as the Silvretta nappe. Rb/Sr and Ar/Ar isotopic investigations of pseudotachylytes indicate that they formed about 75 Ma ago (Thöni, 1988; Bachmann et al., 2009). Fault rocks are assumed to have developed at lower greenschist facies conditions between 300 and 400 °C, as indicated by Alpine mineral paragenesis in pseudotachylytes and their host rocks (Masch & Koch, 1992), which is consistent with the related quartz microfabrics (Bachmann et al., 2009). During the Tertiary the Silvretta units were mainly effected by the vaulting of the Lower Engadine Window.

4 Analytical methods

This chapter gives an overview of all methods used during this dissertation. Extra information like sampling strategies will be given in the specific chapters.

All samples were cut perpendicular to the foliation and parallel to the stretching lineation. Thin sections of ~ 30 μm thickness were polished mechanically and then coated with a thin layer ($\sim$ 5 nm) of carbon for scanning electron microscopy (SEM) and electron microprobe. Electron microscopic investigations were performed on a Hitachi SU5000 with a field emission gun. Semi-quantitative chemical measurements by energy dispersive spectroscopy (EDS, AZtec, Oxford instruments) were acquired using an accelerating voltage of 20 kV and a working distance of 10 mm. Cathodoluminescence (CL) imaging using a Gatan MiniCL detector was performed at 5 kV and 10 mm working distance. Compositions of feldspars and other major minerals were measured by a Cameca SX100 electron microprobe, using 15 kV voltage, 10 nA beam current, 1 μm spot size and common silicate/oxide standards. The ZAF correction scheme provided by Cameca was used.

4.1 Texture analysis with EBSD

For EBSD (electron backscatter diffraction) analysis thin sections, additionally, were polished chemo-mechanically for at least 60 min in a colloidal silica-solution (Syton) before carbon coating. Field emission electron microscopes, a LEO (Zeiss) Gemini 1530 at Ruhr-University Bochum and a SU5000 (Hitachi) at Ludwig-Maximilians University Munich, were used. An acceleration voltage of 20 kV and a working distance of 20–25 mm were applied for electron back scatter diffraction (EBSD) analysis. Samples were tilted at an angle of 70° with respect to the beam. EBSD patterns were automatically measured (step size of 0.7–1 mm) dependent on the required resolution, grain size and size of the area measured. The acquired EBS patterns were indexed automatically by the AZtec analysis software (Oxford instruments).

All crystallographic orientations are presented in pole figures, in which the stretching lineation (X) is oriented east-west and the pole to the foliation (Z) is oriented north-south. For quartz the [0001]-direction and poles to $\{11\bar{2}0\}$- and $\{10\bar{1}1\}$-planes are shown. As albite is triclinic, in principle, upper- and lower-hemisphere projections are needed to present the whole orientation information. For qualitative comparisons only display poles to the (100)-, (010)- and (001)-planes were chosen to be displayed. Using directions did not change the presented conclusions. For grain reconstruction a thresholding angle of 10° was used and grains with a diameter smaller than twice the step size were ignored to avoid artefacts.

For the analyses presented in chapter 5 the EBSD data were analysed with the MTEX toolbox for Matlab, developed by Ralf Hielscher (https://mtex-toolbox.github.io/; e.g. Bachmann et al., 2010). Small non-indexed pixels were filled during data smoothing by a half-quadratic filter (Bergmann et al., 2016). For grain reconstruction, Dauphiné twin boundaries in quartz are neglected by merging grains along boundaries characterized by a misorientation angle of 60° and a [0001] rotation axis. Evaluating albite

grain boundaries in full misorientation space (Krakow et al., 2017) revealed that almost all twins correspond to the albite law and some to the pericline law. For grain reconstruction of albite, grains were merged along the corresponding twin boundaries. Evaluating mean grain orientations, neglecting the twin orientations, requires the use of a higher symmetry, which contains the symmetry element responsible for twinning, which is the point group 121 for albite and 622 for quartz. The mean orientation of the "higher symmetry" grain is the modal orientation of the "lower symmetry" grain. Using the higher symmetry yields the same grain reconstruction result as merging along twin boundaries. Grain size analysis was by area normalization excluding border grains. The mean and median of the area distribution are given in histograms. The aspect ratio and the trend of the grain long axis were calculated from an area-equivalent best-fit ellipse. Pole figures were calculated either from the de-noised EBSD-data (scatter plots) or from orientation distribution functions (ODFs). ODFs were calculated from the grain mean orientation or from every pixel. For the calculation a "de la Vallée-Poussin" kernel was used (https://mtex-toolbox.github.io/; e.g. Bachmann et al., 2010). Kernel width was estimated with the Kullback-Leibler crossvalidation function of MTEX (https://mtex-toolbox.github.io/; e.g. Bachmann et al., 2010). Pole figure densities (pfJ; L2-norm of the pole figures) and texture index (TI, L2-norm of the ODF) are used to characterize texture strength (Mainprice et al., 2015). The internal misorientation of grains is dependent on the density of geometrically necessary dislocations and thus is commonly used as a measure of crystal-plastic strain (e.g. Nicolas & Poirier, 1976; Poirier, 1985; Wheeler, 2009). To compare the intragranular misorientation between grains, we used the grain kernel average misorientation (gKAM; Kilian & Heilbronner, 2017), which can be computed in MTEX. The kernel average misorientation is the misorientation angle averaged over a certain kernel width for every measured point. We used a kernel size of 24 pixels (3rd order neighbours) and ignored misorientation angles above 8°. The sum of these misorientation angles divided by the number of measurements in a grain is gKAM.

For the analyses of quartz microfabrics presented in chapter 7 the data were processed with the software AZtec to produce pole figures, misorientation angle distributions, aspect ratios and shape preferred orientations (SPO)

4.2 Transmission electron microscopy

For TEM sample preparation, detachable thin section were prepared using a thermoplastic adhesive. The samples were then prepared by ion thinning (GATAN PIPS). The TEM samples were thinned at voltages of 3–4 kV and an Ar-beam at an angle of 6–8° with respect to the sample. TEM samples were analysed using bright field conditions at a Tecnai G2 (FEI) microscope operated at 200 kV at Ludwig-Maximilians University Munich, Department of Chemistry.

4.3 Dating of monazite, xenotime and allanite

Monazite, xenotime and allanite were dated *in situ* in the same thin sections used for the other analyses. As monazite and xenotime do not incorporate bigger amounts of common lead, chemical dating using a standard electron microprobe was used. Allanite

was dated by the U-Th/Pb isotope system using mass spectrometry.

4.3.1 Microprobe dating of monazite and xenotime

For microprobe dating of monazite and xenotime the probe current was increased to 200 nA and a thicker carbon coating of 55–60 nm was used. To measure the small quantities of Pb accurately, a counting time of 480 s was used. Counting times for U and Th of 160 & 300 s were used for monazite and of 300 & 160 s for xenotime, respectively (Appendix A3). To monitor instrumental drift, Madagascar monazite (Grand'Homme et al., 2018) was run as unknown (3 points) before and after each analyses of samples.

Ages were calculated for every measurement point by solving the following formula (Montel et al., 1996):

$$Pb = \frac{Th}{232} \cdot [exp(\lambda^{232}t) - 1]208 + \frac{U}{238.4}0.9928 \cdot [exp(\lambda^{238}t) - 1]206 + \frac{U}{238.4}0.0072 \cdot [exp(\lambda^{235}t) - 1]207$$

Uncertainties (2σ) of the microprobe measurements of monazite are 60–170 ppm, 140–230 ppm, 60–170 ppm for U, Th and Pb, respectively. For xenotime the uncertainties are 150–180 ppm, 90–150 ppm, 70–80 ppm for U, Th and Pb. The errors for every age were propagated from these values by a Monte-Carlo simulation using the software NiLeDAM (Seydoux-Guillaume et al., 2012; Villa-Vialaneix et al., 2013).

4.3.2 Dating of allanite

Allanite was dated *in situ* using using an ELAN DRC-e quadrupole LA-ICP-MS with a 193 nm ArF excimer laser at the Institute of Geological Sciences, University of Bern. The analytical procedure followed that of Burn et al. (2017) and Giuntoli et al. (2018). For ablation the laser was tuned to a repetition rate of 9 Hz and a surface energy density of 2.5 Jcm^{-2}. The signal acquisition followied a pre-ablation stage at 1 Hz and 2.5 Jcm^{-2}. Spot sizes of 24 μm were used during measurement and 32 μm for pre-ablation. The ablated material was transported from the ablation cell to the plasma as an aerosol using a gas mixture made of He (1 $Lmin^{-1}$) and H^2 (0.08 $Lmin^{-1}$). Allanite Th/Pb and U/Pb ratios were obtained using Plešovice zircon (Sláma et al., 2008) as primary reference material and the non-matrix-matched standardization procedure included in the in-house software package TRINITY. Cima d'Asta Pluton allanite (CAP) was used as a secondary standard to test the calibration. Every single-spot analysis consisted of 20 s of washout, 40 s of background counting, $\sim$ 10 s of pre-ablation and 60 s of measurement. The primary reference material (Plešovice) was measured for U–Th–Pb ratio calibration, followed my measurement of the secondary reference material (CAP) every 10 analyses of unknowns.

5 Deformation of feldspar at greenschist facies conditions – the record of mylonitic pegmatites from the Pfunderer Mountains, Eastern Alps

This chapter is based on the manuscript "Hentschel, F.; Trepmann, C.; Janots, E. (2019): Deformation of feldspar at greenschist facies conditions – the record of mylonitic pegmatites from the Pfunderer Mountains, Eastern Alps, *Solid Earth*, 10(1): 95–116, doi: 10.5194/se-10-95-2019".

5.1 Introduction

Assessment of the rheological behavior of the continental crust requires an understanding of grain-scale deformation mechanisms of the main rock-forming minerals at not directly accessible depths. In deep parts of seismically active shear zones (10–20 km) the rheological behavior is controlled by the deformation of granitoid rocks, mainly composed of feldspar and quartz, at greenschist facies conditions. A vast number of experimental studies exist to analyze the deformation mechanisms and to derive flow laws for high-temperature creep of feldspar (e.g. Gleason & Tullis, 1993; Kruse & Stünitz, 2001; Mclaren & Pryer, 2001; Stünitz et al., 2003; Rybacki & Dresen, 2004) and quartz (e.g. Jaoul & Tullis, 1984; Gleason & Tullis, 1993; Hirth et al., 2001; Paterson & Luan, 1990). However, the extrapolation of experimentally deduced flow laws for monomineralic material to the flow behavior of polymineralic rocks at geologically reasonable conditions is problematic (e.g. Pfiffner & Ramsay, 1982; Tullis & Tullis, 1986; Paterson, 1987; Jordan, 1988). Also, the application of flow laws to model the rheological properties of the continental lithosphere (e.g. Brace & Kohlstedt, 1980; Kohlstedt et al., 1995) is a matter of debate (e.g. Rutter & Brodie, 1991; Burov, 2007, 2011; Bürgmann & Dresen, 2008). Uncertainties in models for the rheological properties of the continental lithosphere is partly due to a poor knowledge of the deformation mechanisms actually proceeding at depth as well as the interplay between multiple factors influencing rock strength such as stress variations, fluid content, and metamorphic reactions. The comparison of experimental results with microstructural and mineralogical observations of exhumed metamorphic granitoid rocks, which record the grain-scale mechanical and chemical transformations at depths, is therefore indispensable.

The extrapolation of experimental flow laws for dislocation creep of quartz to natural conditions is found to agree well to natural observations (e.g. Stöckhert et al., 1999; Hirth et al., 2001; Stipp et al., 2002). However, there are large discrepancies in experimental and natural observations on the most abundant mineral of the continental crust, feldspar. Deformation experiments suggest that dislocation creep of feldspar in high strain shear zones is dominant only at high temperatures above about 900 °C (e.g. Rybacki & Dresen, 2004). In contrast, ductile deformation with grain-size reduction and formation of new feldspar grains, commonly assumed to imply dislocation creep, is observed already at greenschist facies conditions (Voll, 1976; Tullis, 1983; Gapais, 1989; Fitz Gerald & Stünitz, 1993; Prior & Wheeler, 1999; Ishii et al., 2007). This discrepancy is partly due to the unclear and strongly varying contribution of brittle, dissolution-precipitation and crystal-plastic processes (e.g. Tullis & Yund, 1987; Stünitz

& Fitz Gerald, 1993; Fitz Gerald & Stünitz, 1993; Tullis et al., 1996; Prior & Wheeler, 1999; Kruse & Stünitz, 2001; Stünitz et al., 2003; Ree et al., 2005; Menegon et al., 2006, 2008; Mehl & Hirth, 2008; Sinha et al., 2010; Brander et al., 2011; Kilian et al., 2011; Eberlei et al., 2014; Mukai et al., 2014). Such a creep behavior governed by the interaction of different deformation mechanisms and chemical reactions in the presence of fluids is especially difficult to assess in experimental approaches. This is partly because experiments have to be performed at high temperatures to realize feasible strain rates, which, however, affects phase assemblages and material properties, for example by partial melting. Therefore, activated mechanisms may strongly differ from those at natural strain rates and greenschist facies conditions. Tullis & Yund (1987) found in their deformation experiments at strain rates of 10^{-4} s^{-1} to 10^{-6} s^{-1} effective dislocation climb with subgrain formation and subgrain rotation only effective at temperatures > 900 °C. They concluded that optically visible subgrains in feldspar from low-grade rocks should not directly be assumed to arise from crystal plasticity but may arise from cataclasis and subsequent healing. Dislocation climb necessary for dynamic recovery and recrystallization requires intracrystalline diffusion. At temperatures < 550 °C, the NaSi $\leftrightarrow$ CaAl interdiffusion rates for plagioclase are very low (Yund, 1986; Korolyuk & Lepezin, 2009). In the presence of water, the diffusion coefficient has been interpreted to be higher (Yund, 1986), which was suggested to account for the weakening observed in experiments where fluid is present (e.g. Rybacki & Dresen, 2004). TEM studies also show that sufficient dislocation climb to produce subgrains is effective only at temperatures from the middle amphibolite upward (e.g. White, 1975; Rosenberg & Stünitz, 2003). The experiments by Tullis & Yund (1985) show that grain boundaries may migrate into areas of higher dislocation density introduced by microfracturing driven by the reduction in strain energy at conditions, at which recovery is not active. However, whether extrapolation to natural conditions is valid can only be evaluated by a comparison to natural microstructures.

To analyze the deformation behavior of feldspar at greenschist facies conditions, the record of mylonitic pegmatites of the Austroalpine basement south of the western Tauern Window and north of the Periadriatic line (Fig. 3.2) are used in this study. They show a wide range of feldspar deformation microstructures and are compositionally and mineralogically relatively simple, as they are characterized by a Ca-poor bulk-rock composition (Stöckhert, 1987). The goal of this study is to correlate characteristic microstructures to specific processes responsible for their formation and to discuss the rheological behavior of the rocks based on these findings

5.2 Sampling

The pegmatites occur within high-grade polymetamorphic upper Austroalpine basement rocks located between the western Tauern Window in the north and the Defereggen-Antholz-Valser (DAV) shear zone in the south (Fig. 3.2; e.g. Hofmann et al., 1983; Stöckhert, 1987; Stöckhert et al., 1999; Müller et al., 2000; Mancktelow et al., 2001; Schmid et al., 2013).

About 100 pegmatites were sampledin three field campaigns in 2015 and 2016 (Appendix A1). Their appearance varies mostly between m- to cm-sized veins or lenses and occasionally km-sized bodies occur (Hofmann et al., 1983; Stöckhert, 1987). In a few cases

a mineral zoning is present. Deformed pegmatites, in veins or layers, have a foliation, which is parallel to that of the host gneisses. The largest pegmatite bodies appear macroscopically undeformed. Pegmatites with a pronounced foliation and stretching lineation (Fig. 5.1 a; Appendix A2) were selected. There is no apparent systematic variation in strain with distance to the DAV shear zone, yet the distribution of different matrix microstructures, as described and discussed later, is different from west to east (Fig. 1).

5.3 Results

The primary magmatic assemblage of the pegmatite comprises quartz, albite-rich plagioclase, K-feldspar and muscovite with accessory tourmaline, garnet, zircon, apatite and monazite. The foliation and stretching lineation are characterized by large fragmented magmatic tourmaline and feldspar, here referred to as porphyroclasts and alternating quartz-, albite- and mica-rich layers (Fig. 5.1 a–d). The plane normal to the observed foliation and the stretching lineation on sample-scale are interpreted to represent the principal axes of the finite strain ellipsoid z and x, respectively, which are indicated in micrographs.

The K-feldspar is Na-poor (< 10 %) and rarely shows perthitic exsolution. Plagioclase porphyroclasts have a narrow compositional range of Ab_{96-100}. In few samples magmatic plagioclase with Ab_{95-86} is present and in these grains zoisite inclusions are common. Magmatic garnet is Mn-rich and low in Ca (on average $Alm_{70}Gro_4Sp_{26}$). During metamorphism, garnet with a higher Ca- and lower Fe-component ($Alm_{35}Gro_{45}Sp_{20}$) partly replaced magmatic grains (Fig. 5.2 a). Epidote and Fe-bearing phengitic white-mica (2 wt% FeO) grew in the foliation plane of mylonitic pegmatites (Fig. 5.2 b).The Fe-bearing phengite sometimes directly replaces magmatic white mica. The modal percentage of albite and K-feldspar varies in the different samples: albite comprises about 60–40 % and K-feldspar about 5–30 %. The matrix layers comprise about 95 % albite, independent on the ratio of K-feldspar to albite porphyroclasts, which varies from 8:1 to 1:9. This observation is consistent with whole-rock compositions with a marked variation of Na2O and K2O reported by Stöckhert (1987). Samples show homogenously low CaO (< 1 wt.%) and FeO, MgO, MnO (< 1 wt.%) contents (Stöckhert, 1987). The variations in the whole-rock composition were interpreted to be due to different compositions of the anatectic melt or mineral zoning in the pegmatite body and affected by external fluids (Stöckhert, 1987). In the following, the specific feldspar porphyroclast and matrix microstructures are described.

5.3.1 Strain shadows

In all samples, polyphase aggregates of K-feldspar, albite, quartz and mica occur in prismatic strain shadows between tourmaline and feldspar fragments and surrounding feldspar porphyroclasts (Figs. 5.1 b; 5.3 a, b). Asymmetric strain shadows are characterized by different microstructures displayed in Figure 5.3 a–c: polyphase aggregates of albite, K-feldspar and quartz characterize the upper-left and lower-right quadrants, whereas the lower-left and upper right quadrants contain almost monophase albite aggregates that alternate with quartz layers. This asymmetric strain shadow is indicating a sinistral sense of shear, with the polyphase aggregate representing extensional quad-

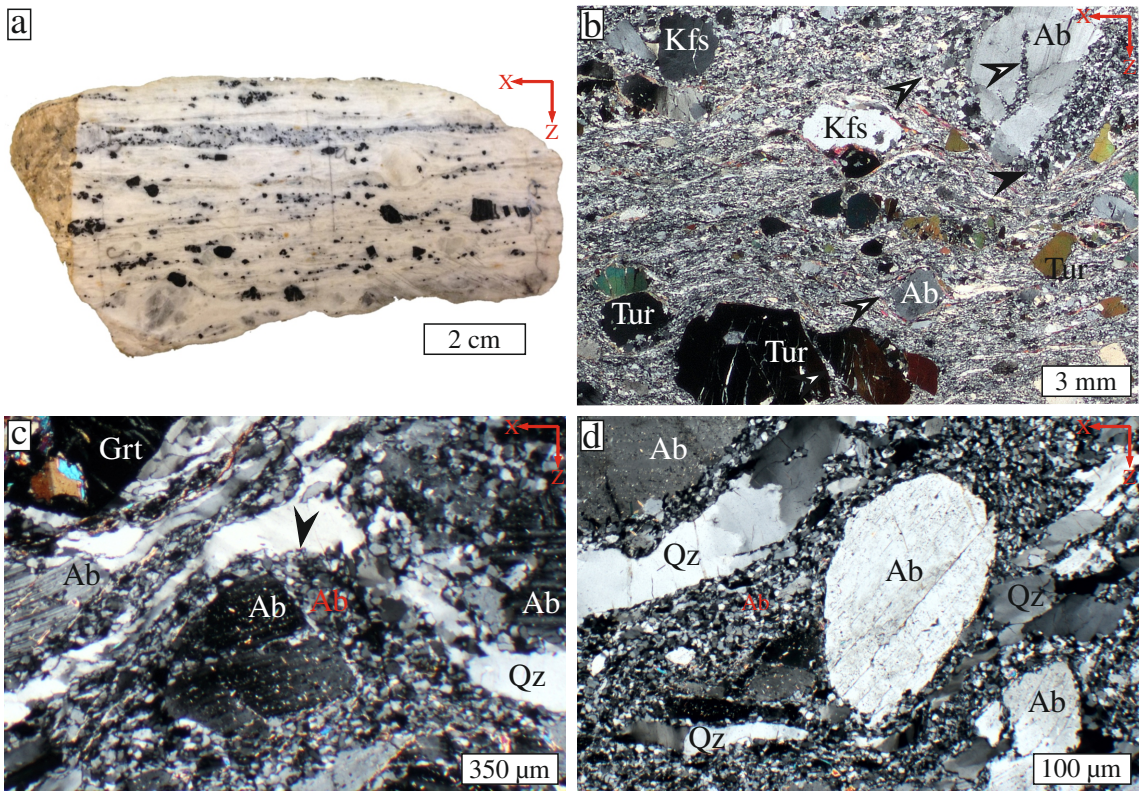

Figure 5.1: Photograph of polished surface **(a)** and thin-section micrograph taken with crossed polarizers **(b)** of sample CT599. K-feldspar (Kfs), albite (Ab) and tourmaline (Tur) porphyroclasts are embedded in a fine-grained matrix. Elongated fractured tourmaline crystals are oriented with their long axes parallel to the stretching lineation (x). Fractures are commonly oriented at a high angle to the stretching lineation (z). Arrows point to strain shadows surrounding porphyroclast and prismatic strain shadows between fragments of tourmaline and feldspar. Black arrow points to mylonitic foliation flowing around strain shadow. **(c, d)** Polarized light micrographs (crossed polarizers, sample FH5b) showing mylonitic foliation defined by quartz layers (Qz) flowing around garnet (Grt) and albite porphyroclasts (Ab), which are partly disintegrated into a fine-grained albite matrix.

rants and the monophase aggregate compressional quadrants. The shape of the albite grains in the monophase layers is rather elliptical with a long axis parallel to the layer, whereas the shape of the albite and K-feldspar grains in the polyphase aggregates are irregular and rather isometric. Grain sizes vary with long axes between 2 and 150 μm, the average of grain diameters is at 25 μm (1 σ = 19 μm) (Fig. 5.3 h, i). The plagioclase composition uniformly ranges between Ab_{97-100}.

EBSD measurements of albite in strain shadows were analyzed comparing single grain orientations with that of the host, comparing pole figures of scattered measurements as well as density plots recalculated from ODF (Fig. 5.3 d–g). The EBSD data reveal no obvious orientation relationship between new grains within aggregates or a specific relationship between new grains and porphyroclasts, although some new grain orientations might correlate with that of the clast (compare to Fig. 5.3 f). Generally, the internal misorientation angles of the grains in aggregates with a typical diameter of 25–30 μm

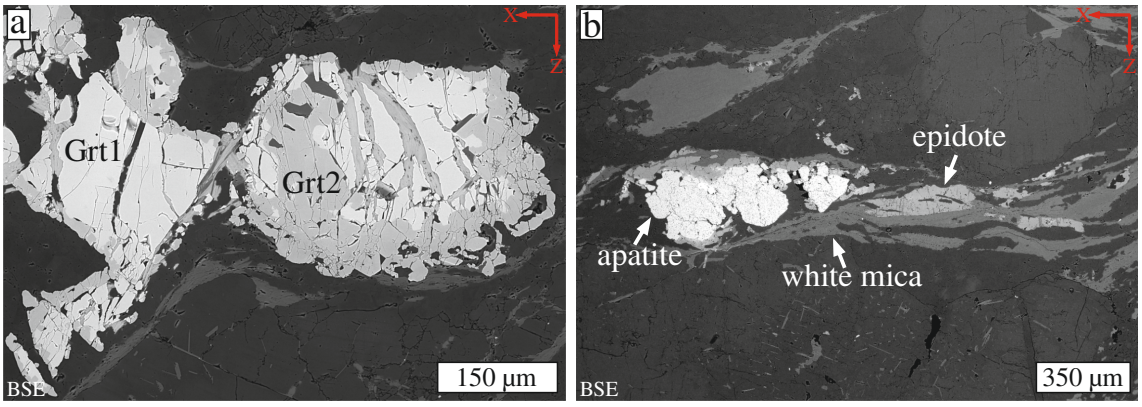

Figure 5.2: Backscattered electron (BSE) images from sample FH27 showing the typical accessory mineral assemblage in the deformed pegmatites: **(a)** Ca-rich garnet (Grt2) replacing magmatic Fe-rich garnet (Grt1). **(b)** Epidote and white mica aligned in the foliation with apatite porphyroclasts.

is low with a maximum internal misorientation generally lower than 5°. The relative misorientation within the albite porphyroclast is lower than 10° (Fig. 5.3 c).

5.3.2 K-feldspar porphyroclasts

Single fractures in K-feldspar porphyroclasts are sealed by aggregates of K-feldspar, albite and quartz, representing prismatic strain shadows (Figs. 5.1 b; 5.4 c, d). Dispersed fluid inclusion trails at high angle to the stretching lineation are interpreted as healed microcracks (Figs. 5.4 a–c). Areas comprising a high amount of healed microcracks are associated to undulous extinction, consistent with a bending of the crystal (Fig. 5.4 a). This bending can be quantified by a change in misorientation angle of about 20° over a distance of 700 μm. Yet, in K-feldspar porphyroclasts that do not show dispersed healed microcracks, the internal misorientation angle within one grain is generally below 5° (Fig. 5.4 d) over a grain size of several mm. The K-feldspar porphyroclast interface with new albite grains is cuspate due to protrusions of small albite grains into K-Feldspar over a length of a few tens of μm. Albite protrusions often have lobate grain boundaries at contact with K-feldspar porphyroclast (Fig. 5.5). The occurrence of this cuspate boundary is independent on position with respect to the stretching lineation or foliation (Figs. 5.4 & 5.5).

EBSD analysis reveals that there is no crystallographic relationship between K-feldspar porphyroclast and new albite grains and the misorientation angle to the porphyroclast is generally high (Fig. 5.4 d, e). The new albite grains often contain numerous pores and inclusions of tiny (< 5 μm) apatite needles, at the vicinity of the K-feldspar porphyroclast interface (Fig. 5.5 b, d). The apatite inclusions are in some places also present in the K-feldspar (Fig. 5.5 b, arrows). Healed microcracks terminate at new albite grains, which therefore are interpreted to have formed after fracturing (arrows in Fig. 5.4 c, d).

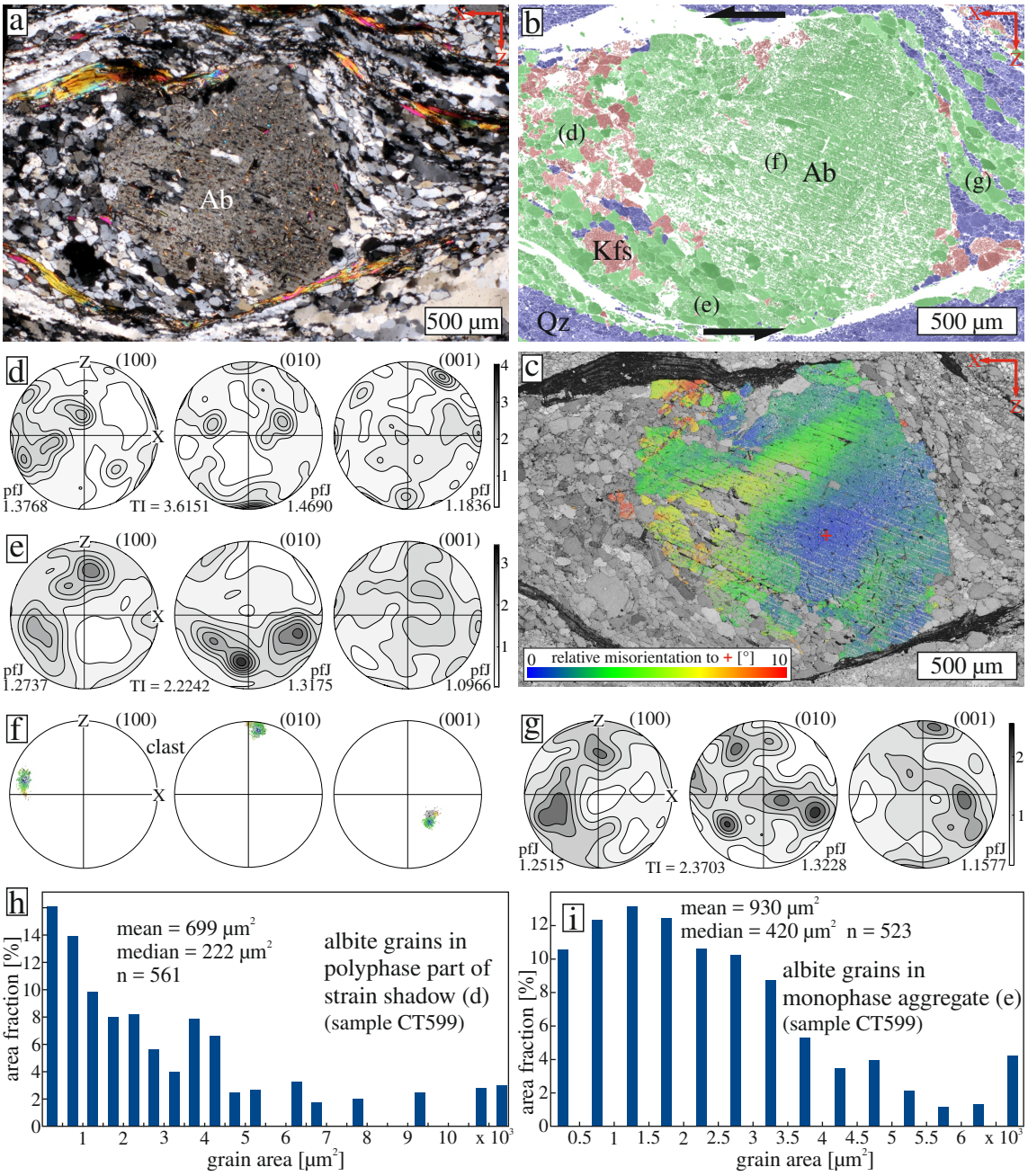

Figure 5.3: **(a)** Asymmetric strain shadow around albite porphyroclast in sample CT599 in thin-section micrograph with crossed polarizers. **(b)** EBSD-phase map of the same area (quartz: blue, albite: green, K-feldspar: red) and **(c)** EBSD-relative misorientation map (0–10°) of the albite porphyroclast. Polyphase aggregates occur mostly in the upper left and lower right of the clast. In the other quadrants, monophase albite dominates. Pole figures show the orientation of albite in the strain shadow in the upper-left quadrant **(d)**, lower-left quadrant **(e)**, albite porphyroclast **(f)** and in the upper-right quadrant **(g)**. Grain area distribution histograms of albite in polyphase aggregates strain shadow **(h)** and in monophase albite aggregates **(i)**.

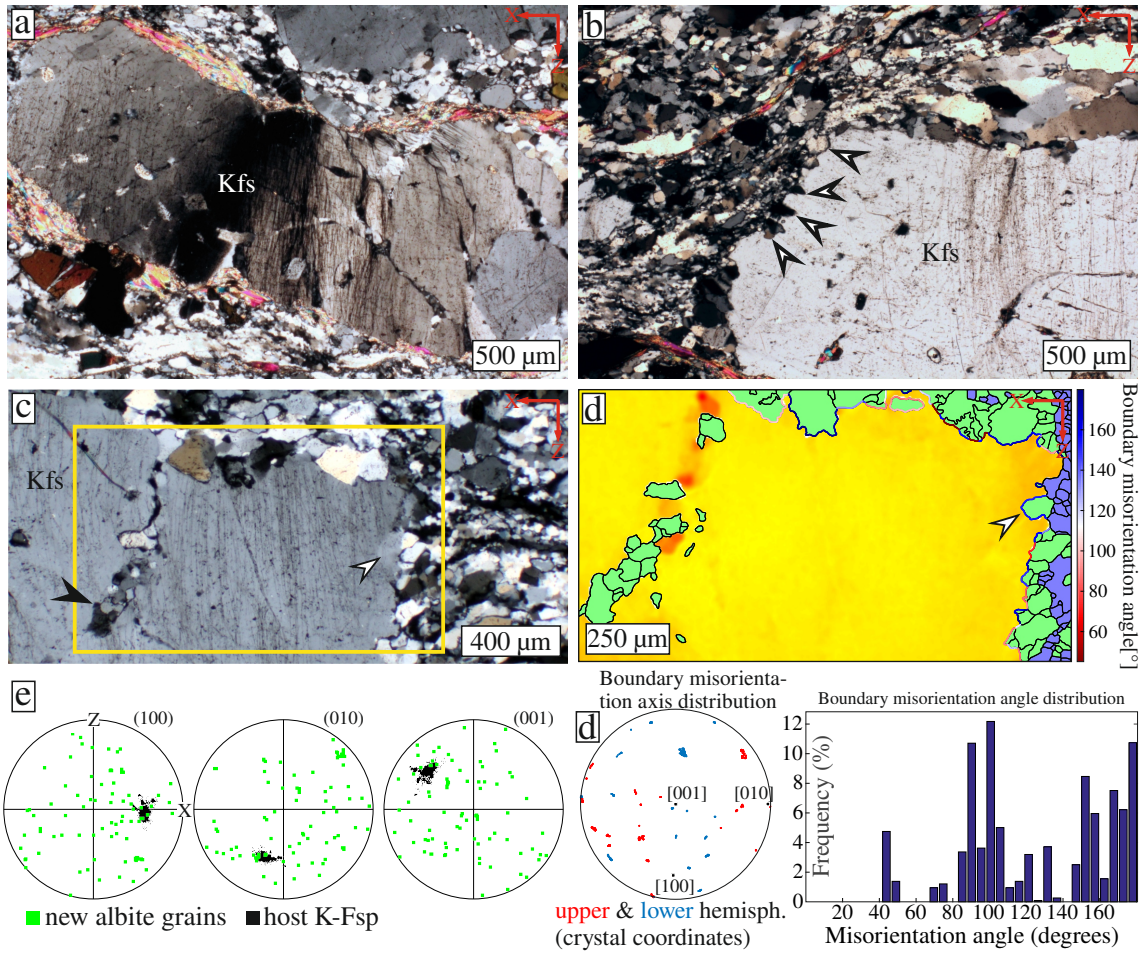

Figure 5.4: K-feldspar deformation microstructures (sample CT599). **(a, b)**Polarized light micrographs (crossed polarizers) of bent K-feldspar porphyroclast with healed microcracks at a high angle to the stretching lineation and cuspate grain boundaries (white arrows in panel b). **(c)** Polarized light micrograph (crossed polarizers) showing K-feldspar with fractures filled with albite (black arrow) and cuspate phase bound- aries. Healed microcracks are cut off by newly formed albite (white arrow). The yellow rectangle shows area of EBSD map in panel (d). **(d)** EBSD map, where boundaries between replacing albite grains (green) and the K-feldspar host (yellow) are colored after their misorientation angle. Quartz in the matrix is blue in color. **(e)** Pole figures of poles to (100), (010) and (001) planes of new albite grains (green) and K-feldspar porphyroclast (black). **(f)** Misorientation angle and axis distribution for the boundaries colored in panel (d).

5.3.3 Albite porphyroclasts

Albite porphyroclasts are commonly twinned, bent and fragmented (Figs. 5.6 & 5.7). The deformed fragments are surrounded by a fine-grained albite aggregate (grain diameters of 27 μm in average) with a very similar composition ($Ab_{96--100}$) compared to the host albite, yet with a tendency to a somewhat higher albite component ($<$ 1 % higher Ab component). An irregular, patchy An-rich seam (up to An_{20}) is commonly observed around new albite grains (Fig. 5.6 f). New albite grains occur along fractures of deformed porphyroclasts that are oriented subparallel to the foliation, i.e. along sites

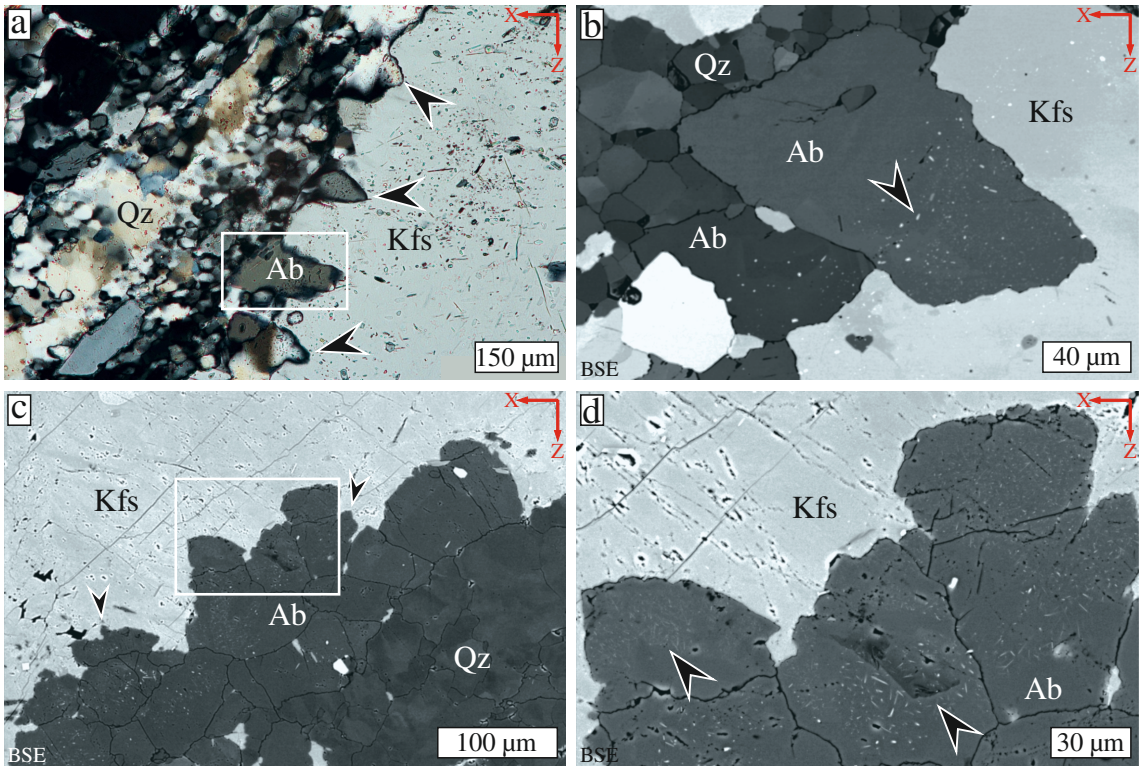

Figure 5.5: (a) Photomicrograph of cuspate interface between K-feldspar clast and new albite grains (sample CT599). **(b)** Close-up BSE image of location indicated by the white box in panel (a). Note the tiny apatite inclusions in the albite (determined by EDS, arrows). **(c)** BSE image of cuspate interface between albite replacing K-feldspar in sample FH14. The arrows point to protrusions. **(d)** Close-up BSE image of the white box in panel (c) showing the numerous tiny (< 5 μm) apatite inclusions in the replacing albite.

of high strain and along boundaries parallel to the foliation (Fig. 5.6 a–c, e). The new albite grains are typically not twinned, in contrast to fragments of the host (Fig. 5.6 b, d).

Larger host fragments have a relative high internal misorientation with angles typically of about 10° along a profile length of 100 μm, ignoring twin domains (Fig. 5.7 g, h). Grain kernel average misorientation (gKAM) values (0.4–0.7°) for new grains are lower than for the porphyroclast or its fragments (0.7–1) (Fig. 5.7 b). Low-angle boundaries are typically observed oriented at high angle to the stretching lineation, indicating that they represent healed cracks associated with a slight misorientation rather than indicating subgrains (Fig. 5.7 a). Curved low-angle boundaries bounding subgrains were not observed. The orientation of the new grains scatters around the orientation of the host crystal (Fig. 5.7 c, d). The misorientation angle distribution shows an excess of low and deficit of high misorientation angles for new grains compared to a random distribution (Fig. 5.7 e, particularly for correlated (neighboring) measurements).

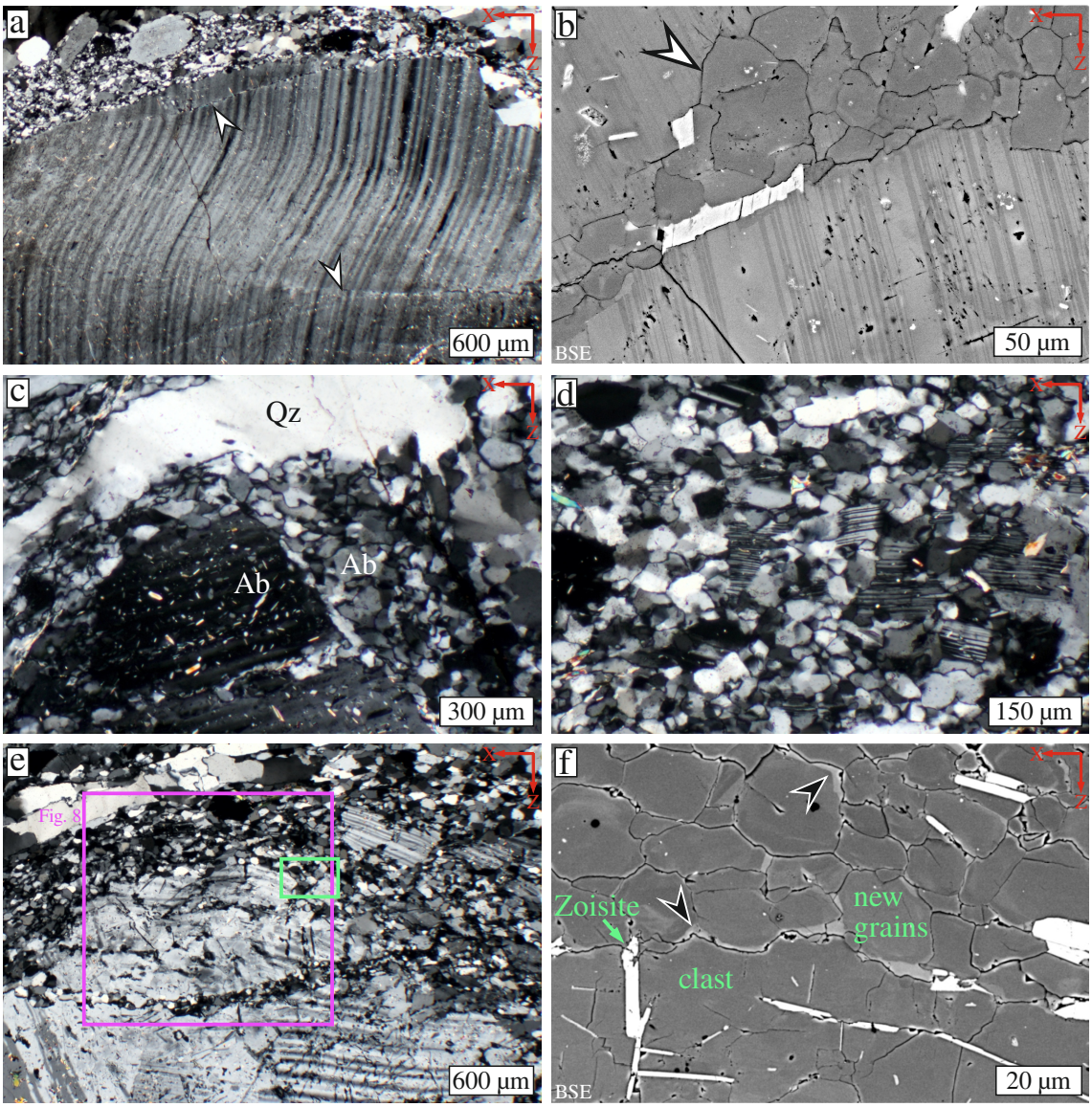

Figure 5.6: **(a)** Polarized light micrograph (crossed polarizers) and **(b)** BSE image of bent and kinked twins in albite porphyroclast, sample FH5. New albite grains occur along fractures parallel to kink band boundaries (arrows). **(c)** Polarized light micrograph (crossed polarizers), showing fragmented albite porphyroclast partly replaced by new grains and surrounded by the quartz layer, sample FH5. **(d)** Polarized light micrograph (crossed polarizers) showing twinned albite fragments surrounded by fine-grained albite matrix, sample FH5. **(e)** Polarized light micrograph (crossed polarizers) of twinned and fractured albite porphyroclast, sample UP3. The green box indicates the area of the BSE image in panel (f); the violet box indicates the EBSD map shown in Fig. 5.7. **(f)** BSE image showing new albite grains adjacent to the albite porphyroclast. New grains often have an outer rim of less albitic plagioclase, up to An_{20} (arrows). The bright phases are zoisite needles.

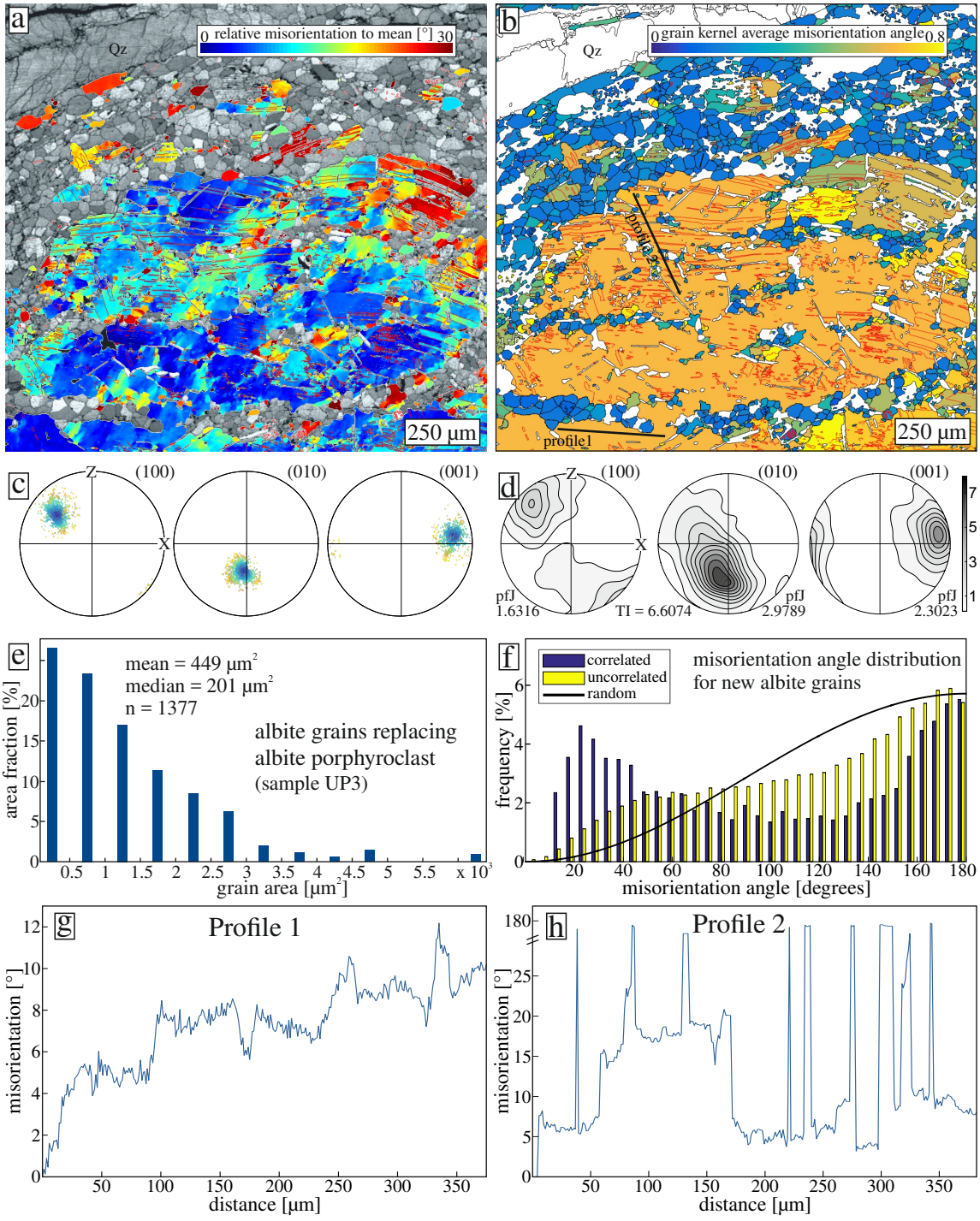

Figure 5.7: (a, b) EBSD-relative misorientation map for albite relative to the mean orientation of the porphyroclast (a) and gKAM map, showing a lower inferred dislocation density for new grains (b) of the area in the violet box in Fig. 5.6b. Red lines indicate albite and pericline twin boundaries. **(c, d)** Corresponding pole figures color-coded corresponding to the EBSD-relative misorientation map (c) and scatter plot (color-coded corresponding to a), where only grains smaller than 100 μm and free of visible twins were used. **(e)** Grain area distribution for new grains smaller than 100 μm. **(f)** Misorientation angle distribution for adjacent and random pairs of new albite grains. **(g, h)** Misorientation profiles (relative to origin) along lines shown in panel (b).

5.3.4 Monophase albite matrix alternating with quartz layers

In the fine-grained matrix, layers of almost purely albitic plagioclase Ab_{97-100} (i.e. similar or slightly more Ab-rich compared to plagioclase porphyroclasts) alternate with quartz-rich layers (Fig. 5.8; Appendix A2). This mylonitic matrix is often deflected by albite porphyroclast and can also be deflected by albite aggregates replacing former porphyroclasts. The microstructure of the layers differs characteristically in their grain size and shape. Based on these two properties, two endmembers of quartz-albite matrix microstructure are distinguished:

- Type A) The albite grains in the a few hundred μm wide layers are isometric (aspect ratio: 1–1.3) with grain diameters varying between 10–70 μm, in average of about 15 μm (Figs. 5.8 & 5.9). The grains usually show no twinning and have a low internal misorientation of generally lower than 5°. The grain boundaries are irregular to smoothly curved (Fig. 5.10). Inclusions of apatite and domains with high porosity are common (Fig. 5.10). Grains show compositional zoning (arrows in Fig. 5.10), which is often only apparent in CL images and is therefore probably linked to changes in trace element contents. This zoning might be truncated by the growth of other grains, generally in the direction of their long axes (green arrow in Fig. 5.10 b). A weak shape preferred orientation (SPO) parallel to the foliation can be deflected around the largest porphyroclasts (Fig. 5.9 a, b). The misorientation angle distribution (Fig. 5.9 c) and pole figures (Fig. 5.9 d) reveal a random texture. Associated quartz-layers are typically a few hundred μm wide and composed of coarse-grained aggregates (diameter of 100–1000 μm; Figs. 5.1 c, d; 5.8 a, b). Quartz in layers shows undulatory extinction, subgrains and sutured grain boundaries (Fig. 5.8 a, b).
- Type B) The albite grains in the layers typically a few tens of μm wide are elongate (aspect ratio: in average 2.3 and up to 9) and show a marked SPO. The average grain diameter is with 30 μm larger than in the type A microstructure (Figs. 5.8 c, d; 5.11). Similar to the type A microstructure, there is no apparent crystallographic preferred orientation (CPO) of albite and grains have a low internal misorientation (Fig. 5.11 b, c). Some K-feldspar can be present as larger clasts (Fig. 5.11 b) or as irregular flakes (Fig. 5.12 a). The grain boundaries are mostly serrated but can vary to smoothly curved and even straight, then they are at low angle to the foliation (Fig. 5.12 a, b). Straight segments can be parallel to the traces of (001) and (010) cleavage plane, representing energetically favored boundaries (e.g. Tröger, 1982). The sutures are affected by intragranular cracks, indicated by trails of pores at high angle to the stretching lineation (arrows in Fig. 5.12 a, b). Numerous tiny apatite needles occur in zones generally restricted to the centre of the grains but can be cut off by grain boundaries (Fig. 5.12 c) or microcracks. Rarely, grains with twins occur (Fig. 5.12 e). Some grains show Ca-enriched zones and areas with a higher porosity (Fig. 5.12 e, f). Generally, new albite grains do not show an orientation contrast observable by BSE imaging, in contrast to twinned remnants of porphyroclasts (Fig. 5.6).

Samples that show the type B matrix microstructure are interpreted to correlate to a higher strain because of the high aspect ratio (up to 9) and narrow spacing of the alternating quartz-albite layers (tens of μm) compared to the type A microstructure with

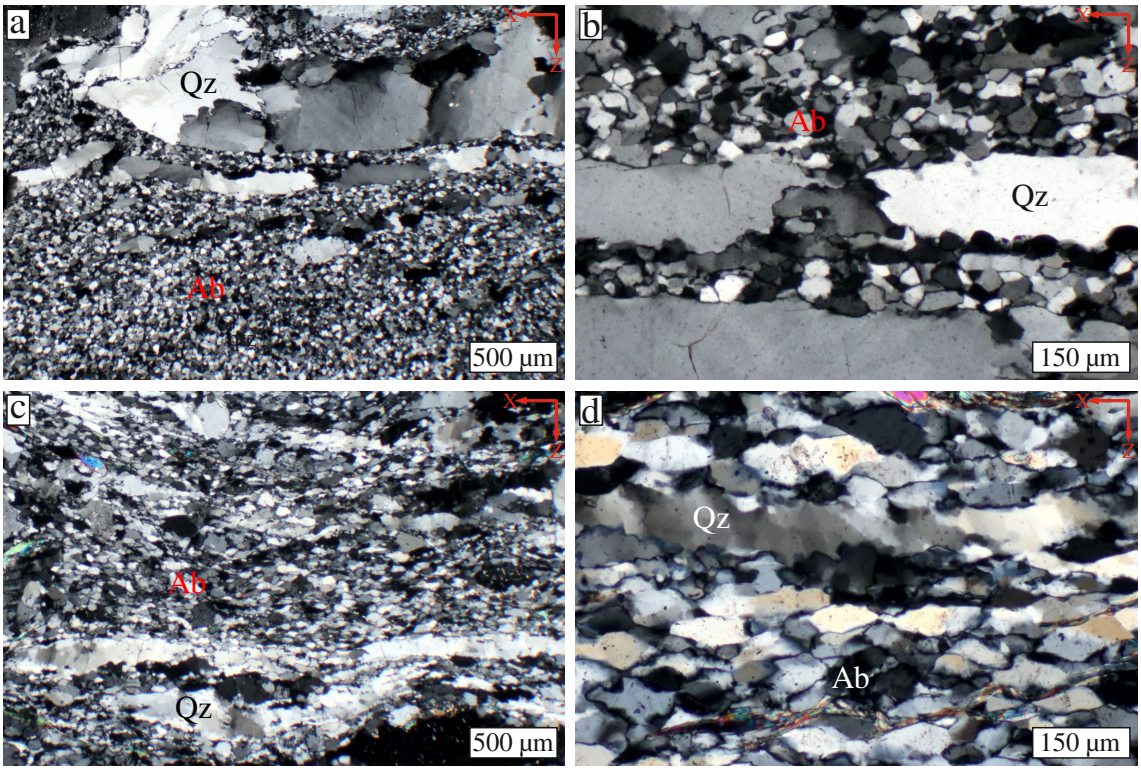

Figure 5.8: Polarized light micrographs taken with crossed polarizers showing the two types of quartz–albite matrix microstructure. **(a, b)** Type A matrix is characterized by coarse quartz layers and albite layers with isometric small grains, sample FH5. **(c, d)** Type B matrix is charac- terized by albite layers characterized by coarser and elongated grains parallel to the foliation, and fine-grained, dynamically recrystallized quartz layers, sample CT599.

a larger spacing of the layers of a few hundreds of μm and a lower aspect ratio (Figs. 5.1 a, b; 5.8 c, d; 5.11 a, b, d). These microfabrics correlate with the observation from the field, where samples showing a type B microstructure are characterized by a more narrow spacing of the foliation planes, lower abundance and diameter of porphyroclast as well as a more pronounced stretching lineation.

5.4 Discussion

In the following, the deformation and replacement mechanisms of feldspar leading to the mylonitic fabric and implications on the Alpine deformation are discussed.

5.4.1 Interface-coupled K-feldspar replacement by albite

The replacement of K-feldspar by albite is a widely observed reaction in deforming granitoids at low temperatures. Different types of replacements of K-feldspar by albite have been discussed, which can be divided into two groups:

1. Neocrystallisation or heterogeneous nucleation during metamorphic reactions and/ or precipitation from the pore fluid, produces distinct albite grains without any

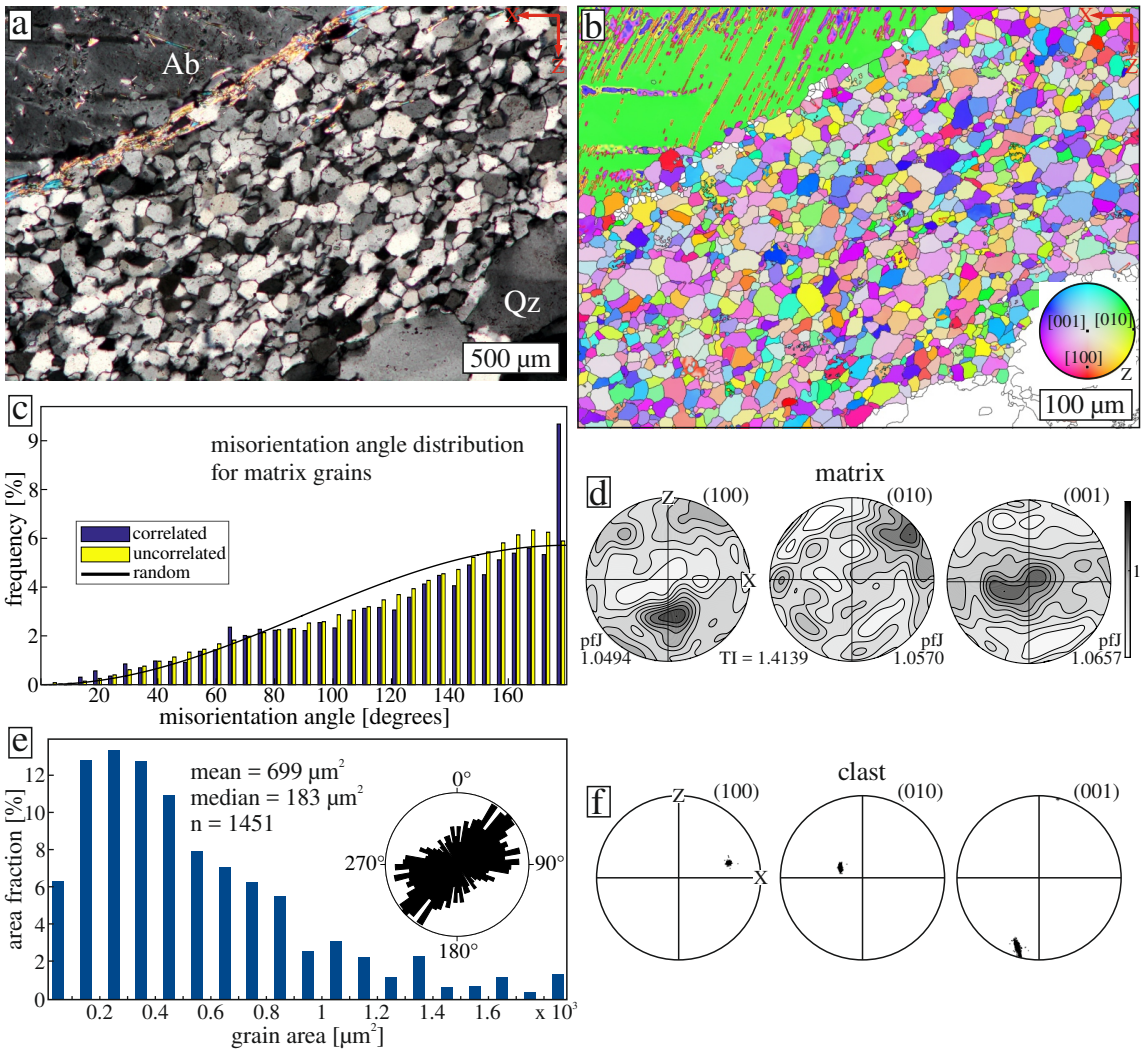

Figure 5.9: EBSD-analysis of type A albite matrix in sample FH5. **(a)** Photomicrograph of the analyzed area. **(b)** EBSD map with inverse pole figure coloring (see lower inset). Twin boundaries in the porphyroclast are shown as red lines. **(c)** Misorientation angle distribution showing an essentially random distribution of neighboring or random grain pairs. **(d)** Contoured pole figures showing orientation distribution of albite matrix grains. **(e)** Grain area distribution of the measured matrix grains. **(f)** Rose diagram showing the orientation of the long axis of grains. **(g)** Pole figures showing the orientation of the albite porphyroclast from panels (a, b).

crystallographic relationship to the replaced K-feldspar. The replacements often appear in strings and patches inside the host grain and may be related to fractures (e.g. Fitz Gerald & Stünitz, 1993; Stünitz, 1998; Menegon et al., 2013).

2. Interface-coupled dissolution of K-feldspar (or plagioclase) and spatially coupled precipitation of albite leads to a strong structural coherence across the reaction interface, i.e. of the primary mineral on the orientation of secondary mineral as found in rocks (Plümper & Putnis, 2009; Putnis, 2009) and experiments (Hövelmann et al., 2010; Norberg et al., 2011). These studies reported that the new albite might be porous and might contain secondary inclusions. Norberg et al. (2011) ob-

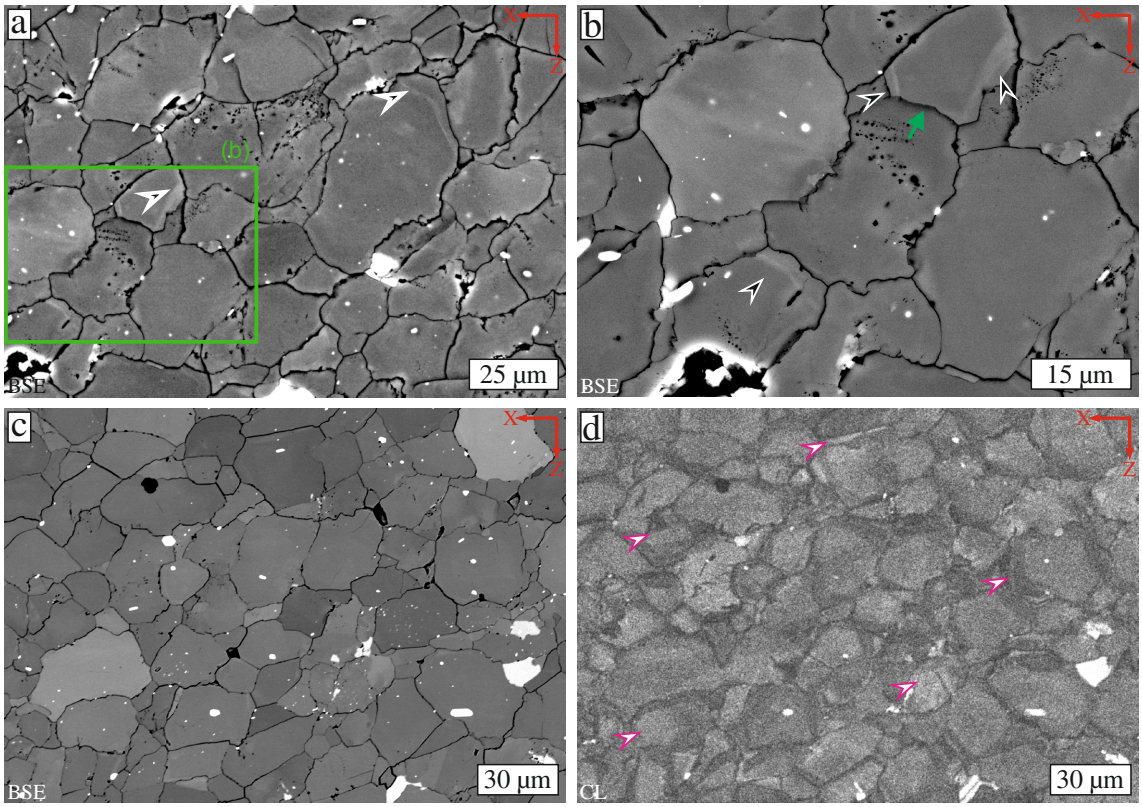

Figure 5.10: Type A matrix, sample FH5. **(a, b)** BSE images show albite matrix with irregular grain boundaries, porosity and weak zonation (black arrows). In panel (b), the zonation of the grain in the upper right is truncated, possibly by growth of the grain below (green arrow). **(c)** BSE image with grey shades representing both orientation and compositional contrast (bright phase is apatite) and **(d)** corresponding CL image showing zonations, not visible in the BSE image (arrows). Grain boundaries in the CL image are also associated with darker grey shades.

served associated microcracking in the K-feldspar adjacent to the reaction front. The dissolution of K-feldspar has been found to be orientation-dependent (Norberg et al., 2011). Cuspate protrusions of albite growing into the host K-feldspar have been found to be characteristic of such interface-coupled replacements (Norberg et al., 2011).

The cuspate boundaries between new grains of albite and K-feldspar porphyroclasts are interpreted to indicate interface-coupled replacement (Fig. 5.5), supported by the porosity and apatite inclusions in albite replacing K-feldspar (Fig. 5.5 b, d). The K-feldspar replacement is independent from the orientation of the boundary to the foliation and stretching lineation and is therefore interpreted to be not directly related to the strain field during deformation, not excluding some influence of higher strain along the boundary compared to within the crystal. The driving force is interpreted to be the difference in solubility between albite and K-feldspar at the given greenschist-facies metamorphic conditions (Putnis, 2009). Whereas locally albite grew to replace K-feldspar, K must have been transported through the pore fluid, either to form metamorphic phengitic mica in the foliation plane or to precipitate K-feldspar in polyphase strain shadows.

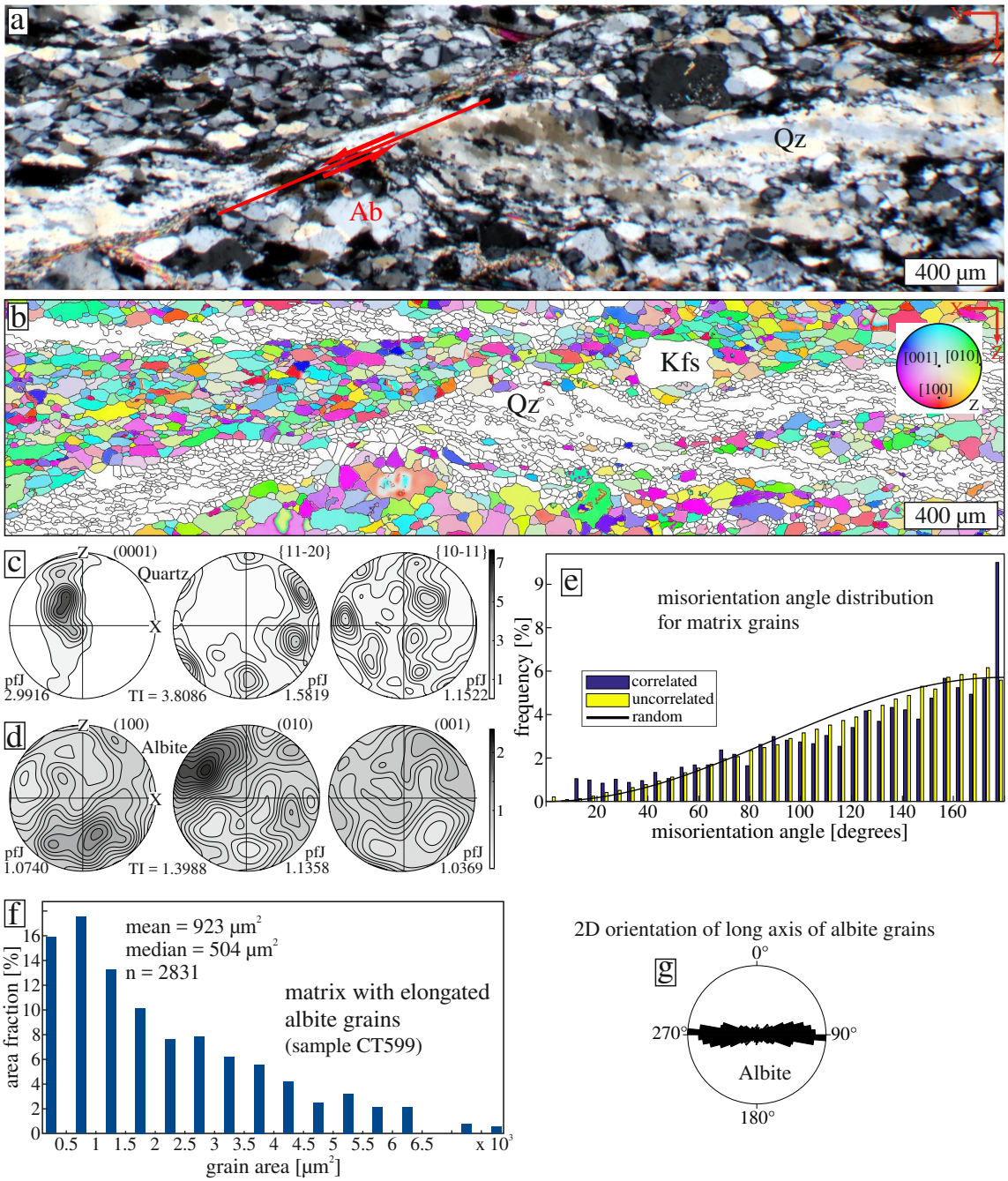

Figure 5.11: **(a)** Photomicrograph of the type B matrix with coarse monophase albite and fine-grained quartz layers in sample CT599. Quartz and albite layers are offset at the shear band marked in red. **(b)** EBSD map of the area from panel (a) with an inverse pole figure (IPF) color code (z axis). Only albite is colored after the IPF color code. **(c)** Pole figures for albite grains from panel (b). **(d)** Pole figures for quartz grains from panel (b). **(e)** Misorientation angle distribution showing an essentially random distribution of neighboring or random grain pairs. **(f)** Grain area distribution diagram. **(g)** Rose diagram of the long axis of albite matrix grains from the area measured by EBSD.

The albite in grains along intragranular fractures within K-feldspar (Figs. 5.1 b; 5.4 d) might represent neocrystallization of albite replacing K-feldspar. As the intragranular

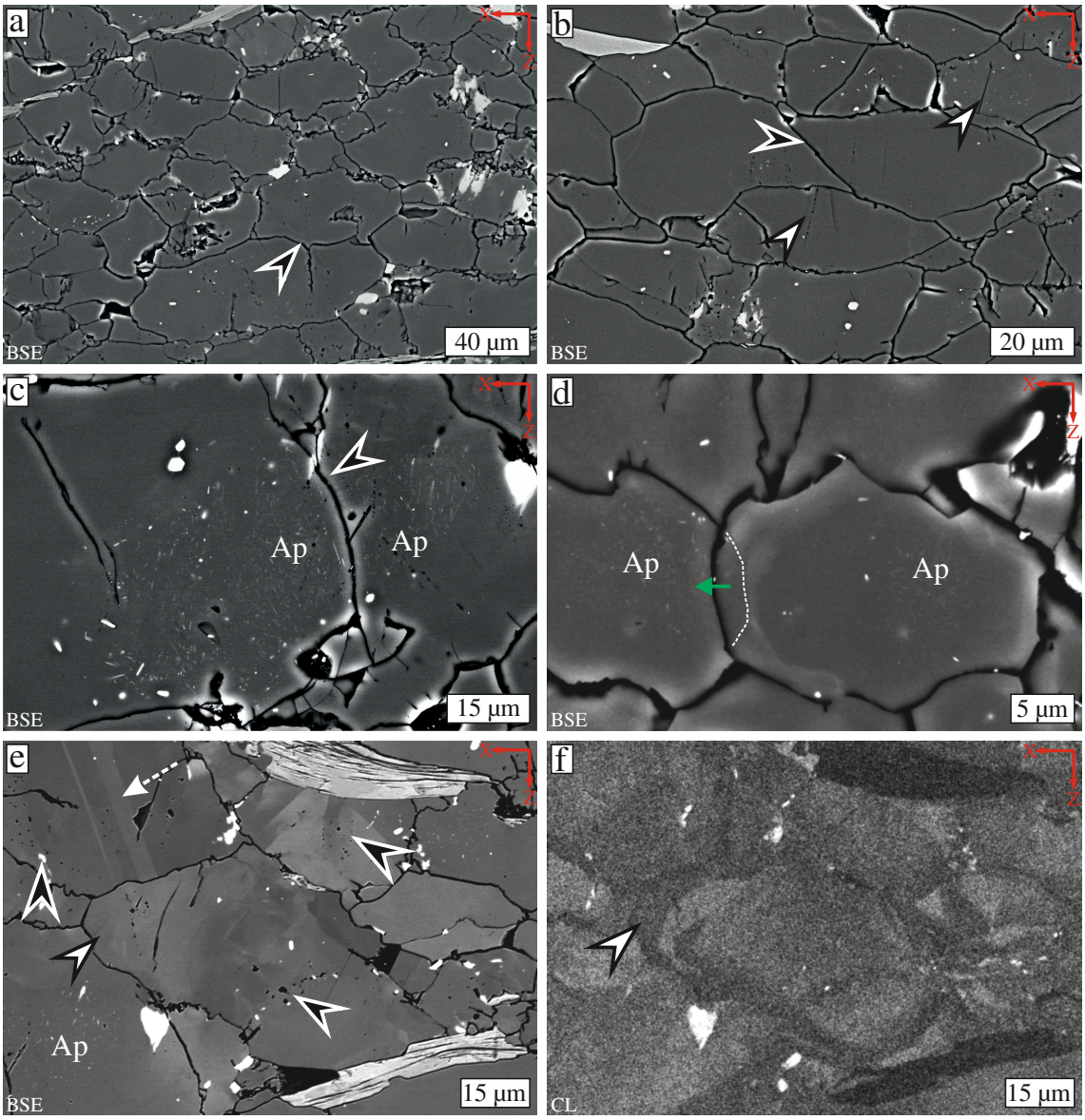

Figure 5.12: BSE images of albite grains in type B matrix. **(a)** Overview showing elongated albite grains and some relict Kfs grains (light grey). Note grain boundary affected by a crack in the grain below (arrow). **(b)** Boundaries can be remarkably straight, especially at a low angle to the foliation (black arrow). Healed microcracks at a high angle to the stretching lineation are indicated by increased porosity (white arrows). **(c)** Apatite needles in albite grains. Apatite-rich zone is crosscut by grain boundary (arrow). **(d)** Albite grains showing the Ca-enriched zone, representing the growth rim (green arrow represents growth direction), with the former grain boundary preserved by the zonation (dashed line). **(e)** Grain with twins (dashed arrow). Black arrows point to porosity, which is associated with zonation (white arrow), best seen in the CL image **(f)**. The zonation is probably due to changing contents of trace elements, which cannot be resolved in the BSE image.

fractures perpendicular to the stretching lination (x), these sealed fractures might represent prismatic strain shadows, i.e. albite may have precipitated from the pore fluid and

not necessarily replacing K-feldspar.

5.4.2 Strain-induced replacement of albite

Albite porphyroclasts are mostly deformed at boundaries parallel to the foliation, commonly associated with bent mechanical twins (Fig. 5.6 a–e). Bent twins are corresponding to an undulous extinction indicating a continuous internal misorientation, which is usually taken to result from the presence of geometrically necessary dislocations (e.g. Nicolas & Poirier, 1976; Poirier, 1985; Wheeler, 2009), though some microcracking might also be involved, as pointed out by Tullis & Yund (1987). For albite this continuous internal misorientation is not associated to distributed healed microfractures, as observed for K-feldspar (compare Figs. 5.4 and 5.6), which is taken to indicate a relative higher importance of dislocation glide for the deformation of albite compared to K-feldspar. Strained areas (fractures, porphyroclast boundaries) parallel to the foliation are replaced by new, strain free grains that are generally not twinned (Fig. 5.6 b, d, e, f). The composition of the new albite grains can be the same as that of the replaced porphyroclast, though it can also show slightly higher Na-content, as already reported by Stöckhert (1987). Plagioclase with Ca-richer compositions occurs locally as thin rims at grain boundaries of new grains with no systematic occurrence (Figs. 5.6 f). Because new strain-free albite grains replace twinned porphyroclasts with internal misorientation at boundaries parallel to the foliation (Figs. 5.6 e, f; 5.7 a, b) and along intragranular microcracks parallel to the foliation (Fig. 5.6 a, b), the replacement is interpreted to be driven by the reduction in stored strain energy. Strain-induced grain boundary migration and formation of growth rims following dislocation glide and microfracturing is consistent with an orientation scatter around the orientation of the host porphyroclast (Fig. 5.7 d, f). The similar composition of the new albite compared to the replaced porphyroclasts, with a tendency of a slightly increased Na-content, suggests a contribution of chemical driving forces although strain-induced grain boundary migration is dominating (Stöckhert, 1982; Stünitz, 1998). Whereas dislocation glide is indicated by bent and twinned porphyroclasts and fragments with internal misorientation, subgrains in deformed fragments (Fig. 5.7 a–c) have not bee observed, even in strongly bent porphyroclasts (Fig. 5.6 a, b, e). This is consistent with the general finding that albite shows only little evidence of dislocation climb with dynamic recovery and recrystallization at $T \leq 550$ °C (e.g. Tullis, 1983; Fitz Gerald & Stünitz, 1993; Kruse & Stünitz, 2001).

The observations suggest that albite porphyroclasts deform in the regime of low-temperature plasticity, where dislocation climb is ineffective and where dislocation glide leads to strain hardening and microfracturing. Additionally, dislocations can be induced by microfracturing (Tullis & Yund, 1987). Subsequently, grains grow by strain-induced grain boundary migration, where crystalline volume with higher strain energy is dissolved and strain-free crystalline volumes precipitated, as suggested by Tullis & Yund (1987). Growth can additionally be by precipitation along areas of lower solubility leading to growth rims with a shape-preferred orientation with long axes in the foliation plane. Strain-induced grain boundary migration might be enhanced by chemical disequilibrium (Stöckhert, 1982; Stünitz, 1998). This interpretation of strain-induced replacement is similar to the “micro-crush zones” described by Tullis & Yund (1992) associated with undulous extinction, shear bands and grain size reduction that are usually associated to

crystal plastic mechanisms (Mclaren & Pryer, 2001; Stünitz et al., 2003). This process is also similar to the "neocrystallization" in the sense of Fitz Gerald & Stünitz (1993) and Menegon et al. (2013), which may or may not cause some compositional variations, dependent on the local fluid present. However, here the term "strain-induced replacement" is suggested for the nucleation by low-temperature plasticity (associated dislocation glide and microfracturing) and growth to stress firstly the importance of dislocation glide (as opposed to the term "micro-crush zones" that stresses brittle mechanisms) and secondly to stress the difference to precipitation with nucleation of new phases from the pore fluid in strain shadows (as opposed to the term "neocrystallization").

5.4.3 Intragranular fracturing of K-feldspar

K-feldspar porphyroclasts deformed dominantly by intragranular fracturing with no comparable strain-induced replacement associated with a grain size reduction as observed for albite. A preferred crystallographic relation of the intragranular fractures was not detected given their orientation at high angle to the stretching lineation independent on crystallographic orientation (Fig. 5.4), ruling out a major influence of cleavage fractures. Single fractures are sealed with albite, K-feldspar and quartz representing prismatic strain shadows, or they are healed (Fig. 5.4). Bending of K-feldspar porphyroclast associated to undulous extinction is restricted to sites of distributed microcracking (Fig. 5.4 a). The high amount of healed microcracks at high angle to the stretching lineation indicates that here, microfracturing was dominating over dislocation glide in the bending of the crystal, as opposed to albite porphyroclasts (compare Fig. 5.4 a and Fig. 5.6 a, e). In contrast to plagioclase, where mechanical twinning is commonly observed, mechanical twinning of K-feldspar is hindered by the Si/Al-ordering (Tullis, 1983).

Reaction weakening of K-feldspar, commonly in association with myrmekites, is known to play a major role during grain size reduction and ductile deformation at many metamorphic conditions (e.g. Simpson & Wintsch, 1989; Tsurumi et al., 2003; Ree et al., 2005; Menegon et al., 2006, 2008; Abart et al., 2014). In the mylonitic pegmatites described here, myrmekitic replacements are very rare and apart from the cuspate replacements, K-feldspar porphyroclasts are well preserved. Thus, reaction weakening of K-feldspar is rheologically not relevant for the mylonitic deformation described here.

5.4.4 Precipitation in strain shadows

The occurrence of polyphase aggregates of K-feldspar, albite, mica and quartz in strain shadows between fragments of tourmaline and feldspar porphyroclasts, as well as surrounding porphyroclast (Figs. 5.1 a, b; 5.3 a–c; 5.4 c, d), with random texture and absent systematic crystallographic relationships indicate that these aggregates represent precipitates of a saturated pore fluid during deformation by dissolution-precipitation creep (e.g. Groshong, 1988; Passchier & Trouw, 2005; Wassmann & Stöckhert, 2013). That few grain orientations in the strain shadow correlate with that of the host crystal is interpreted to be due to the presence of fragments of the host crystal (Fig. 5.3 d). The precipitation of K-feldspar, quartz and albite in strain shadows and albite growth rims is restricted to boundaries at high angle to the stretching lineation (x), i.e. controlled by strain, yet an additional chemical driving force is clearly not ruled out but rather

probable. Additionally, some replacement might also occur in strain shadows. The sites of dissolution are much more difficult to identify, as the material has been removed.

A polyphase matrix of K-feldspar, albite quartz and mica in mylonitic granitoids is often attributed to fine-grained reaction products (e.g. Stünitz & Fitz Gerald, 1993; Rosenberg & Stünitz, 2003; Kilian et al., 2011). Other authors, suggest polyphase matrix to develop by mechanical phase mixing in mylonites at highest strain (Fliervoet, 1995). In the mylonitic pegmatites reported here, however, no indication of active "phase mixing" is observed and the occurrence of a polyphase matrix is attributed to precipitation. Also, the characteristic mylonitic microstructure of the pegmatites is associated not with a polyphase matrix but with the monophase quartz and albite layers.

5.4.5 Formation of monophase albite layers

Based on the observations that albite in layers shows the same characteristics as albite grains replacing albite porphyroclasts (missing subgrains and internal misorientations, apatite inclusions, weak chemical zoning and porosity, and remnants of twinned porphyroclast fragments), it is suggested, that the strain-induced replacement of albite is the most important process of grain size reduction to form the monophase albite layers (Fig. 5.13). Additionally, part of the albite in the mylonitic matrix stems from the replacement of K-feldspar, as suggested by K-feldspar-relicts (Figs. 5.11 b; 5.12 a). Because the matrix layers comprise about 95 % albite, independent on the ratio of K-feldspar to albite porphyroclasts, it is suggested that albite is taking up a higher amount of strain as compared to K-feldspar. Dislocation creep of albite is ruled out as main process to form the fine-grained almost monophase albite layers, given a missing systematic CPO as well as missing evidence of effective dislocation climb. Also, precipitation from the pore fluid as dominating process can be ruled out, given the monophase composition of the layers, in contrast to polyphase aggregates in strain shadows. Cataclasis would suggest a higher amount of twinned and deformed fragments. Instead, only very rarely twinned grains are observed (Fig. 5.12 e).

The observations suggest that after grain size reduction, the fine-grained albite matrix was undergoing a mixture of dissolution-precipitation processes, microcracking and sliding of grains, commonly referred to as granular flow (e.g. Behrmann & Mainprice, 1987; Stünitz & Fitz Gerald, 1993; Jiang et al., 2000). Sliding might have occurred along straight boundaries weakly inclined to the foliation (Fig. 5.12 b). Microcracking is indicated by the fractures at high angles to the foliation (Fig. 5.12 a, b, e). The weak zoning of grains (Figs. 5.10 & 5.12) suggests the involvement of dissolution-precipitation. Granular flow would also cause weakening of a domainal CPO resulting from the replacement of albite porphyroclasts (e.g. Jiang et al., 2000; Hildyard et al., 2011).

Quartz layers of coarse recrystallized grains systematically correlate with albite layers of small isometric grains in the type A matrix microstructure (Figs. 5.8 a, b; 5.9; 5.10). In contrast, narrow quartz layers with fine-grained quartz aggregates and marked CPO are correlated with elongate coarser albite in the type B matrix microstructure (Figs. 5.8 c, d; 5.11; 5.12). The elongate shape of albite and zones of high porosity at boundaries at high angle to the stretching lineation in the type B matrix microstructure indicates growth by precipitation, resulting in a shape-preferred orientation (Fig. 5.12 e, f). The

microstructure correlates with the overall strain of the mylonitic matrix (Fig. 5.13). In samples with higher overall strain, albite grains in the layers are coarser and more elongate and quartz aggregates are finer-grained and have a marked CPO.

5.4.6 Implications for rock rheology and deformation history

The prismatic strain shadows of polyphase material between fragmented tourmaline and feldspar as well as strain shadows surrounding porphyroclasts indicate that dissolution-precipitation creep did play a role in the rheology of the rocks. Yet, other indicators of dissolution-precipitation creep, as for example evidence of dissolved feldspar porphyroclasts along boundaries parallel to the foliation, i.e. strain caps, are remarkably low. The monophase alternating quartz and albite layers are the main characteristic of the mylonites. The dominating process of grain size reduction of feldspar is interpreted to be the strain-induced replacement of albite with associated dislocation glide and fracturing (Fig. 5.13). Subsequent growth by strain-induced grain boundary migration and formation of growth rims by precipitation resulted in a SPO (Fig. 5.13), which took place probably simultaneously together with granular flow and dislocation creep of quartz. As such, for considering the rock's rheology, these different deformation mechanisms and associated processes have to be taken into account, where the relative contributions additionally vary with time. In contrast, dissolution-precipitation creep with dissolution along boundaries parallel to the foliation and precipitation with nucleation of new phases in strain shadows is interpreted to play an only subordinate role for the formation of the mylonitic alternating quartz-albite layers, although precipitation of albite forming elongate grains with SPO in monophase aggregates is important. Furthermore, a major role of dislocation creep of feldspar (i.e. deformation by dislocation glide with simultaneous dynamic recovery) on the formation of the mylonitic microstructure as may be suggested by monophase layers of fine-grained feldspar aggregates, is not supported by any further microstructural observation (e.g. systematic missing of LAGBs) and therefore interpreted to be rheologically not relevant during deformation.

The observation of newly precipitated grains from the pore fluid between tourmaline and K-feldspar fractures at strain shadows as well as the microcracks in K-feldspar that are cut off by the wedge shaped albites replacing K-feldspar (Figs. 5.1 a, b; 5.2 c, d) indicate growth of grains after fracturing and during ongoing deformation. The observation of the deflected mylonitic foliation around former porphyroclasts, which are now replaced by new grains (Figs. 5.1 c, d; 5.6 c), indicates that the new grains grew after or during the formation of the mylonitic layers, but not before. Thus, strain-induced replacement of albite must have played an important role during an early stage of deformation and was ongoing during granular flow. Thus, a specific sequence of different deformation episodes at markedly different metamorphic stages, as had been discussed, is not apparent (Stöckhert, 1987; Mancktelow et al., 2001). The indication of the type A matrix microstructure being dominating in the eastern area and the type B matrix microstructure representing in comparison higher strain in the western area might be correlated with higher metamorphic temperature conditions in the western area, as the amount of uplift and erosion since the intrusion of magmatic bodies at 30 Ma is increasing from about 10 km in an eastern area of the Rieserferner to about 15 to 25 km in the Rensen area in the west (Trepmann et al., 2004).

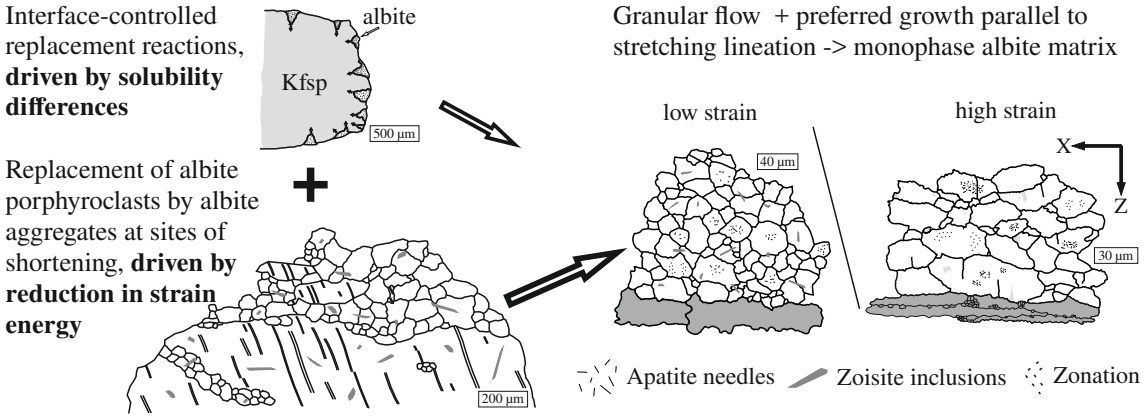

Figure 5.13: Conceptual sketch of the formation of the mylonitic albite matrix. The contribution of replacement of albite porphyroclasts by albite is larger than that of replacement of K-feldspar (see text for discussion).

5.5 Conclusions

The mylonitic pegmatites record the deformation behavior of feldspar at greenschist facies conditions. Based on the presented observations and discussions the following conclusions are drawn:

1. K-feldspar porphyroclasts deformed dominantly by fracturing and only subordinate dislocation glide, without major grain size reduction. Healed or sealed intragranular fractures in large porphyroclasts at high angle to the stretching lineation are the dominating deformation microstructures of K-feldspar (Fig. 5.4).
2. Interface-coupled replacement of K-feldspar by albite is mainly driven by chemical disequilibrium as indicated by the cuspate albite-K-feldspar phase boundaries independent on the orientation of the boundary to the foliation or the stretching lineation (Fig. 5.5).
3. Grain size reduction of albite porphyroclasts is by combined fracturing and dislocation glide, i.e. low-temperature plasticity. Dislocation glide is indicated by bent and twinned remnant host albites with internal misorientation. Evidence of significant amount of dislocation climb allowing effective dislocation creep with dynamic recovery of feldspar is systematically missing (no subgrains, negligible internal misorientation of new grains; Figs. 5.9 c, d; 5.11 c, e).
4. Subsequent strain-induced grain boundary migration and formation of growth rims produced aggregates of strain-free albite grains with SPO at porphyroclast boundaries parallel to the foliation (Figs. 5.6 c–f; 5.7). The observed tendency of slightly enriched Na-content (decrease of Ca-content) of the new albite grains compared to albite porphyroclasts is in agreement with an additional, though subordinate driving force for grain boundary migration by chemical disequilibrium (Stöckhert, 1982).
5. Monophase quartz layers formed dominantly by dislocation creep (dislocation glide, dynamic recovery and recrystallization) of quartz, as indicated by sutured grain boundaries, CPO, subgrains and undulatory extinction (Figs. 5.1 c; 5.8; 5.11 a,

d). Some influence of dissolution-precipitation creep cannot be excluded; though microstructural evidence has not been observed.

6. Granular flow of the new albite grains with overgrowth of albite forming a SPO together with quartz dislocation creep is interpreted to result in the alternating monophase albite-quartz layers (Figs. 5.8–5.12). For considering the rock's rheology, these different deformation mechanisms and associated processes have to be taken into account, where the relative contributions additionally vary with time.

6 Coronas around monazite and xenotime recording incomplete replacement reactions and compositional gradients during greenschist facies metamorphism and deformation

This chapter is based on the manuscript "Hentschel, F.; Janots, E.; Trepmann, C.A.; Magnin, V.; Lanari, P. (in prep): Coronas around monazite and xenotime recording incomplete replacement reactions and compositional gradients during greenschist facies metamorphism and deformation".

6.1 Introduction

Understanding the behaviour of monazite and xenotime in metamorphic reactions of deforming rocks is of great importance in metamorphic petrology. Monazite ($LREEPO_4$) and xenotime ($HREEPO_4$) are widespread accessory minerals and, together with allanite ($CaREEAl_2Fe[Si_2O_7][SiO_4](O,F)(OH,O)$), the most important REE-minerals in metapelitic (e.g. Spear & Pyle, 2002) and (meta-)granitic rocks (e.g. Bea, 1996; Förster, 1998b,a) and as such have attracted much attention in research in the last decades (see Engi, 2017 for a review). Monazite (symmetry: $P2_1/n$) and xenotime (symmetry: $I4_1/amd$) are both orthophosphate minerals, which consist of alternating PO_4-tetrahedra and $REEO_9$-polyhedra. In addition to the obvious REE $\leftrightarrow$ Y substitution, Th and U can be incorporated into the crystal structure as well. The substitution of U and Th is generally not correlated (Spear & Pyle, 2002).

Two main characteristics of monazite and xenotime are important for their use in metamorphic petrology. Firstly, trace elements in rock-forming and accessory minerals, such as REE and Y, contain valuable information about the growth history of the minerals and therefore for the microfabric development of the rock in general, because trace element diffusion is generally slow in major minerals (Spear & Pyle, 2002; Raimondo et al., 2017). An important application of this is the YAG thermometer using Y-contents in garnet and monazite or xenotime (Pyle & Spear, 2000; Pyle et al., 2001). Secondly, because monazite and xenotime incorporate Th and U during growth, both can be used for radiometric dating and, as Pb in both is mostly radiogenic, chemical dating methods, for example by electron microprobe (EMP), can be used (Montel et al., 1996; Suzuki & Kato, 2008; Williams et al., 2007). If these reactions can further be related to deformation and pressure-temperature conditions, U/Pb-Th dating of these minerals can give valuable information on the tectonometamorphic history of the rocks (Williams & Jercinovic, 2012).

The stability of monazite during metamorphism in both metasediments and metagranitioids is characterized by the breakdown/disappearance at mid-T conditions and the (re-)appearance at higher temperatures. In metasediments, monazite is replaced by allanite at about 450 °C during prograde metamorphism, which in turn is replaced by monazite at 550 – 600 °C (e.g. Wing et al., 2003; Janots et al., 2008; Goswami-Banerjee & Robyr, 2015). In rocks of low Ca and Al bulk compositions, monazite is stabilised and allanite might not occur at all. Analogously, xenotime is replaced by and replaces

HREE-rich epidote/clinozoisite during metamorphism. The stability of xenotime might also be controlled by the formation or destruction of garnet, as garnet can control the Y-budget of rocks (Spear & Pyle, 2002).

Apart from the involvement in these characteristic reactions, monazite and xenotime have been found to be susceptible to fluid-mediated breakdown and alteration processes. One peculiar product of monazite and xenotime breakdown reactions is the formation of apatite-allanite/epidote-coronas around monazite or xenotime relics, recording incomplete replacement reactions (Finger et al., 1998; Broska et al., 2005; Majka & Budzyń, 2006; Ondrejka et al., 2012, 2016; Budzyń & Jastrzębski, 2016; Lo Pò et al., 2016). These have been interpreted to be produced by dissolution of monazite/xenotime and subsequent precipitation of apatite and REE-bearing epidote-group minerals. The formation of such microstructures with distinctive zones of the corona minerals has only been vaguely discussed in the literature. While Finger et al. (1998) attribute the concentric alteration structures to diffusion, other authors attribute them to solubility differences of the freed elements in the fluid phase (Broska et al., 2005; Upadhyay & Pruseth, 2012). Still, the exact mechanisms of corona formation remain uncertain and more detailed investigations of textural and chemical variations are crucial.

In this study, the composition, age and microfabric of coronas in mylonitic pegmatites from the Austroalpine basement in the Eastern Alps are used to infer the involved reaction mechanisms, the scale of mass transfer and the relationship to the deformation of the pegmatites. Based on the findings the mechanisms of corona formation and the relations to the deformation of the rocks are discussed. For mineralogical, microfabric and geochronological characterizations imaging and x-ray spectroscopic and electron backscatter diffraction (EBSD) techniques at the scanning electron microscope (SEM), electron microprobe (EMP) and laser ablation inductively coupled mass spectrometry (LA-ICP-MS) dating are used.

6.2 Results

6.2.1 Sample description

Corona structures around monazite are present in deformed pegmatites in a matrix of alternating quartz and albite layers that form a mylonitic foliation (Fig. 6.1 a), as well as included in tourmaline (Fig. 6.1 c, d). Samples were collected in field campaigns in 2016 and 2017 and thin sections prepared from slices perpendicular to the foliation and parallel to the stretching lineation of the finite strain ellipsoid (Hentschel et al., 2019). The magmatic assemblage of the pegmatite is quartz, albitic plagioclase, K-feldspar and muscovite, accompanied by accessory tourmaline, garnet, zircon, apatite and monazite. Primary magmatic garnet is Mn-rich and low in Ca (on average $Alm_{70}Gro_4Sp_{26}$). During metamorphism, garnet with a higher Ca and lower Fe component ($Alm_{35}Gro_{45}Sp_{20}$) partly replaced magmatic grains. Epidote and Fe-bearing phengitic white mica (2 wt% FeO) occur in the foliation plane of the deformed pegmatites. For a detailed description of the geochemistry and microfabric of the pegmatites the reader is referred to Stöckhert (1987) and Hentschel et al. (2019).

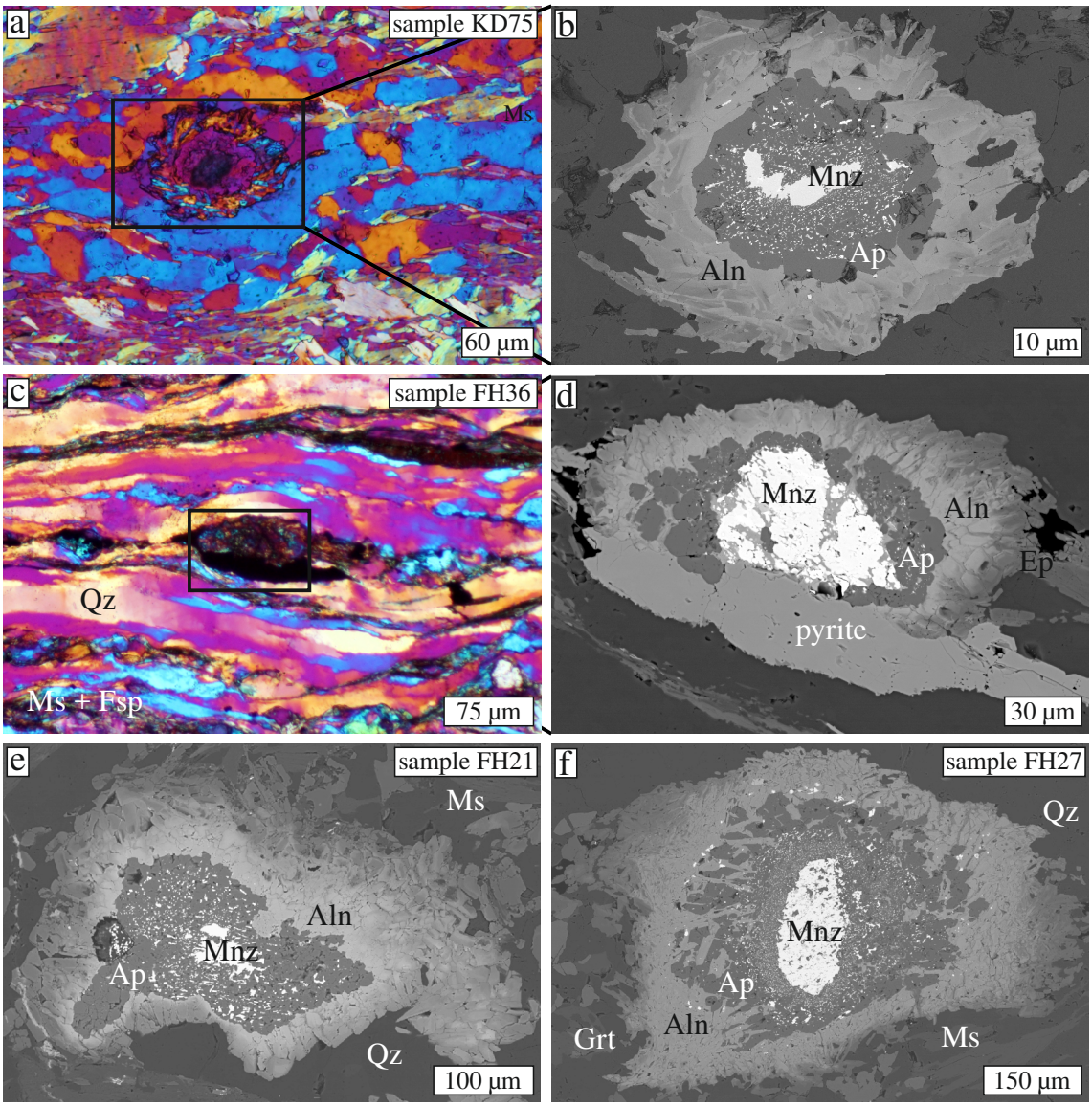

Figure 6.1: Micrographs of typical corona microstructures around monazite with apatite, allanite and epidote zones. **(a)** Polarized light micrograph with compensator plate inserted showing corona within mylonitic pegmatite (sample KD75). Note the quartz layers bent around the corona. **(b)** BSE image of the corona microstructure shown in (a). **(c)** Polarized light micrograph with compensator plate inserted showing corona around monazite in mylonitic pegmatite surrounded by pyrite (sample FH36). **(d)** BSE image of the corona microstructure shown in (c). **(e, f)** Corona microstructures chosen for detailed chemical and microstructural characterization and dating. All abbreviations for mineral names are from Whitney & Evans (2009).

6.2.2 Coronas around monazite

Monazite single crystals are surrounded systematically by a multiphase corona made of several tens of μm wide rims of apatite, and allanite, which is grading into epidote at the outer rim (Figs. 6.1; 6.2). Throughout the text the term epidote will refer to REE-poorer epidote-group minerals. These corona microstructures indicate partial

replacement of the monazite. The coronas are typically oblate shaped with long axes varying from 60 μm up to over 600 μm and an aspect ratio of up to 2 (Figs. 6.1; 6.2). The coronas are aligned within the mylonitic foliation, which is deflected around it (Figs. 6.1 a, c). The size and shape of the preserved mostly elongate monazites is generally very heterogeneous with long axes typically being a few tens of μm and reaching up to 200 μm (Figs. 6.1; 6.2). Elongate monazite cores are mostly but not necessarily aligned within the sample's foliation plane (compare e.g. Fig. 6.1 b and 6.1 f).

Locally apatite-allanite coronas without a monazite core are observed, either representing a non-centred cut of the corona structure or indicating complete replacement of monazite (Fig. 6.2 e, f). The size of the apatite zone around monazite is especially thin when the corona is included in tourmaline, indicating that the monazite is largely preserved (Fig. 6.2 a, b). In contrast, monazite grains in the mylonitic matrix (Fig. 6.1) or for example located near a quartz-filled crack within a tourmaline (Fig. 6.2 c, d) are largely replaced. The dependence of the degree of replacement on the local mineral assemblage is also documented by the largely missing apatite zone between monazite and pyrite in figure 6.1 d. The apatite and allanite/epidote zones are mostly broader parallel to the foliation and shorter perpendicular to it (Figs. 6.1, 6.2). Yet, the prismatic to columnar epidote crystals of the outer zone mostly grow with their long axes perpendicular to the apatite zone, also at a high angle to the foliation (Fig. 6.2 e, f). In some cases all of the outermost epidote grains grow parallel to the foliation (Fig. 6.1 b)

Two characteristic coronas around monazite in the samples FH21 (Fig. 6.1 e) and FH27 (Fig. 6.1 f) were chosen for detailed and geochronological investigation, which are described in the following.

The monazite core

The corona core from sample FH21 has an irregular outline with embayments and isolated patches surrounded by apatite (Figs. 6.1 e; 6.3). The elemental distributions show two compositionally different areas, which correlate with their EMP ages. The first domain (Mnz1) has higher contents in Ca, U and Y and lower in Si, La and Ce compared to the secondary domain (Mnz2). Thorium is distributed heterogeneously through the grain and microinclusions of thorite and apatite are found within monazite.

The monazite core from sample FH27 is with a long axis of about 200 μm one of the largest observed preserved monazite grains in the samples. It has an ellipsoidal shape (Figs. 6.1 f; 6.4) and many inclusions, mostly of apatite (high Ca content, Fig. 6.4 b), thorite (high Th, Fig. 6.4 d), pyrite, xenotime (high Y, Fig. 6.4 g) and quartz (high Si, Fig. 6.4 a). The relative distribution of elements within monazite is similar to that in FH21, with areas that have higher Ca, Y and U and lower Si, La and Ce. The latter areas are preferentially found at the rim but propagate heterogeneously through the grain.

From the measured U, Th, Pb contents (6.1), ages were calculated and are plotted in figure 6a. Calculating the distributions individually for each sample changed the results only slightly. Three different age populations were identified by the software NiLeDAM (Seydoux-Guillaume et al., 2012). The oldest one (Mnz1) has a mean age of 267 $\pm$ 4 Ma, in which the individual ages scatter between 250 and 285 Ma. This population is henceforth called "magmatic", as it corresponds well to the magmatic age of the pegmatites. About 10 % (3 of 32 measurements) of the measured points from FH27 show

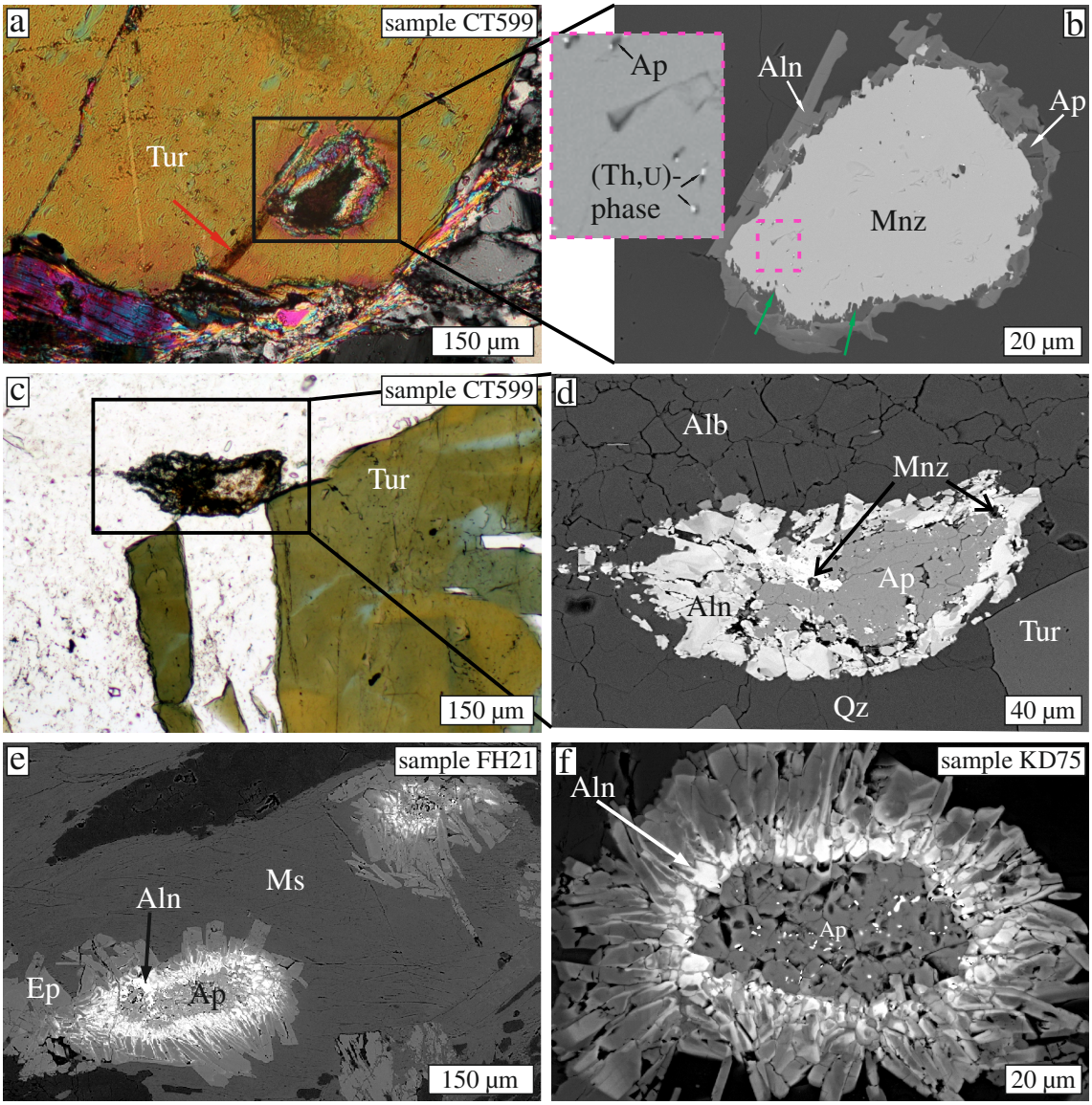

Figure 6.2: Coronas with varying relative proportions of apatite to monazite. **(a)** Polarized light micrograph with crossed polarizers showing monazite inclusion in tourmaline located near an intragranular crack (red arrow, sample CT 599). **(b)** BSE image of monazite inclusion shown in (a) with thin apatite and allanite rim. The stippled inset shows that apatite inclusions in the monazite are associated with (Th,U)-phases. **(c)** Polarized light micrograph and **(d)** corresponding BSE image showing corona microstructure located at a quartz-filled fracture of tourmaline (sample CT 599). **(e. f)** Corona microstructures without monazite core. Note especially the prismatic shape of and chemical zoning within the allanite/epidote grains.

magmatic ages and 60 % of the measured points from FH21 (9 of 15 measurements). The second population has a Mesozoic age of 196 ± 8 Ma, 10 % in FH27 and 47 % from FH21, which scatter between 170 and 210 Ma. The youngest population ages found only in FH27 scatter more widely between 20 and 120 Ma, with a mean age of 66 ± 6.

The measurements are grouped according to their EMP age (Fig. 6.3 h; 6.4 h; 6.5 a).

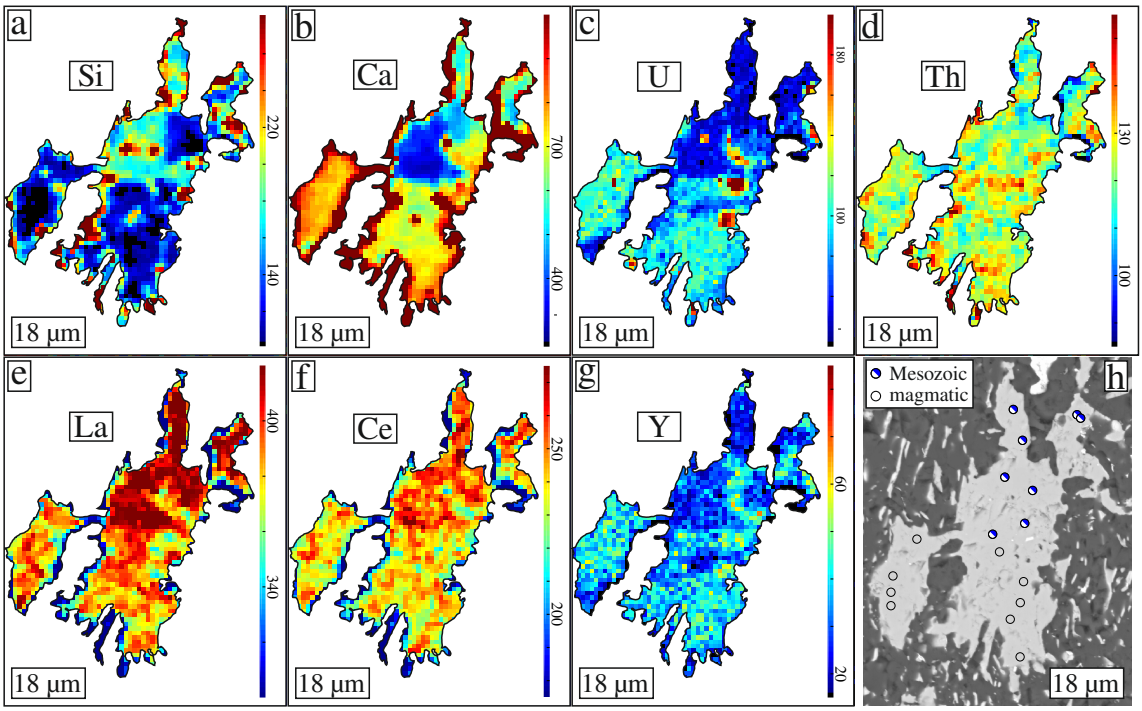

Figure 6.3: (a–g) Semi-quantitative element distribution maps for the monazite core from sample FH21, obtained by EMP (unit: counts; Fig. 6.1 e). **(h)** BSE image showing measurement points for EMP dating and their corresponding age population.

Table 6.1: Representative Monazite analyzes obtained by EMP

	FH21magm	FH21jur	FH27magm	FH27jur	FH27alp						
P_2O_5	30.50	29.87	30.89	30.18	29.94	P^{5+}	1.005	0.982	1.005	0.996	0.987
As_2O_3	0.27	0.24	0.23	0.25	0.21	As^{5+}	0.006	0.006	0.005	0.006	0.005
SiO_2	0.14	0.76	0.17	0.46	0.71	Si^{4+}	0.006	0.029	0.006	0.018	0.028
ThO_2	4.55	4.56	4.82	3.89	4.49	Th^{4+}	0.040	0.040	0.042	0.034	0.04
UO_2	1.55	0.19	3.77	1.30	0.36	U^{4+}	0.013	0.002	0.032	0.011	0.003
PbO	0.11	0.04	0.20	0.07	0.02	Pb^{4+}	0.001	0.000	0.002	0.001	0
Y_2O_3	2.01	1.16	2.81	2.63	0.99	Y^{3+}	0.037	0.021	0.051	0.048	0.018
La_2O_3	11.45	12.63	12.91	13.46	14.76	La^{3+}	0.164	0.181	0.183	0.193	0.212
Ce_2O_3	27.11	29.54	26.85	28.90	30.67	Ce^{3+}	0.386	0.420	0.378	0.412	0.437
Pr_2O_3	2.79	3.10	2.45	2.68	2.84	Pr^{3+}	0.040	0.044	0.034	0.038	0.04
Nd_2O_3	10.70	11.52	8.78	9.71	10.08	Nd^{3+}	0.149	0.160	0.120	0.135	0.14
Sm_2O_3	3.81	3.94	2.38	2.88	2.80	Sm^{3+}	0.051	0.053	0.031	0.039	0.038
Gd_2O_3	2.72	2.78	1.64	1.89	1.65	Gd^{3+}	0.035	0.036	0.021	0.024	0.021
CaO	1.57	0.54	2.12	0.88	0.58	Ca^{2+}	0.065	0.022	0.087	0.037	0.024
Total	99.26	100.86	100.01	99.18	100.11	Σ	1.999	1.996	1.999	1.994	1.993

Magmatic monazite from both coronas lie along the cheralite substitution line (Fig. 6.5 b). The composition of secondary monazite, generally, is shifted towards the substitution line to huttonite (Fig. 6.5 b), which for example reflects the lower Ca and higher Si contents in the metamorphic domains (Fig. 6.3). The difference in composition between primary and secondary monazite is also reflected in the REE-composition (Fig. 6.5 c).

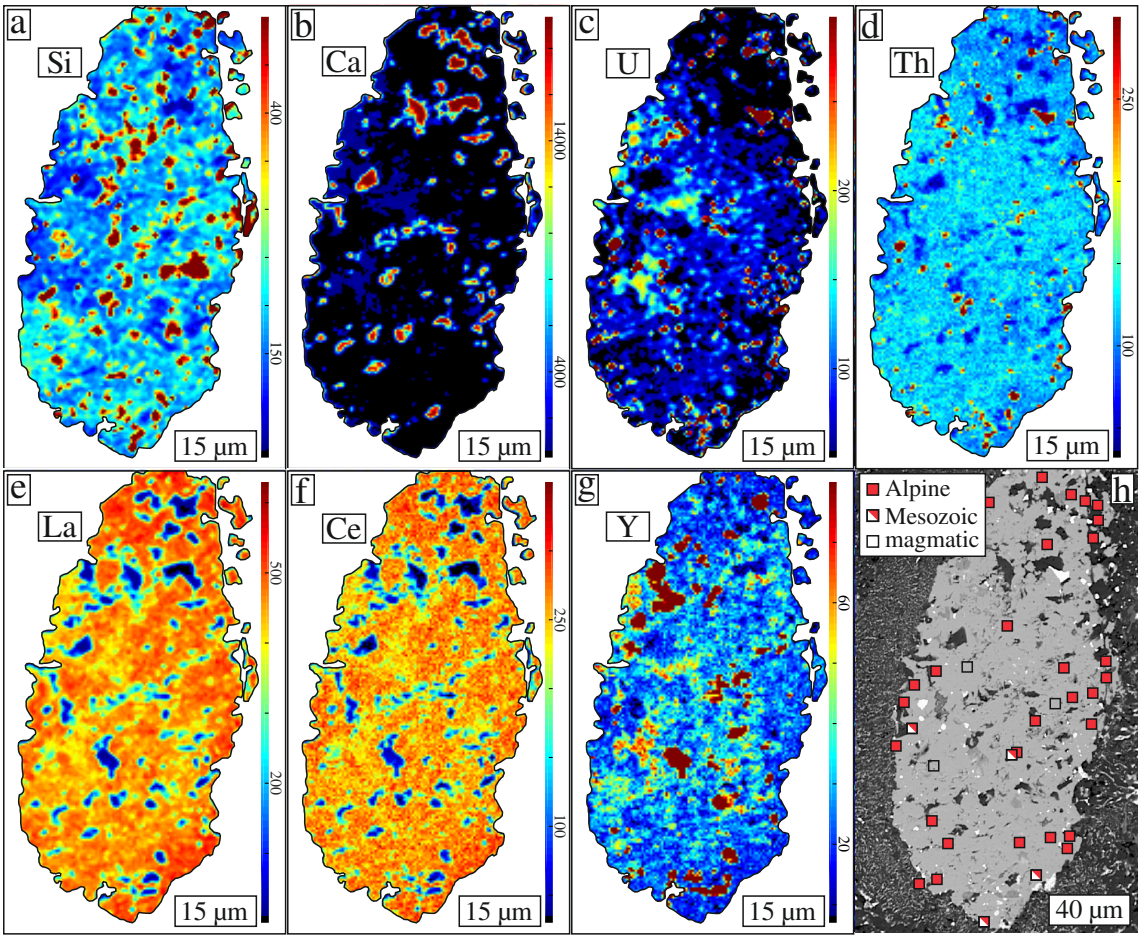

Figure 6.4: (a–g) Semi-quantitative element distribution maps for the monazite core from sample FH27 (unit: counts; Fig. 6.1 f). **(h)** BSE image showing measurement points for EMP dating and their corresponding age population.

Magmatic monazite has the highest HREE/LREE-ratios, but the lowest REE-content. The Th/U ratios are generally low (< 30), especially for the magmatic domains, where UO_2 reaches few % (compare Fig. 3 from Grand'Homme et al., 2016). The original low Th/U ratios and the very high U contents – up to 30000 ppm, often above 10000 – are a prerequisite for chemical dating of the Alpine monazite population.

The apatite zone

The apatite zone directly surrounds the monazite core (Fig. 6.6). It consists of isometric grains that have a polygonal shape (Fig. 6.1 b). The grain sizes generally increases outwards, from as small as < 1 μm adjacent to the monazite core up to 30 μm at the outer apatite rim (Fig. 6.6). This change in grain size might be smooth or have pronounced steps. Thorite occurs as small (< 1 μm–10 μm) grains dispersed between and as inclusions in apatite grains (Fig. 6.6). Most of the thorite grains occur in the innermost part of the apatite zone. Allanite is present in the apatite zone in varying amounts. It occurs as thin film a long g rain b oundaries o r a t t he e dge b etween three apatite grains (Fig. 6.6). The boundary to the allanite zone might be sharp as in the corona of samples FH21 and KD75 (Figs. 6.1 b, e; 6.6 a) or more diffuse with

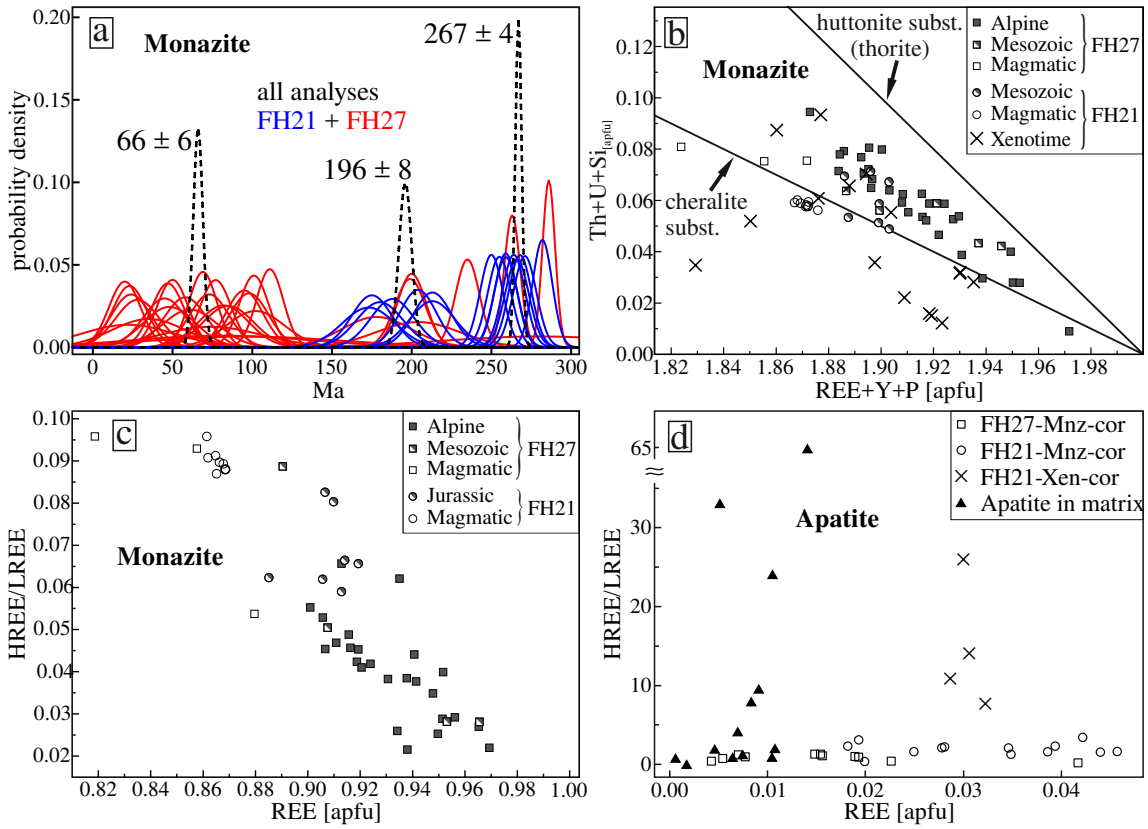

Figure 6.5: (a) Age distribution diagram for monazite points from both FH21 & FH27. The mean population ages and errors were calculated using the software NiLeDAM (Seydoux-Guillaume et al., 2012). **(b)** Substitution diagram showing the composition of monazite and xenotime from the three coronas. The two lines represent two substitutions towards the endmembers cheralite (brabantite): Ca + (Th,U) = 2REE and huttonite: Si + (Th,U) = REE + P. **(c)** REE-composition of monazite. Xenotime has much higher and uniform HREE/LREE ratios and is not shown here. **(d)** REE-composition of apatite from the two monazite coronas, the xenotime corona and apatites from the matrix from both samples. 10 measurements of apatite from xenotime coronas have LREE contents below the detection limit and are not shown here.

allanite grains protruding into the apatite zone as in the corona of sample FH27 (Fig. 6.1 f). Generally, the grain boundaries of the outermost apatite grains towards allanite are straight and even. In contrast, the boundary towards the monazite zone is always irregular with many embayments and protrusions of apatite into monazite (Figs. 6.3 h; 6.4 h). In the corona of sample FH21 elongated islands of monazite occur in the apatite zone (Fig. 6.3 h).

The REE-composition of apatite is shown in table 6.2 & figure 6.6 b and compared to apatite grains from the matrix of both samples. The REE-content of apatite from the coronas varies between 0.003 and 0.047 atoms per formula unit. The spatial distribution of the REE-contents is random and no difference between the inner and outer subzone in FH27 exists. The HREE/LREE-ratios are uniform and low. In contrast, grains from the rock's matrix have generally lower REE-contents below 0.011 and strongly varying HREE/LREE-ratios.

Table 6.2: Representative Apatite analyzes obtained by EMP

	FH27mon	FH21mon	FH21xen	FH21matrix	FH27matrix						
SO3	0.02	0.01	0.00	0.01	0.01	S^{6+}	0.001	0.001	0	0.001	0.001
P_2O_5	43.31	41.96	42.33	42.58	43.12	P^{5+}	2.957	2.903	2.878	2.998	3.032
As_2O_3	0.00	0.04	0.00	0.00	0.02	As^{5+}	0	0.002	0.000	0	0.001
SiO_2	0.01	0.20	0.49	0.19	0.04	Si^{4+}	0.001	0.016	0.040	0.015	0.003
ThO_2	0.06	0.03	0.00	0.00	0.00	Th^{4+}	0.001	0.000	0	0	0
UO_2	0.04	0.00	0.00	0.01	0.00	U^{4+}	0.001	0	0	0.000	0
PbO	0.00	0.04	0.01	0.00	0.00	Pb^{4+}	0	0.001	0.000	0	0
Y_2O_3	0.25	0.36	0.76	0.08	0.14	Y^{3+}	0.009	0.014	0.029	0.003	0.006
La_2O_3	0.09	0.07	0.02	0.00	0.02	La^{3+}	0.003	0.002	0.000	0	0.001
Ce_2O_3	0.16	0.18	0.00	0.04	0.00	Ce^{3+}	0.005	0.006	0	0.001	0.000
Pr_2O_3	0.02	0.08	0.02	0.00	0.02	Pr^{3+}	0.001	0.002	0.001	0	0.000
Nd_2O_3	0.06	0.06	0.00	0.01	0.00	Nd^{3+}	0.002	0.002	0	0.000	0
Sm_2O_3	0.00	0.06	0.00	0.00	0.01	Sm^{3+}	0	0.002	0	0	0.000
CaO	57.74	57.50	58.39	55.71	55.50	Ca^{2+}	4.989	5.035	5.024	4.964	4.940
SrO	0.15	0.07	0.03	0.12	0.25	Sr^{2+}	0.007	0.003	0.001	0.006	0.012
FeO	0.05	0.16	0.17	0.07	0.04	Fe^{2+}	0.004	0.011	0.011	0.005	0.003
MnO	0.08	0.02	0.02	0.04	0.05	Mn^{2+}	0.011	0.003	0.002	0.005	0.007
Na_2O	0.06	0.05	0.08	0.00	0.03	Na^{+}	0.009	0.008	0.013	0.001	0.004
F	3.80	4.53	4.93	4.73	3.24	F	0.970	1.172	1.253	1.245	0.850
Cl	0.01	0.00	0.00	0.01	0.04	Cl	0.002	0.000	0	0.001	0.005
Total	105.92	105.44	107.25	103.60	102.52	Σ	8.972	9.182	9.253	9.246	8.867

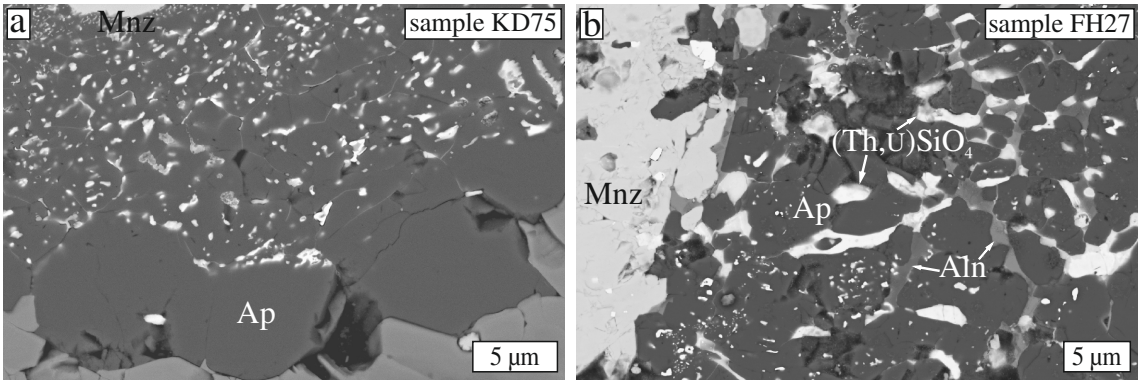

Figure 6.6: (a) The apatite zone of the corona from sample KD75 (compare Fig. 6.1 b). **(b)** The innermost part of the apatite zone in the corona from FH27 (compare Fig. 6.1 f).

The allanite/epidote zone

The allanite/epidote zone surrounds the apatite zone. The complex structure of this zone varies between different coronas. The allanite in the innermost zone at the contact to apatite are often isometric. The outermost epidote grains often are elongate and form a concentric radiating palisade-like structure (Figs. 6.1 b; 6.2). In the allanite/epidote zone, the HREE/LREE-ratio increases and the REE-content decreases from the apatite zone towards the outside of the corona (Fig. 6.7 b). In the outermost part, the composition corresponds to Y-rich epidote (Fig. 6.7 b).

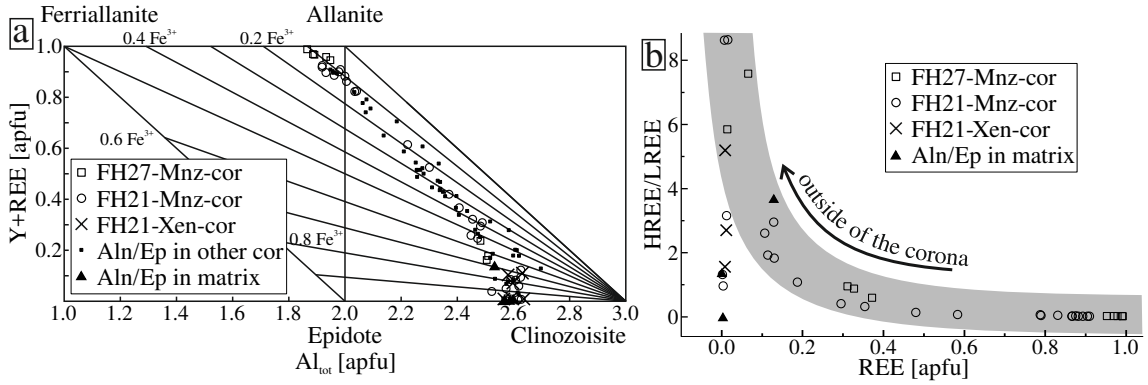

Figure 6.7: Chemical composition of REE-bearing epidote group minerals. **(a)** REE +Y vs. Al_{tot} diagram (after Petrík et al., 1995) and **(b)** in a REE-composition diagram (Epidote-group-minerals in xenotime coronas have higher HREE/LREE-ratios of 28; 40 & 117 and are not shown in this diagram)

In the corona from FH21 a small compositional gap exists between allanites (XAln=0.8–0.9) and epidote of lower REE-contents (XAln < 0.6). This gap is much wider in FH27 (with XAln = 0.95–1.0 and XAln < 0.4, respectively). The composition of allanite in other coronas, which do not contain any monazite, occupies the whole compositional range of Aln fraction from 0 to 100 % in the epidote group mineral (Fig 6.7 a). Therefore, a distinction between an allanite and a separate epidote zone is not done here. Allanite/epidote grains are usually also zoned internally as well, with both normal (REE-rich to poor) and inverse zoning (Fig. 6.8). Compositional zoning can also be patchy. Epidote-group minerals that occur in the matrix of samples FH21 and FH27 have low REE-contents between 0.2 [apfu] and varying HREE/LREE ratios (Fig 6.7 a).

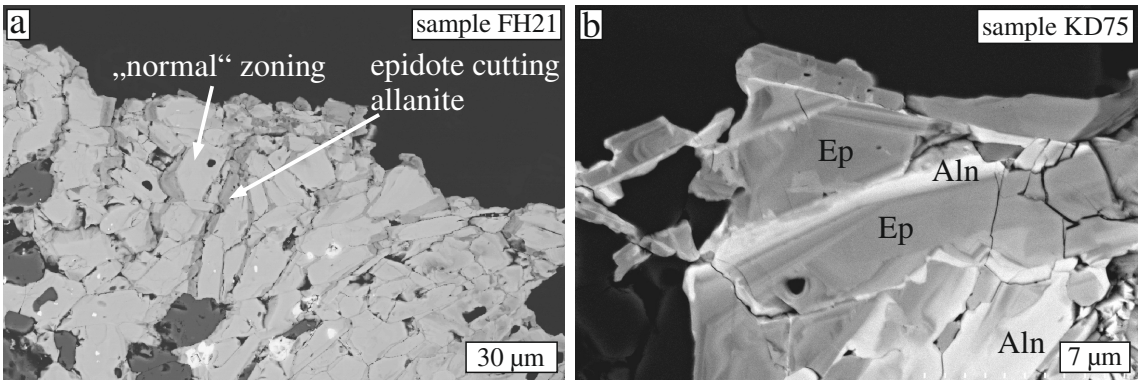

Figure 6.8: BSE images of the allanite/epidote zone in the coronas from FH27 **(a)** and FH21 **(b)**, showing the shape and zoning (oscillatory and reverse) of allanite grains.

6.2.3 Coronas around xenotime

Xenotime is not as common as monazite but if it occurs, it shows similar corona structures (Fig. 6.9). Xenotime in the center of the corona is accompanied by small zircon grains and is surrounded by apatite and HREE-bearing epidote-group minerals. Thorite (U-bearing) occurs in channels and voids in the xenotime core (Fig. 6.9 c, d). Some of the

Table 6.3: Representative Allanite and Xenotime analyzes obtained by EMP

	Allanite							**Xenotime**	
sample	FH21 mon-cor		FH27 mon-cor		FH21 xen-cor	FH21		FH21 xen-cor	FH21 xen-cor
Type	high REE	low REE	high REE	low REE	FH21xen	matrix		FH21magm	FH21tri
SiO_2	31.02	38.81	31.54	37.85	38.16	37.82	SO_3	0.02	0.02
TiO_2	0.07	0.00	0.02	0.01	0.02	0.04	P_2O_5	35.05	35.55
Al_2O_3	17.35	27.36	18.15	27.49	27.68	27.69	SiO_2	0.56	0.30
FeO	12.47	7.81	11.47	5.79	5.91	5.94	ThO_2	0.59	0.23
MnO	0.16	0.11	0.24	0.19	0.15	0.10	UO_2	2.48	1.38
MgO	0.10	0.02	0.15	0.00	0.00	0.00	PbO	0.10	0.04
CaO	10.13	22.48	11.52	22.80	22.38	24.29	Y_2O_3	40.43	41.66
Na_2O	0.00	0.00	n.d.	n.d.	0.00	0.00	La_2O_3	n.d.	n.d.
SrO	0.00	0.00	0.00	0.00	0.00	0.00	Ce_2O_3	n.d.	n.d.
PbO	0.03	0.04	0.07	0.09	0.02	0.00	Pr_2O_3	n.d.	n.d.
ThO_2	0.42	0.01	1.10	0.00	0.01	0.00	Nd_2O_3	0.75	0.49
UO_2	0.00	0.00	0.01	0.08	0.02	0.00	Sm_2O_3	1.27	1.21
Y_2O_3	0.13	0.59	0.28	1.47	2.20	0.00	Eu_2O_3	0.02	0.03
La_2O_3	6.55	0.03	5.68	0.00	0.00	0.02	Gd_2O_3	3.87	3.95
Ce_2O_3	13.10	0.09	11.40	0.01	0.03	0.00	Dy_2O_3	7.14	7.38
Pr_2O_3	1.18	0.00	1.27	0.02	0.01	0.02	Ho_2O_3	0.92	0.90
Nd_2O_3	3.44	0.07	3.46	0.02	0.00	0.05	Er_2O_3	2.85	2.90
Sm_2O_3	0.68	0.13	0.73	0.10	0.05	0.00	Yb_2O_3	1.75	1.76
Gd_2O_3	0.30	0.12	0.31	0.13	0.26	0.00	Lu_2O_3	0.23	0.23
Dy_2O_3	0.00	0.00	n.d.	n.d.	0.00	0.00	CaO	0.36	0.22
Ho_2O_3	0.00	0.00	n.d.	n.d.	0.00	0.00	Total	98.40	98.40
Er_2O_3	0.00	0.00	n.d.	n.d.	0.00	0.00			
Total	97.13	97.68	97.40	96.03	96.91	95.97	S^{6+}	0.001	0.001
							P^{5+}	1.034	1.044
Si^{4+}	3.009	3.036	2.873	3.013	3.018	2.978	Si^{4+}	0.019	0.010
Al^{3+}	0	0	0.127	0	0	0.022	Th^{4+}	0.005	0.002
Σ T	3.009	3.036	3.000	3.013	3.018	3.000	U^{4+}	0.019	0.011
Ti^{4+}	0.005	0	0	0	0	0	Pb^{4+}	0.001	0.000
Fe^{3+}	0.010	0	0	0	0	0	Y^{3+}	0.662	0.679
Al^{3+}	0.985	1.000	0.736	0.977	0.973	0.948	La^{3+}	n.d.	n.d.
Σ M1	1.000	1.000	0.736	0.977	0.973	0.948	Ce^{3+}	n.d.	n.d.
Al^{3+}	1.000	1.000	1.000	1.000	1.000	1.000	Pr^{3+}	n.d.	n.d.
Σ M2	1.000	1.000	1.000	1.000	1.000	1.000	Nd^{3+}	0.009	0.006
Al^{3+}	0.000	0.522	0.086	0.602	0.608	0.600	Sm^{3+}	0.015	0.014
Ti^{4+}	0	0	0.002	0.000	0.001	0.002	Eu^{3+}	0.000	0.000
Fe^{3+}	0.077	0.369	0.140	0.330	0.280	0.391	Gd^{3+}	0.045	0.045
Mg^{2+}	0.014	0.002	0.020	0.000	0.000	0.000	Dy^{3+}	0.080	0.082
Fe^{2+}	0.909	0.106	0.734	0.056	0.111	0.000	Ho^{3+}	0.010	0.010
Mn^{2+}	0	0	0.018	0.013	0	0.007	Er^{3+}	0.031	0.032
Σ M3	1.000	1.000	1.000	1.000	1.000	1.000	Yb^{3+}	0.019	0.019
Na^{+}	0.000	0.000	0.000	0.000	0.000	0.000	Lu^{3+}	0.002	0.002
Ca^{2+}	0.971	0.957	1.000	1.000	0.990	1.000	Ca^{2+}	0.013	0.008
Mn^{2+}	0.014	0.007	0	0	0.010	0	Σ	1.967	1.966
Fe^{2+}	0.015	0.036	0	0	0	0			
Σ A1	1.000	1.000	1.000	1.000	1.000	1.000			
Pb^{2+}	0.001	0.001	0.002	0.002	0.000	0.000			
Sr^{2+}	0.000	0.000	0.000	0.000	0.000	0.000			
Ca^{2+}	0.081	0.927	0.124	0.944	0.907	1.049			
Th^{4+}	0.009	0.000	0.023	0.000	0.000	0.000			
U^{4+}	0.000	0	0.000	0.001	0.000	0.000			
Y^{3+} + REE	0.900	0.037	1.115	0.062	0.102	0.003			
Σ A2	0.991	0.964	1.264	1.010	1.010	1.052			

voids appear to have negative crystal shapes (Fig. 6.9 d). The apatite grains, surrounding the xenotime have an isometric, polygonal shape and a size of 5–15 μm. They have a uniform REE-content of 0.026 to 0.038 apfu, with high HREE and negligible LREE, compared to the monazite coronas (Fig. 6.5 d). Apatite is surrounded by one, slightly zoned, blade-shaped epidote crystal (Fig. 6.9 b). It contains very little REE (Fig. 6.7), but can have up to 0.07 apfu of Gd and 0.1 apfu of Y.

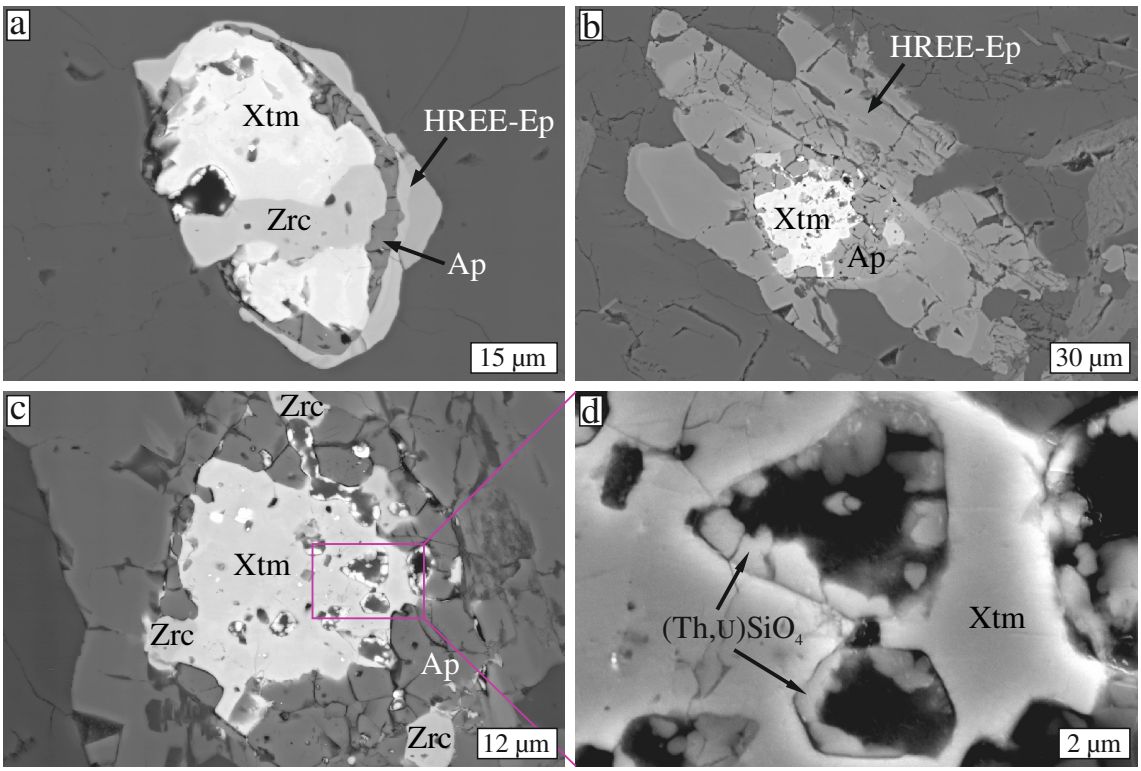

Figure 6.9: BSE images of the xenotime coronas from sample FH21. **(a)** Incipient replacement of a xenotime grain accompanied by zircon. **(b)** corona, on which the compositional measurements were done. **(c)** Close-up of the xenotime core from (a), also showing the polygonal apatite grains. **(d)** Close-up of voids, which are partly filled with thorite at their edges.

All measurements were obtained from the corona in figure 6.9 b, c, d. The composition of xenotime is shown in figure 6.5 b. Regarding the actinides, it incorporates less Th but significant U, with lower Th/U, compared to monazite. The EMP age distribution for xenotime is shown in figure 6.10 a. Two populations were found with three points in them each: one at 287 Ma and one at 205 Ma, very similar to the monazite from FH21. The determined EMP ages seem to correlate with the Th/U-ratio, with magmatic domains (Xen1) tending to have higher Th/U compared to domains with Mesozoic ages (Xen2; Fig. 6.10 b).

6.2.4 Crystallographic relationships

In the coronas from sample FH21, EBSD measurements were collected from monazite, xenotime and apatite to investigate possible orientation relationships between the minerals in the corona, especially between apatite and monazite/xenotime. To avoid major

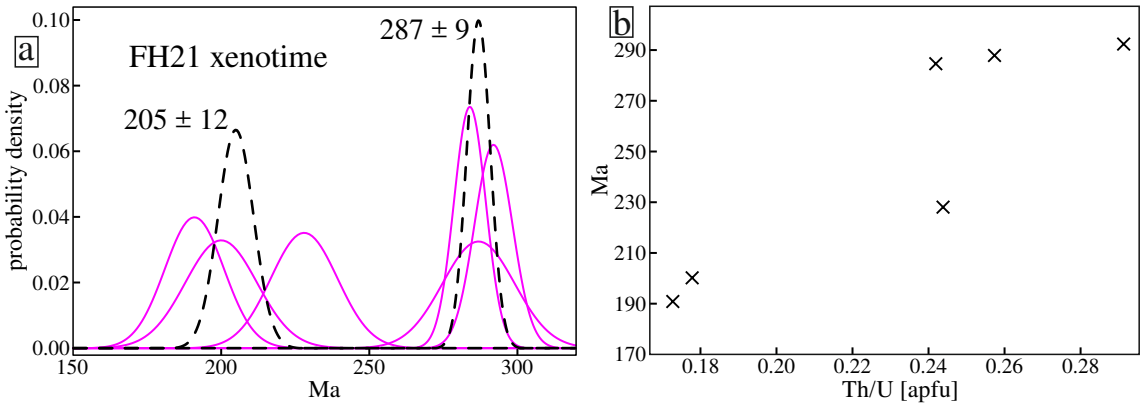

Figure 6.10: (a) Age distribution diagram for six measured xenotime points from sample FH21 (Fig. 10). **(b)** Age vs. Th/U diagram.

artefacts from misindexing, manually set point measurements were collected, allowing the focus to be adjusted for every single measurement. Attention was paid to an unbiased distribution of points. The EBSD measurement locations and pole figures showing the orientation of monazite and apatite from the FH21 corona are shown in figure 6.11.

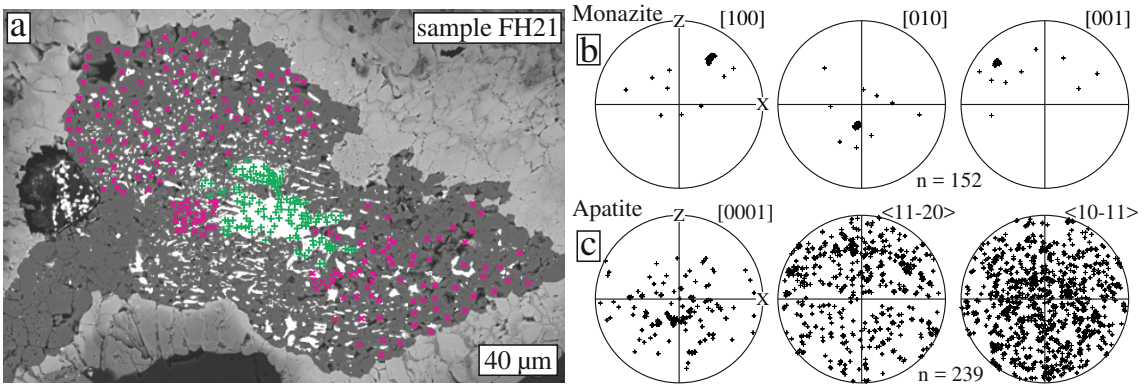

Figure 6.11: EBSD point measurements on apatite and monazite. **(a)** BSE image showing the measurement locations, pink for apatite and green for monazite. **(b, c)** Pole figures (equal angle projection of the lower hemisphere) for monazite (b) and apatite (c).

The monazite has an uniform orientation, as have the small isolated islands (c.f. Fig. 6.3 h). The outliers are randomly distributed and are probably due to misindexing. The c-axes of apatite crystals scatter around the b-axis of the monazite crystal. The crystallographic orientation of both xenotime and apatite is shown in figure 6.12. Apatite c-axes largely scatter around the c-axis of the xenotime single crystal.

6.2.5 LA-ICP-MS U/Th-Pb dating of allanite

In the monazite corona of sample FH27, allanite was dated by LA-ICP-MS (figure 6.13). The common lead fractions are relatively high (f206 = 0.86–0.97; f208 = 0.86–0.99), requiring a common lead correction. The uncorrected Tera-Wasserburg and Th-isochron diagrams are shown in figure 6.13 a; b. The intercept age in the U-Pb system is 49 ± 18 Ma and the Th-isochrone age is 69 ± 14. The corrected ages (using the common lead

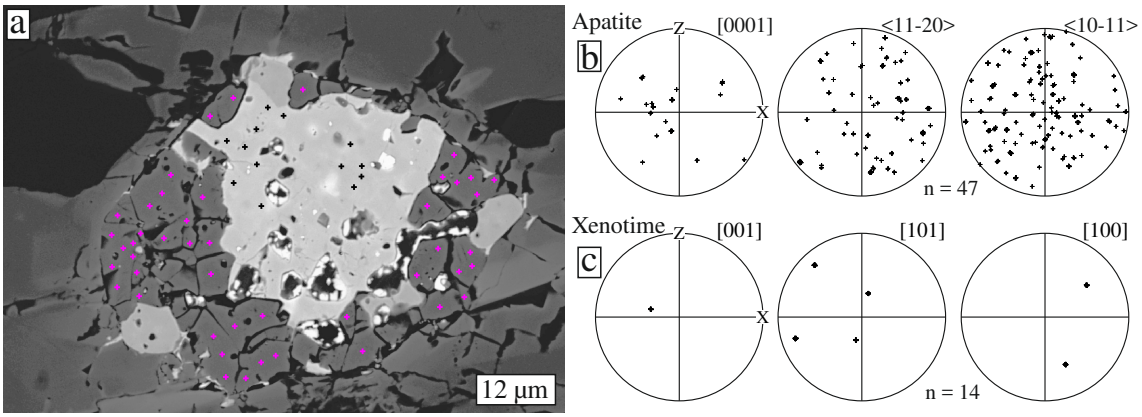

Figure 6.12: EBSD point measurements on apatite and xenotime. **(a)** Shows the measurement locations, pink for apatite and black for xenotime. **(b, c)** Show the pole figures (equal angle projection of the lower hemisphere) for apatite (b) and xenotime (c).

composition values given in figure 6.13 a; b) are 51 ± 8 and 60 ± 6 Ma for the U-Pb and Th-Pb systems, respectively.

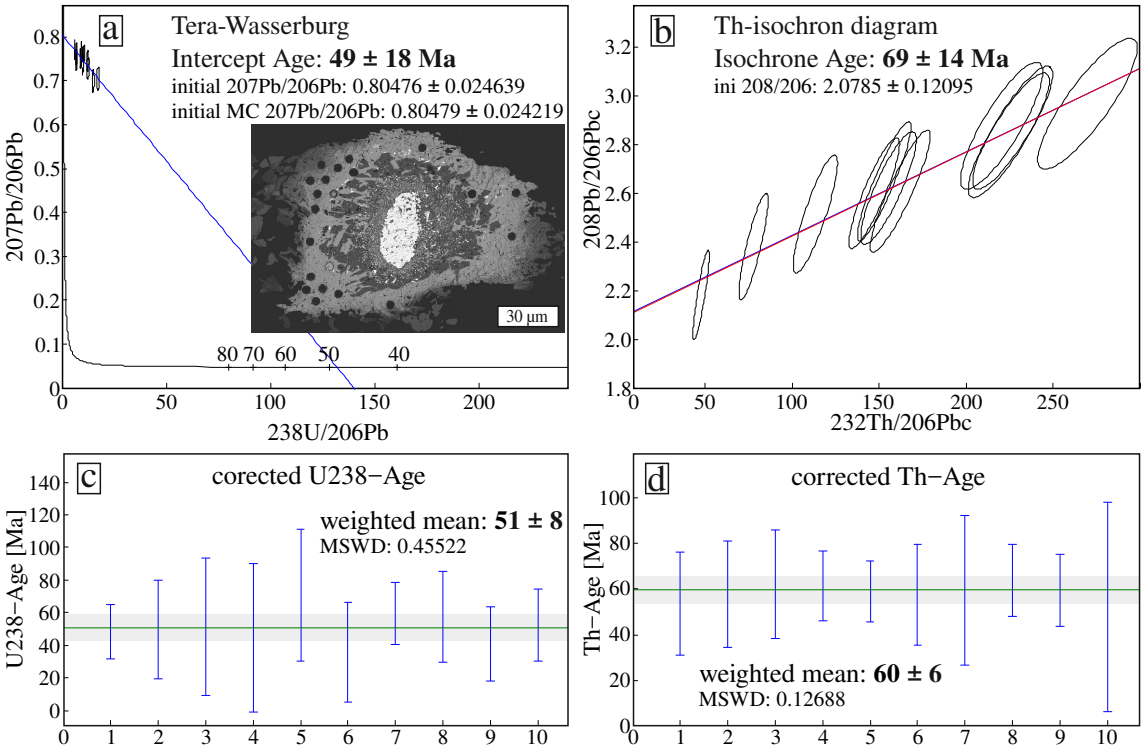

Figure 6.13: **(a)** Tera-Wasserburg and **(b)** Th-Pb-Isochrone diagram for allanite from sample FH27. **(c, d)** U- and Th-ages of the measurement points after correction for common lead.

6.3 Discussion

6.3.1 Age and formation of secondary monazite and xenotime

Different approaches to date the minerals that form the coronas, i.e. monazite, xenotime and allanite were used. Monazite and xenotime were dated by the chemical method by EMP, whose high spatial resolution allows different growth domains to be to differentiated within single crystal corona cores. The age of allanite in the corona was obtained by U/Th-Pb dating of allanite using LA-ICP-MS with a 24 μm laser diameter.

Primary Permian ages at 267 ± 4 Ma and 287 ± 9 Ma were found for Mnz1 and Xen1, respectively (Fig. 6.5 a, 6.10 a). Thus the magmatic age reported for the pegmatites from this area (Borsi et al., 1980; Knoll et al., 2018) are supported by the data presented here. This suggests that chemical EMP dating is a robust method to identify and date crystallization ages of monazites and xenotime, though both minerals are altered and modified during deformation under greenschist facies conditions.

In the investigated coronas secondary monazite (Mnz2) or xenotime (Xen2), respectively, occur. The chemical changes accompanying the formation of secondary monazite in coronas are such that the altered domains (Mnz2) have less Y, Pb, U and Ca, but are enriched in REE and Si compared to primary monazite Mnz1 (Figs. 6.3; 6.4; Table 6.1). Secondary monazite might have a lower or higher Th content than primary monazite (Figs. 6.3 & 6.4). Similar chemical changes were found in alteration experiments by various authors (e.g. Budzyń et al., 2011; Grand'Homme et al., 2018). In all samples, the crystallographic orientation of primary and secondary monazite and xenotime is the same, which indicates crystallographic continuity across the alteration interface. This crystallographic continuity is typical for interface-coupled dissolution-precipitation reactions (Putnis, 2009) and has been observed in experiments on monazite (Harlov et al., 2011; Grand'Homme et al., 2018).

The alteration characteristics in the monazite coronas differ slightly. In the corona of sample FH21 primary and secondary monazite are clearly separated into two domains, forming, essentially, a core-and-rim pattern (Fig. 6.3). Additionally, some satellite monazites occur as elongated islands in the apatite zone (Fig. 6.3 h). In the corona from sample FH27, secondary monazite is unevenly distributed, although more of it occurs at the rim of the monazite (Fig. 6.4). Comparable structures, albeit on a smaller scale, have been found in alteration experiments on monazite, using NaOH-rich fluids (Grand'Homme et al., 2016, 2018). In these cases, the replacement proceeds along nm-sized channels, which result in a nano-scale mixture of unaltered and altered material. It might be possible that the microstructure found in sample FH27 resulted from alteration, in which the fluids travelled along irregular channels, rather than forming just a rim around unaltered crystal, like usually found for dissolution-precipitation processes (e.g. Putnis, 2009).

Ages obtained from monazite produced by fluid-mediated alteration are difficult to interpret. During experimental replacement, the U/Th-Pb behavior in altered monazite is complex and depends on the reaction mechanism (Seydoux-Guillaume et al., 2002; Harlov et al., 2011; Grand'Homme et al., 2016), and on physicochemical parameters (fluid speciation, temperature). While Pb incorporation is normally negligible in altered

domains, it can also reach significant concentrations (Seydoux-Guillaume et al., 2002; Budzyń et al., 2011; Harlov et al., 2011), especially at low temperature (Grand'Homme et al., 2016). This means that the radiometric clock is not set to zero in altered monazite. Grand'Homme et al. (2016, 2018) found that, although secondary monazite contains no structural Pb, primary unaltered monazite occurs with secondary monazite in altered domains at the nanoscale due to incomplete replacement. This nanomixture is not resolvable by the spatial resolution of the EMP, which gives an intermediate age between primary and experimentally altered secondary monazite. As the fraction of primary monazite in the nanomixtures decreases with alteration temperature, higher temperatures lead to a more complete Pb removal and to a higher resetting of the U-Th-Pb system (Grand'Homme et al., 2016). This incomplete resetting in altered domains is proposed to explain discordant ages and age scatter in natural samples (Bosse et al., 2008; Kelly et al., 2012; Didier et al., 2013).

In the corona from sample FH21, altered and unaltered monazite are spatially separated and almost no inclusions or porosity is present. In this corona, only two age populations are found: Magmatic and Mesozoic. In FH27, secondary and primary monazite are intimately mixed and inclusions and microporosity are present, which might indicate incomplete alteration (Grand'Homme et al., 2016). Scattering ages with three populations were found: Late-Variscan magmatic, Mesozoic and Alpine (Fig. 6.5 a). Although the Alpine ages are scattered, they give an average at 66 ± 4 Ma (Fig. 6.5 a), which compares very well to the 60 ± 10 Ma allanite age obtained in the same corona (Fig. 6.13 d). This indicates coeval formation of a secondary monazite population and formation of the corona microstructure.

The significance of the Mesozoic age in both monazite and in xenotime with 196 ± 8 Ma and 205 ± 12 Ma (Figs. 6.5 a; 6.10 a), respectively, is more difficult to interpret. As it has no specific chemical signature, like the Magmatic (lower REE; higher HREE/LREE) and the Alpine (higher REE; lower HREE/LREE) populations, it might compositionally be a mixture of these two, indicating incomplete replacement during alpine times. Therefore, it remains unclear, if the Mesozoic age represents a discrete alteration event or a mixed primary and Alpine age.

Electron microprobe dating of xenotime has much more rarely been done than on monazite. To the author's knowledge, this study present the first ages obtained by chemical dating for xenotime within corona structures. The fact that the xenotime ages are well consistent with the monazite ages (compare Figs. 6.5 a; 6.10 a) shows that this method is just as reliable and cost- & time-effective.

6.3.2 Monazite and xenotime breakdown reactions

Monazite breakdown reactions into allanite-apatite-coronas have been described to happen during postmagmatic cooling (Broska et al., 2005; Petrík & Konečný, 2009), during prograde metamorphism from greenschist-to-amphibolite-facies conditions (Broska & Siman, 1998; Finger et al., 1998) and during retrograde metamorphism to greenschist-facies conditions (Lo Pò et al., 2016). Coronas around xenotime are much less frequently described (e.g. Broska et al., 2005). Experiments have shown that fluid composition plays a major role for monazite breakdown and the resulting product minerals (Seydoux-

Guillaume et al., 2002; Budzyń et al., 2011, 2017; Mair et al., 2017). Ca-rich fluids produce apatite and allanite (Budzyń et al., 2011, 2017), whereas Na- or even K-rich fluids may lead to dissolution and the precipitation of new monazite (Budzyń et al., 2011; Grand'Homme et al., 2018) but not allanite and apatite. Thus, in general, a high Ca/Na-ratio leads to the stabilization of allanite + apatite relative to monazite. Fluids rich in CO_2, apart from fluorine, may also lead to the formation of REE-rich carbonates, like hydroxylbastnäsite (Ondrejka et al., 2012). However, these experimental settings are strongly deviating from the natural conditions in the pegmatites described here. The observations presented here consistently indicate the breakdown of monazite and xenotime following generalized reaction as follows:

$$Mnz1+(Si,Ca,Al,Fe,F)fluid \rightarrow Mnz2+LREE-Ap+Aln/REE-Ep+(Th,U)SiO_4$$

$$Xen1+(Si,Ca,Al,Fe,F)fluid \rightarrow Xen2+HREE-Ap+HREE-Ep+Ep+(Th,U)SiO_4$$

Phosphorus is directly incorporated into apatite, Th and U are mostly captured in thorite and REE mostly in allanite, and in a lesser extent into apatite. Monazite breakdown leads to a fractionation of the REE. Allanite closest to the center of the corona (i.e. with the highest REE-contents) has the lowest HREE/LREE ratios. This trend is similar to that observed by Finger et al. (1998). Apatite and epidote in the coronas contain more REE than the same minerals in the mylonitic matrix do. This difference may indicate restricted transport of REE within the fluid phase in relation to their solubility at the given temperature conditions and possibly also a restricted and/or episodic availability of fluids at thin section scale.

Thorium and U seem to have the lowest solubility in the fluid phase, because (a) thorite is usually found in the apatite zone and (b) small thorite grains occur together with apatite inclusions in incipiently replaced monazites (Fig. 6.2 b). This shows that these elements are mostly immobilized by thorite precipitation and are only incorporated into allanite or apatite in very small amounts. This restricted transport of Th in the fluid phase compared to REEs has been observed in corona structures (e.g. Broska et al., 2005; Ondrejka et al., 2012) and during the alteration of granites (Förster, 2000).

The corona around xenotime shows a similar element distribution, except that no REE-fractionation is indicated. Like in the monazite coronas, phosphorus is incorporated into apatite and Th and U into thorite. Most of the thorite occurs in channels and voids inside the xenotime core and the apatite zone (Fig. 6.9 c, d).

Finger et al. (1998) was able to perform mass balance calculations on similar corona structures around monazite and found that the coronas essentially represent "diluted monazite", which means that most of the material from the original monazite did not escape outside of the corona structure. Due to the uncircularity of the coronas observed here, uncertainties in the determination of the mineral fractions and maybe the effect of non-central cutting, the same results were not achieved here. But as the element distribution and microstructure of the coronas is similar to those for which such calculations were done (Finger et al., 1998; Upadhyay & Pruseth, 2012), it is likely that not much material (REE, P, Th, U) was lost to the outside of the corona in the samples from this study as well, which is consistent with the different apatite REE-composition inside the

corona and outside in the mylonitic matrix.

Generally, cutting effects in 2D images of the 3D corona microstructure make it difficult to assess the true proportions of the different mineral phases. Yet, as a first approximation, the relative proportions of apatite to monazite within the images is taken as indication of the amount of replacement. The higher the relative apatite to monazite proportion, the higher the suggested degree of replacement of monazite. The observation that monazite inclusions in tourmaline are largely preserved (Fig. 6.2 a, b) as opposed to the replacement by apatite/allanite/epidote in the matrix (Fig. 6.2 c–f), is most likely due to restricted pathways for fluids in the tourmaline inclusion. This dependence of degree of replacement on the local surrounding microfabric indicates that fluid availability along grain boundaries in the matrix and cracks controls the reaction advancement, by allowing the elementary mass transfer required for the corona reaction (Ca, Al, Si, Fe).

As discussed above, the presence of a fluid is a prerequisite for the breakdown of monazite and xenotime, however, the source, availability and composition of the fluid remains difficult to assess. The question of open or closed system is a matter of scale. Here, pegmatite bodies that are usually of the size of a few meters were used as reference system, which underwent metamorphic reactions in the presence of fluids during the alpine orogeny (Stöckhert, 1987; Hofmann et al., 1983; Hentschel et al., 2019). Mn-poor garnet grew on the expense of magmatic Mn-rich garnet, but replacement of garnet by chlorite is only minor. Some Fe-bearing white mica as well as biotite formed, partly at the expense of magmatic muscovite. Feldspar alteration by sericite is comparatively weak and feldspars were mostly affected by small scale dissolution at strain caps. Also, epidote grains formed along the mylonitic foliation. These reactions are evidence that fluids were present but that the bulk chemistry of the pegmatites was not largely affected by major fluid-rock interaction. Thus, also the elements needed for the corona formation (Si, Ca, Al, Fe and F) were probably supplied by these metamorphic changes, and a major external source and fluid-flow on a large scale is not necessarily required to explain the breakdown of monazite and xenotime. At least, negligible REE transport is expected to produce the chemical gradients reflected by the distinct apatite and epidote compositions depending on the microstructure (monazite corona, xenotime corona, matrix) as discussed hereafter.

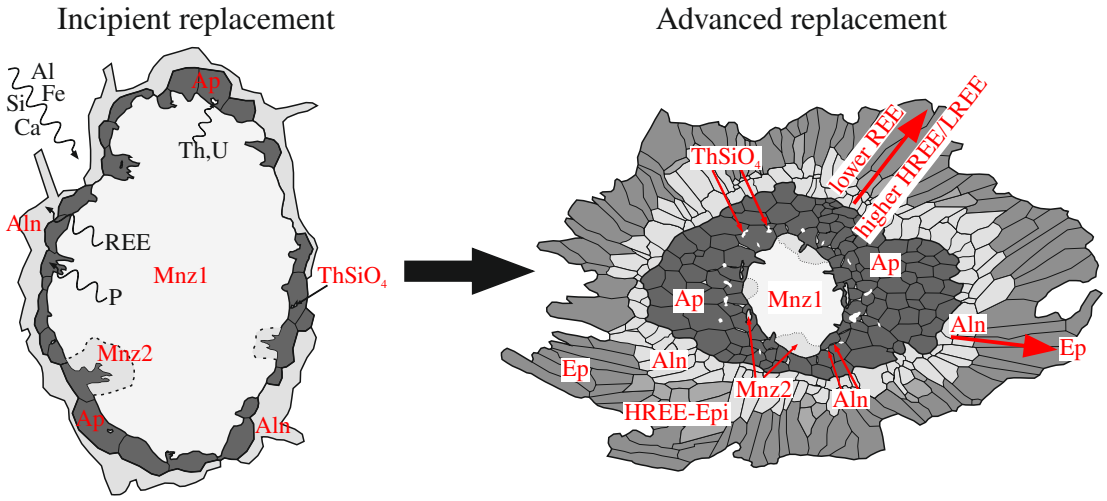

Figure 6.14: Sketch of observed corona microstructures with incipient and advanced replacement of monazite.

6.3.3 Mechanism of corona formation

The general structure of the monazite coronas – an almost pure apatite zone surrounding the monazite core and an outer allanite-epidote zone – can be explained by different nucleation mechanisms. Here it is suggested that monazite was partly dissolved at its surface. The involved fluid was supersaturated with respect to apatite, which precipitated immediately. Because of the weak crystallographic similarity of apatite and monazite – both contain PO_4-tetrahedra – precipitation occurred essentially at the reaction front. Thus, the external shape of the monazite is preserved by a polycrystalline apatite aggregate with a weak correlation to the crystallographic orientation of the replaced monazite (Fig. 6.11). This process of interface-coupled dissolution and precipitation has been well established in the last years (Putnis, 2009; Putnis & Austrheim, 2010) and the same epitactic relationship has been described by Hansen & Harlov (2007). The nucleation of allanite, on the other hand, is not controlled by monazite, given its crystallographic and chemical difference. Allanite therefore precipitates between apatite and the outside of the incipient corona (Fig. 6.14). This explanation of different nucleation environments based on the chemical and structural differences, however, can neither explain the complex elemental zoning in the allanite/epidote zone nor the occurrence of allanite inside the apatite zone in coronas with relative advanced replacement of monazite (Figs. 6.1 d, f; 6.6 b; 6.14). The latter observation might be explained by a growing apatite zone hampering fluid flow away from the corona, leading to a ”premature” precipitation of allanite between already formed apatite grains (Fig. 6.6; 6.14).

The internal zonation of the allanite/epidote zone (Figs. 6.1 b, d, e, f; 6.2 e, f; 6.8 b) is also difficult to explain. It has been suggested that LREE-allanite and HREE-epidote nucleate separately, indicating a miscibility gap between those phases (Finger et al., 1998; Upadhyay & Pruseth, 2012). However, it is not exactly known, if such a miscibility gap exists (Gieré & Sorensen, 2004; Armbruster et al., 2006) and the observations presented here rather suggest full miscibility at the given conditions (Fig. 6.7). As allanite is incorporating preferentially LREE (in contrast to epidote Gieré & Sorensen, 2004) and

the dissolving monazite is containing especially LREE, LREE-allanite is precipitating first (Fig. 6.14). Only at a later stage, accumulated HREE from the dissolved monazite is incorporated into epidote precipitating at the outer rim. Consistently, the HREE-bearing xenotime is only replaced by HREE-apatite and HREE-epidote (Fig. 6.9). Changing HREE/LREE ratios have also been attributed to differential mobility of these elements in the fluid phase (e.g. Finger et al., 1998; Broska et al., 2005; Upadhyay & Pruseth, 2012). Also, differences in solubility can lead to different travel distances (e.g. Förster, 2000), which might have played a role for the observed REE zonation – higher HREE/LREE-ratios towards the outside of the corona around monazite. This would suggest that the HREE have a higher solubility than the LREE in the fluid at the given conditions, which is consistent with the observation that altered monazite has lower HREE/LREE ratios than magmatic one (Figs. 6.3; 6.4). Nonetheless, more data on the solubility of REE in such an environment of reacting and deforming rocks would be needed.

In addition to this radially changing REE composition, grains in the allanite/epidote zone can show oscillatory internal zonations and allanite overgrowths (Fig. 6.8). Oscillatory zonings do not necessarily reflect overall changes in fluid chemistry, but might just be caused by local equilibrium and self-organization (e.g. Wang & Marino, 1992; Borg et al., 2014). REE-rich overgrowths or zones inside grains suggest that dissolution of monazite/xenotime occurred not in a single stage but rather episodic.

In summary, the observed REE gradients in single grains, within the corona and on thin section scale suggests restricted transport through the fluid phase and/or restricted availability of fluid at the given time and temperature-pressure conditions as well as episodic reactions.

6.3.4 Relation between corona formation and mylonitic foliation

The relationship between the corona microstructure and the mylonitic microfabric can be used to infer the relative ages. The first observation is the elongate shape of the coronas itself. The corona structures are flattened within the sample's foliation plane (Figs. 6.1 & 6.2). This elongation is mirroring the shape of the apatite and allanite/epidote zones, which mostly have a lower width perpendicular and a bigger width parallel to the foliation (Fig. 6.2). This elongation can have two reasons: (a) it reflects replaced elongated monazite grains, which where rotated into the rock's foliation during deformation before corona formation; or (b) the apatite and allanite/epidote zones formed at non-isostatic stress conditions during deformation. As the preserved monazite can even be elongate perpendicular to the foliation (Fig. 6.1 f), and commonly a smaller apatite zone perpendicular as parallel to the foliation (Fig. 2d) is observed, indicates that the replacement was enhanced in strain shadows of the monazite. Therefore, case (b) seems most likely. Yet, the outermost epidote zones themselves are mostly not deformed (Fig. 6.2 e, f).

The second observation is that the mylonitic foliation is affected by the corona microstructure (Fig. 6.1 a, c). Especially the corona around monazite situated at a prismatic strain shadow of a tourmaline, i.e. at a quartz-filled vein, indicates that breakdown reactions of monazite to apatite and allanite/epidote took place during formation of the mylonitic microfabric. Consistently, these observations suggest that the main stage of

formation of the coronas and the mylonitic foliation are more or less coeval, though the last growth of epidote took at least locally place at a late stage of deformation at already low stress conditions.

The observations consistently suggest that both deformation and corona formation are episodic process interlinked with each other. The inferred age of the corona formation of 60 ± 10 Ma years therefore is also a time of active deformation in the area. Rb/Sr muscovite cooling ages decrease from 250 to 30 Ma from the DAV towards the north (Borsi et al., 1978), K/Ar muscovite cooling ages typically range between 100 and 60 Ma and Rb/Sr and K/Ar biotite cooling ages between 30 and 15 Ma (e.g. Steenken et al., 2002). This suggests that the mylonitic pegmatites were at the time of deformation and corona formation at lower greenschist-facies conditions, which is well consistent with the overall microfabric of the mylonitic pegmatites. Shear zone activity at greenschist facies conditions and ∼ 60 Ma was also inferred from combined geochronological and microstructural data for the structurally similar Main Mylonite Zone in the Kreuzeck Mountains southeast of the Tauern Window (Wölfler et al., 2015).

6.4 Conclusions

The analysis of the corona structures in mylonitic pegmatites from the Austroalpine basement south of the western Tauern Window with an inner zone of apatite, surrounding relict monazite and xenotime, and an outer zone of allanite/REE-bearing epidote allow to draw the following conclusions:

1. Monazite and xenotime relics are heterogeneous with domains of distinct ages and compositions representing different generations with the same crystallographic orientation, indicating interface-coupled replacement reactions (Fig. 6.14).
2. EMP dating gave 250–287 Ma for the primary domains of both monazite and xenotime, representing the magmatic age of the pegmatites. In secondary monazite, a mean Alpine age of 66 ± 6 Ma was measured. Allanite was dated by LA-ICP-MS U/Th-Pb to an age of 50–60 Ma, which suggest that at least part of the monazite alteration was coeval with the formation of the corona itself.
3. The chemical and structural characteristics of the coronas suggest that monazite and xenotime were dissolved in a fluid phase that provided the elements required for precipitation of apatite, allanite and epidote (Si, Ca, Al, Fe, F). The observed crystallographic relationship between apatite and the replaced monazite/xenotime and the highly irregular phase boundary indicate that apatite directly replaced monazite/xenotime by a dissolution-precipitation processes. The precipitation of allanite/epidote, however, was not controlled by the direct replacement of monazite/xenotime and occurred after transport through the fluid phase outside the apatite zone (Fig. 6.14).
4. The relative amount of apatite and relict monazite is dependent on the local surrounding microfabric (Figs. 6.1; 6.2), indicating that fluid available along grain boundaries in the matrix and cracks controls the progression of replacement.
5. The preserved REE gradients in single allanite/epidote grains, within the corona and on thin section scale suggests restricted transport within the fluid phase and/or

restricted availability of fluid as well as episodic reactions.

6. The oblate shape of the coronas aligned within the samples' foliation and the deflection of the mylonitic foliation by the corona microstructure suggests that the replacement reactions took place during deformation. Thus, the time of corona formation at $\sim$ 60 Ma was a time of metamorphic reactions and deformation of the Austroalpine basement south of the western Tauern Window.

7 Recrystallization of quartz after low-temperature plasticity – The record of stress relaxation below the seismogenic zone

This chapter is based on the manuscript "Trepmann, C.; Hsu, C.; Hentschel, F.; Döbler, K; Schneider, C; Wichmann, V. (2017): Recrystallization of quartz after low-temperature plasticity – The record of stress relaxation below the seismogenic zone. *Journal of Structural Geology*, 95: 77–92, doi: 10.1016/j.jsg.2016.12.004".

7.1 Introduction

Dynamic recrystallization of quartz is known to largely influence the physical properties of crustal rocks (e.g. strength, anisotropy) and the rheology of the upper lithosphere (e.g. Evans & Kohlstedt, 1995; Kohlstedt et al., 1995). Although dynamic recrystallization has been the focus of a vast number of observational, experimental and numerical studies, many details about the development of microstructural anisotropy, especially crystallographic preferred orientation (CPO) and shape preferred orientation (SPO), during recrystallization remain equivocal (Hobbs, 1968; Hirth & Tullis, 1992; Lloyd & Freeman, 1994; Skrotzki, 1994; Piazolo et al., 2002; Passchier & Trouw, 2005; Derez et al., 2014; Kjøll et al., 2015). This uncertainty is especially true for complex stress and strain rate histories. Transient high stress deformation of quartz can be followed by recrystallization at relaxing stresses during the seismic cycle at depths below the seismogenic zone (Trepmann & Stöckhert, 2003, 2013; Trepmann et al., 2007; Bestmann et al., 2012). The resulting microfabrics may be difficult to distinguish from those that develop during dislocation creep with dynamic recrystallization at rather constant stresses (Stipp & Tullis, 2003; Austin & Evans, 2007; Platt & Behr, 2011b,a). Yet, this distinction is important for deciphering and understanding the deformation record of natural shear zones.

In natural shear zones, a complex history of deformation and recrystallization at varying conditions influences the texture (i.e. the crystallographic orientation relationship of grains) of the evolving quartz recrystallization microfabric. It is generally assumed that deformation by dislocation glide can cause a CPO, where crystal orientations rotate towards an orientation that promotes glide on the active glide system(s) (Hobbs, 1968; Schmid & Casey, 1986; Schmid, 1994; Skrotzki, 1994). Which glide system will be active during dislocation glide depends on the critical resolved shear stress (CRSS). More than one glide system can be active, especially at large differential stresses. The CPO resulting from deformation by dislocation glide is dependent on deformation conditions, as temperature, water content, pressure, stress and strain rate (Lister & Hobbs, 1980; Hobbs, 1985; Schmid, 1994; Skrotzki, 1994; Passchier & Trouw, 2005; Law, 2014; Hobbs & Ord, 2015). During ongoing deformation, grains in specific crystallographic orientations may develop a systematically higher dislocation density than others, such that strain-induced grain boundary migration (SIGBM) may lead to a preferred growth of those with the lower dislocation density (Jessel, 1987; Ree, 1990; Gleason & Tullis, 1993), influencing the evolution of a CPO. A CPO, however, may as well develop by dissolution-precipitation creep (Bons & den Brok, 2000) or preferred precipitation from a fluid, where the growth rate of quartz is dependent on crystallographic orientation (e.g. Shelley, 1979,

1989, 1994).

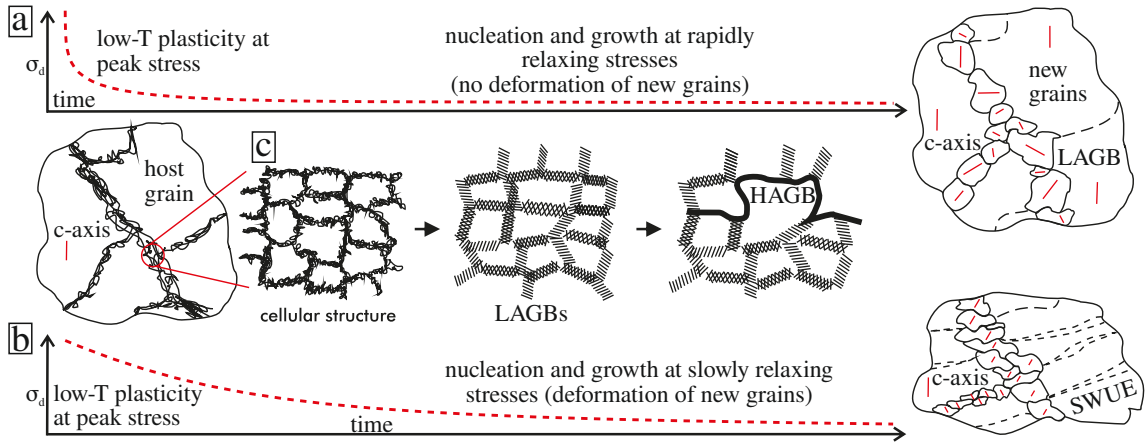

Figure 7.1: Schematic sketch depicting formation of new grains from localized highly-damaged zones after low temperature plasticity at transient peak stresses during **(a)** fast stress relaxation, i.e. nucleation and growth at low stress (below 125 MPa), leading to isometric grains with no CPO, and **(b)** slow stress relaxation, i.e. nucleation growth at moderately high stresses (on the order of a few hundred MPa, see text for discussion) resulting in elongate new grains with SPO and CPO. **(c)** Possible mechanism of "nucleation" from a cellular structure characterized by zones of a high density of tangled dislocations, modified after (Humphreys, 2004, see text for discussion).

To be able to interpret a texture in the context of the deformation conditions and history, the deformation mechanisms as well as the recrystallization processes must be understood. From microstructural observations of deformed metamorphic rocks, it can be difficult to unravel the associated processes during recrystallization, owing to similar microstructures that can be formed by a sequence of different deformation and recrystallization stages. Experiments allow the investigation of microstructural evolution through a sequence of specific stages at different stress conditions. A sequence of high-stress deformation of quartz, followed by deformation at relaxing stresses was performed to simulate deformation during the seismic cycle just below the seismogenic zone in the continental lithosphere by Trepmann et al. (2007) and Trepmann & Stöckhert (2013). The deformation experiments were performed in a Griggs-type deformation apparatus at 400 °C and 2 GPa confining pressure. Maximum differential stresses reached 2–3 GPa during the experiments. The high-stress deformation stage was followed by a stage of creep at low stresses, 900 °C and 2.5 GPa confining pressure. Low-temperature plasticity (i.e. dislocation glide-controlled deformation commonly associated with microcracking due to strain-hardening) of quartz involved the formation of localized highly-damaged zones (Fig. 7.1) characterized by large dislocation densities and microcracks. During creep, two different stress histories were chosen: fast rates of relaxing differential stresses (to $<$ 125 MPa) and slow rates of stress relaxation, where moderate differential stress were kept constant at about 250 MPa. These experiments revealed characteristically different recrystallization microfabrics: creep at low stress after low-temperature plasticity resulted in a random texture of new grains (Fig. 7.1 a); When the subsequent creep-stage was performed at moderately high stresses, in contrast, a marked CPO and SPO developed (Fig. 7.1 b; Trepmann et al., 2007; Trepmann & Stöckhert, 2013). Whereas the high-stress

deformation stage was performed close to the conditions at the base of the seismogenic zone, the creep stage was performed at higher temperatures to accelerate thermally activated dislocation climb and strain-induced grain boundary migration. Whether indeed the same processes are activated at isothermal conditions in nature can only be evaluated by a comparison to natural microstructures. For this comparison, quartz microfabrics analyzed by polarized light microscopy, scanning electron microscopy (SEM) and transmission electron microscopy (TEM) are presented from two selected shear zones in the Eastern Alps: the Defereggen-Antholz-Vals (DAV) shear zone and the basal thrust of the Silvretta nappe (Fig. 3.3). The deformation mechanisms and formation of new grains recorded by characteristically different recrystallization microfabrics of the two shear zones are analyzed to obtain information about their stress histories. Finally, the geological implications of the different recorded stress histories are discussed.

7.2 Sample selection

For this study, the Silvretta basal thrust at the southwestern border of the Engadine window (Jamtal, Austria) and the DAV shear zone to the south of the western Tauern Window (Southern Tyrol, Italy) in the Eastern Alps (Fig. 2) were chosen, because: (1) The associated fault rocks were deformed at lower greenschist facies conditions (DAV: e.g. Kleinschrodt, 1987; Stöckhert et al., 1999; Silvretta: e.g. Masch & Koch, 1992). These conditions correspond to the base of the seismogenic zone in the continental lithosphere (e.g. Scholz, 2002) as well as to the so-called brittle-viscous transition of quartz, depending on the stress-loading rates (e.g. Voll, 1976; Hirth & Tullis, 1994; Stöckhert et al., 1999; Hirth et al., 2001). Just below the base of the seismogenic zone, systematically varying stresses during the seismic cycle can be expected to leave a marked imprint in the quartz microfabrics of the deformed rocks (Trepmann & Stöckhert, 2003, 2013; Trepmann et al., 2007). (2) Both, the thrust and the shear zone contain pseudotachylytes indicating seismic activity during their development (DAV: e.g. Mancktelow et al., 2001; Silvretta: e.g. Masch & Koch, 1992). (3) Given the generally different tectonic settings for the thrust and the shear zone, different deformation histories are expected, which should produce distinctive microfabrics. Gneisses near both the thrust and the shear zone that contain concordant quartz veins were sampled, so as (1), to rule out systematic differences in the quartz microfabric due to differing mineralogical composition; and (2) for better comparison to the experimental results on deformed natural vein quartz. It is important to recognize that these veins predate the thrust and the shear zone, so their microfabrics can be used to represent deformation during the formation of these larger structures and to compare the two deformation records to the perspectives gained from the experimental deformation of quartz.

Pseudotachylyte-bearing gneisses with quartz veins from the Silvretta crystalline nappe were collected close the basal thrust exposed at the south-western border to the Engadine window, North to the Jamtal glacier (Austria), close to the Russkopf (Fig. 2a,b, CS24, CT623, CT626, N46°52'19.13"; E10°9'55.29").

Samples were collected along the Defereggen-Antholz-Vals (DAV) shear zone at the Sambock crest (KD81, 84, 85, 86; N46°51'08", E11°53'28") and the Terenten Valley (KD1–3; N46°50'15.72", E11°46'32.45") located south to the western Tauern window (Fig. 2a, c),

Southern Tyrol, Italy.

7.3 Quartz microfabrics

7.3.1 Silvretta fault rocks

The microfabric of vein quartz fault rocks (Fig. 7.2 a) is characterized by fine-grained (< 10 mm in diameter) quartz aggregates that cut by branching zones at an angle of 20–40° to the normal of the foliation through coarse original grains (several mm in diameter), termed host grains (Fig. 7.2 b–f). Lamellar undulating domains with slightly different extinction position, described as short wavelength undulatory extinction (SWUE) by Trepmann & Stöckhert (2013) are typical microstructures within host grains (Fig. 7.2 d). Narrow (10–20 mm) domains comprising new grains can occur in conjugate sets (Fig. 7.2 e & f). EBSD-analyzes reveal that the new grains have diameters mostly < 10 mm, with an average of about 6 mm (Fig. 7.3). The new grains do show a weak SPO, with long axes of grains oriented at a high angle to the foliation-normal and a small aspect ratio of in average 1.6 (Fig. 7.3 e & f). The orientations of new grains broadly cluster around that of the host crystal, and they do not reveal a marked CPO (Figs. 7.3 c & d; 7.4 b & c). Misorientation-angle distributions of neighbouring new grains show an abundance of small misorientation angles and a deficit at large misorientation angles when compared to a random distribution, whereas the randomly selected grains reveal misorientation angles very close to a random distribution (Fig. 7.3 g). New grain orientations have strongly varying Schmid factors for basal <a> glide (Figs. 7.3 b & 7.4 e), the dominant glide system of quartz at greenschist facies conditions (e.g. Hobbs, 1985; Schmid & Casey, 1986; Law, 2014). No systematic variation of the Schmid factor for new grains was found for any glide system. The misorientation angle associated with SWUE is generally 2–4°, whereas the jump in misorientation angle in the host grain to the recrystallized grains is 40–90°, which is large and abrupt (Fig. 7.4 d, f, g). Dauphiné twin boundaries are common in host grains (Fig. 7.4 a & b). Note for example the SW-NE trending Dauphiné twin boundary in Fig. 7.4 a, separating two coarse twin domains (yellow and purple coloured), that is at high angle to the zone of localized new grains.

TEM investigations reveal recrystallized grains with a diameter of typically 1–2 mm (Fig. 7.5 a & b). Commonly grains are partly bound by high-angle grain boundaries (HAGBs) and partly by low angle grain boundaries (LAGBs) (Fig. 7.5 c–e) with the LAGB connecting HAGBs (Fig. 7.5 e). Generally, many tilt boundaries (Fig. 7.5 f–h) and few twist boundaries (Fig. 7.5 i) are observed. The dislocation density is heterogeneous, with the range of 10^{12}–10^{13} m^{-2} in the deformed host crystal moderately high (Fig. 7.5), typical for quartz that shows optically marked undulatory extinction (Fig. 7.2 d). In contrast, new grains show only a low density of dislocations (Fig. 7.5 b–e). These observations clearly rule out purely cataclastic formation, where the new grains would represent fragments of the hosts. Remarkably, fluid inclusions were not observed in TEM, which are otherwise typical for natural vein quartz. Together with the large number of observed crystal defects, the missing fluid inclusions rule out formation of new grains by precipitation from a fluid as important.

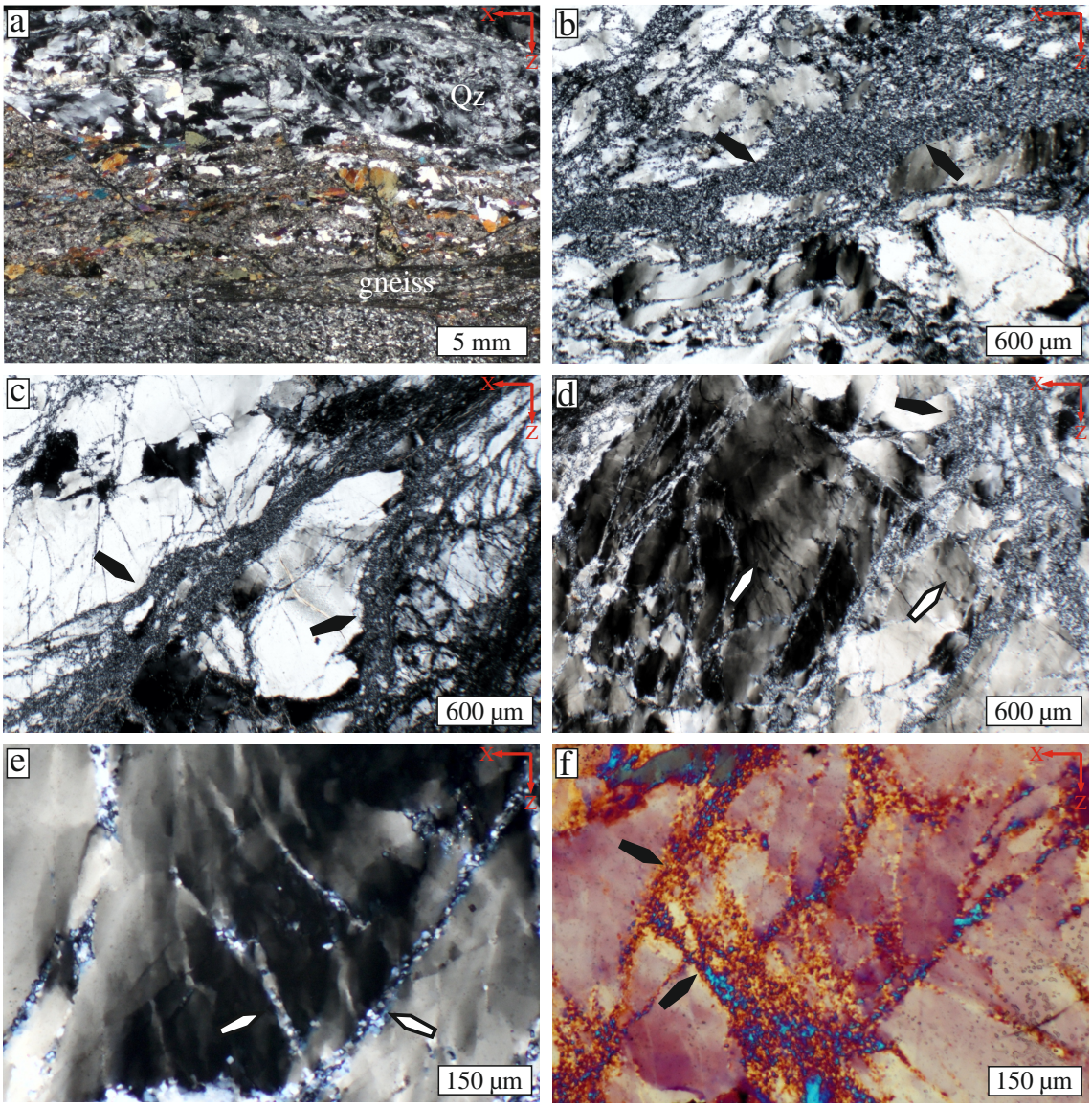

Figure 7.2: Cross-polarized photomicrographs showing zones of recrystallized quartz from Silvretta fault rocks (CT 626). **(a)** Overview of quartz vein (qtz) within amphibole-gneiss. **(b–d)** Branching zones of recrystallized quartz grains (black arrows) cutting through deformed host crystals showing short-wavelength undulatory extinction (SWUE, white arrows in d). **(e, f)** New grains along conjugate zones (arrows) cutting through host crystal; (f) compensator plate inserted and is same view as (e).

7.3.2 DAV shear zone

Vein quartz samples from the DAV shear zone show heterogeneous quartz microstructures (Fig. 7.6 a) with large deformed host grains surrounded or cut by localized zones of recrystallized grains (Fig. 7.6 a–d). The large host grains show SWUE, along which new grains can occur (Fig. 7.6 e–f). Deformation lamellae parallel to the basal plane are common (Fig. 7.7). Recrystallized grains can occur in micro-shear zones in conjugate orientations cutting through the host grains at an angle of 50–60° to the normal of the foliation, z (Fig. 7.6 b–c). The *c*-axis orientations of grains in the conjugate strings

systematically differ from axial orientations in the host grains, as shown by polarized light microscopy using the compensator plate (Figs. 7.6 c & 7.8 a). This difference would correspond to a relative rotation of the c-axes of grains in the microshear zones, corresponding to their respective sense of shear, assuming a shortening direction perpendicular to the foliation of the sample (Fig. 7.8 b, e, f). EBSD-analyzes show that the new grains occur at orientations with a high Schmid factor for basal <a> glide (average 0.45; Fig. 7.8 c). Dauphiné twin boundaries in host grains are common close to micro-shear

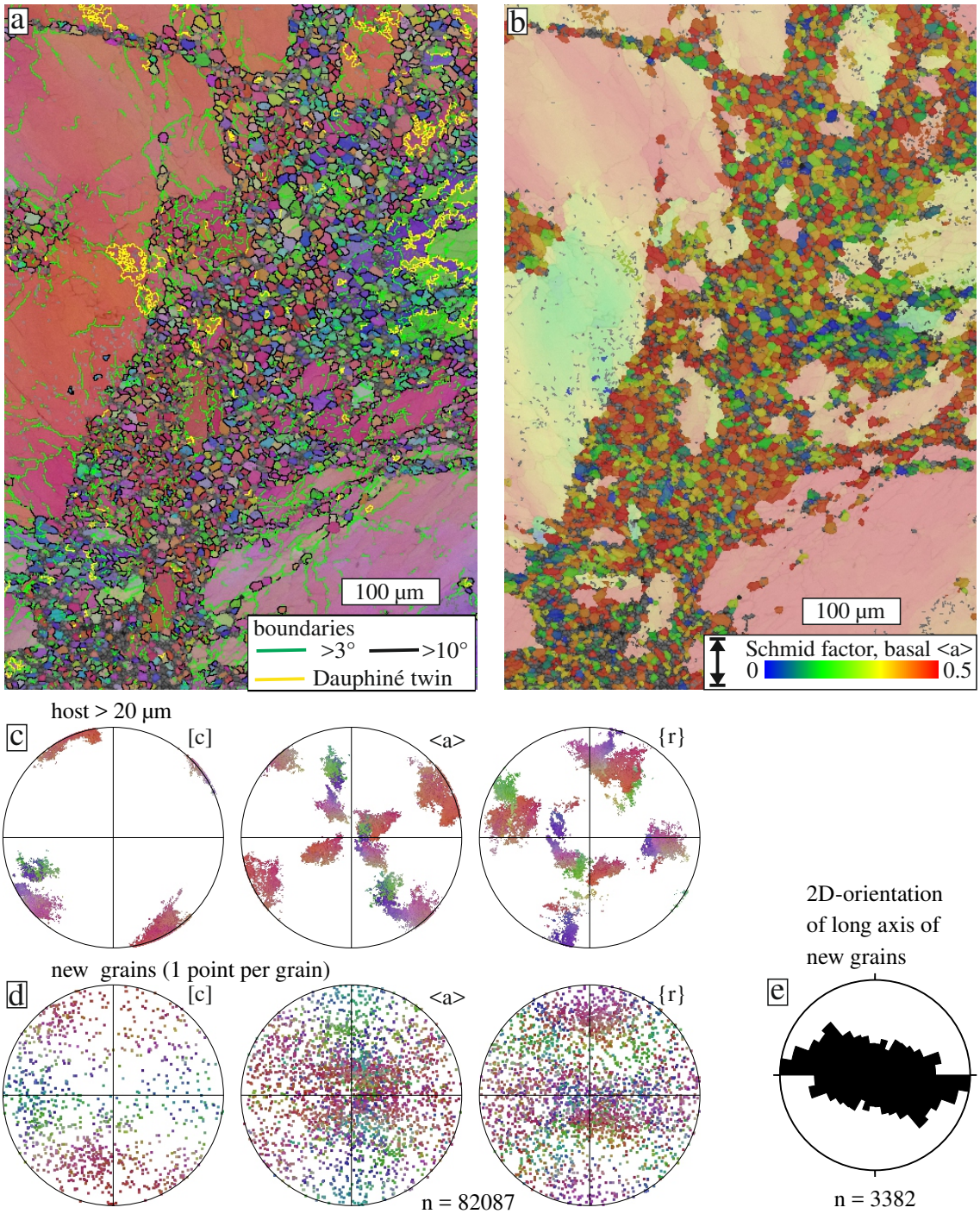

Figure 7.3: continued on the next page

cont.

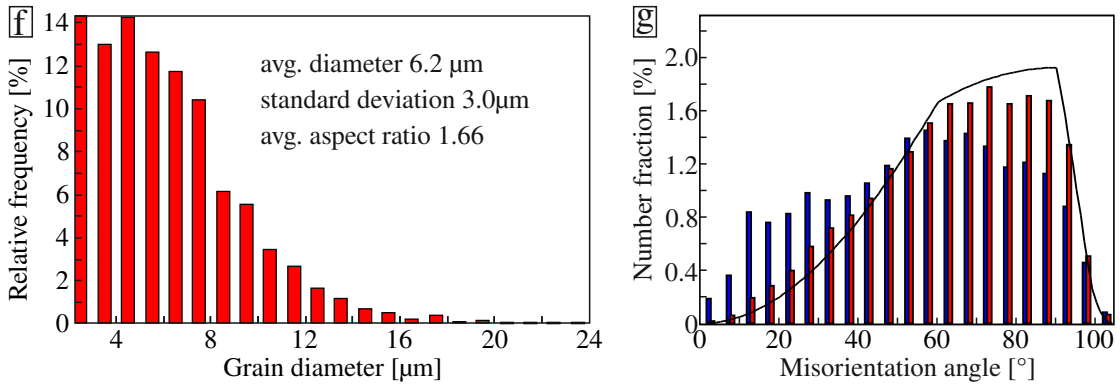

Figure 7.3: EBSD data of recrystallized quartz zone, sample CT626 from the Silvretta thrust. **(a, b)** EBSD map showing colour coding after inverse pole figure (vertical direction) and Schmid factor for basal <a> glide (shortening direction vertical), respectively. In (a) HAGB (black lines), LAGBs (green lines) and Dauphiné twin boundaries (yellow lines) are shown. **(c, d)** Stereographic projection of *c*-, *a*-axes and *r*-planes of host grain and new grains, respectively (colour coding corresponds to map in (a)). **(e)** 2-D orientation of long axis of new grains (10° classes). **(f)** Grain-size histogram for new grains. **(g)** Misorientation-angle distribution of randomly selected (red) and neighbouring (blue) new grains. Theoretic random distribution is shown by black solid line (Wheeler et al., 2001).

zones (Fig. 7.8 b, d). Generally, about 25–30 % of the quartz is recrystallized (< 20 mm in grain diameter), and about 50–70 % of this fraction has a grain diameter smaller than 10 mm (Fig. 7.9). The misorientation profiles show a gradual increase in misorientation angle within the host grain towards strings of recrystallized grains (Fig. 7.9 a–c). The misorientation angle distribution of new grains reveals (for both, randomly selected and neighbouring grains) an excess of orientations with low misorientation angles and deficit of orientation at high misorientation angles compared to a random distribution (Fig. 7.9 d). New grains have an average aspect ratio 1.6 and 1.9, for grains < 10 mm diameter and 10–20 mm, respectively (Fig. 7.9 e). The elongate grains show a marked SPO with the long axes of grains at a low angle to the foliation plane (Fig. 7.9 f) that is also prominent in the polarized light microscope (Fig. 7.6 d). Orientations of host grains with an ellipsoidal shape (aspect ratio around 2) are characterized by a relatively low Schmid factor (in average 0.3; Figs. 7.6 b & 7.8 c). If host grain orientations show a higher Schmid factor, they are rather ribbon shaped with a large aspect ratio averaging around 3 and contain a high amount of subgrains.

In TEM, the new grains in micro-shear zones have a diameter of a few mm and moderately high dislocation densities (Fig. 7.10). The smoothly curved to straight grain-boundaries are commonly decorated by fluid inclusions (Fig. 7.10 a–c, e, arrows). Grain boundaries frequently enclose an equilibrium angle close to 120° at triple junctions (Fig. 7.7 d, arrows). Straight HAGBs decorated with fluid inclusions (Fig. 7.10 e, white arrow) are interpreted as healed microcracks. Low-angle grain boundaries appear to be curved and are not decorated by fluid inclusions. Dislocation-poor domains can be bound by LAGBs (Fig. 7.10 f, arrow). The dislocation density is heterogeneous ranging mostly from 10^{12}–10^{13} m^{-2}.

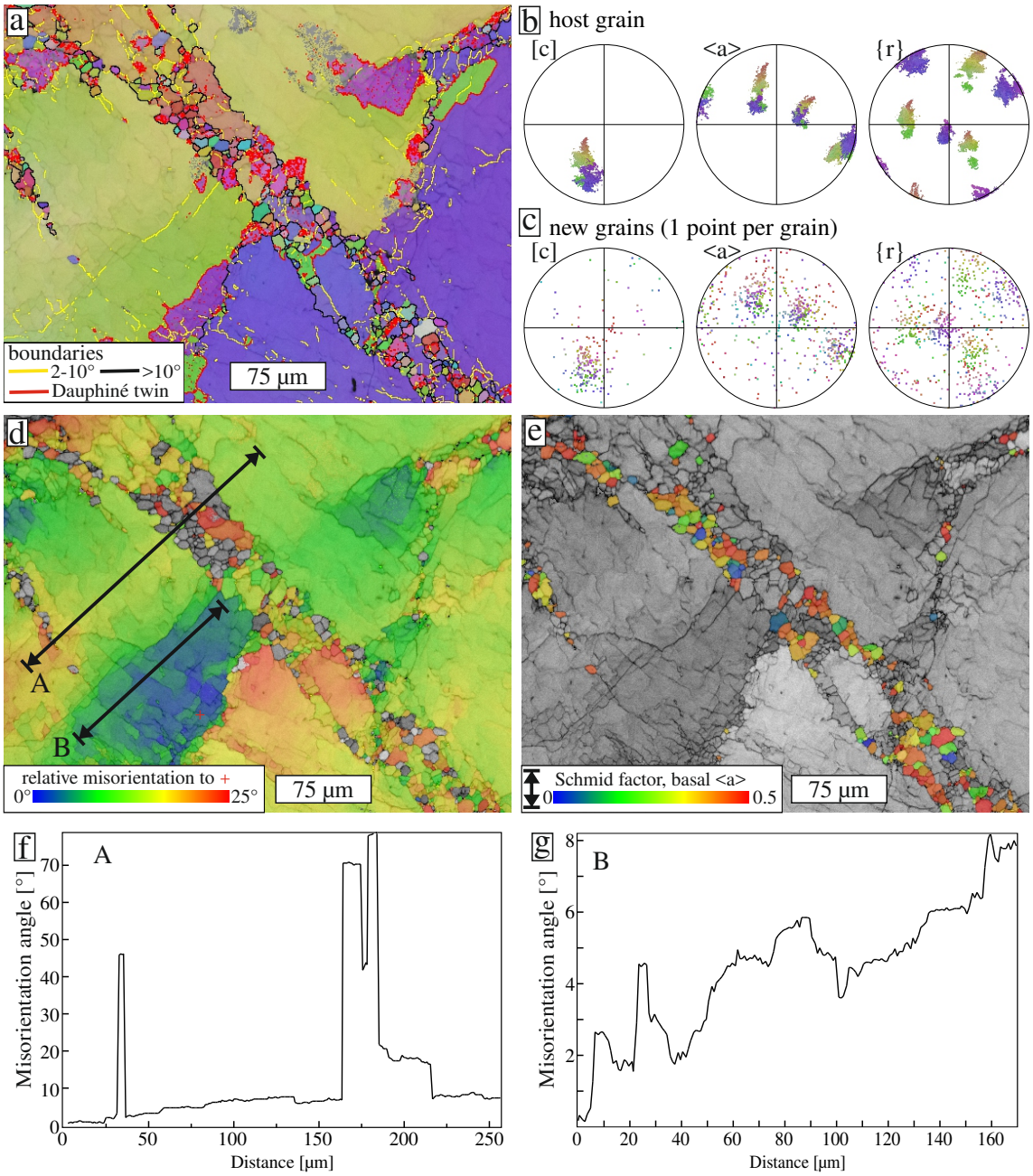

Figure 7.4: EBSD data of recrystallized quartz, sample CT623 from the Silvretta thrust. **(a)** EBSD map showing colour coding after inverse pole figure (normal to thin section). HAGB (black lines), LAGBs (yellow lines) and Dauphiné twin boundaries (red lines) are shown. Note the dominant SW-NE trending Dauphiné twin boundary in the map, separating coarse twin domains (yellow/purple). The short-wavelength Dauphiné twin boundaries are probably artefacts due to the pseudo-hexagonal symmetry of quartz. **(b, c)** Stereographic projection of *c*-, *a*-axes and poles to *r*-planes of host and new grains, respectively, colour coding corresponds to map in (a). **(d, e)** EBSD map showing the relative misorientation (to reference point marked by a red cross) and Schmid factor for basal <a> glide (shortening direction vertical), respectively. In (d), lines correspond to misorientation profiles in (f) and (g). **(f, g)** Misorientation angle profiles, profile lines are shown in map (d).

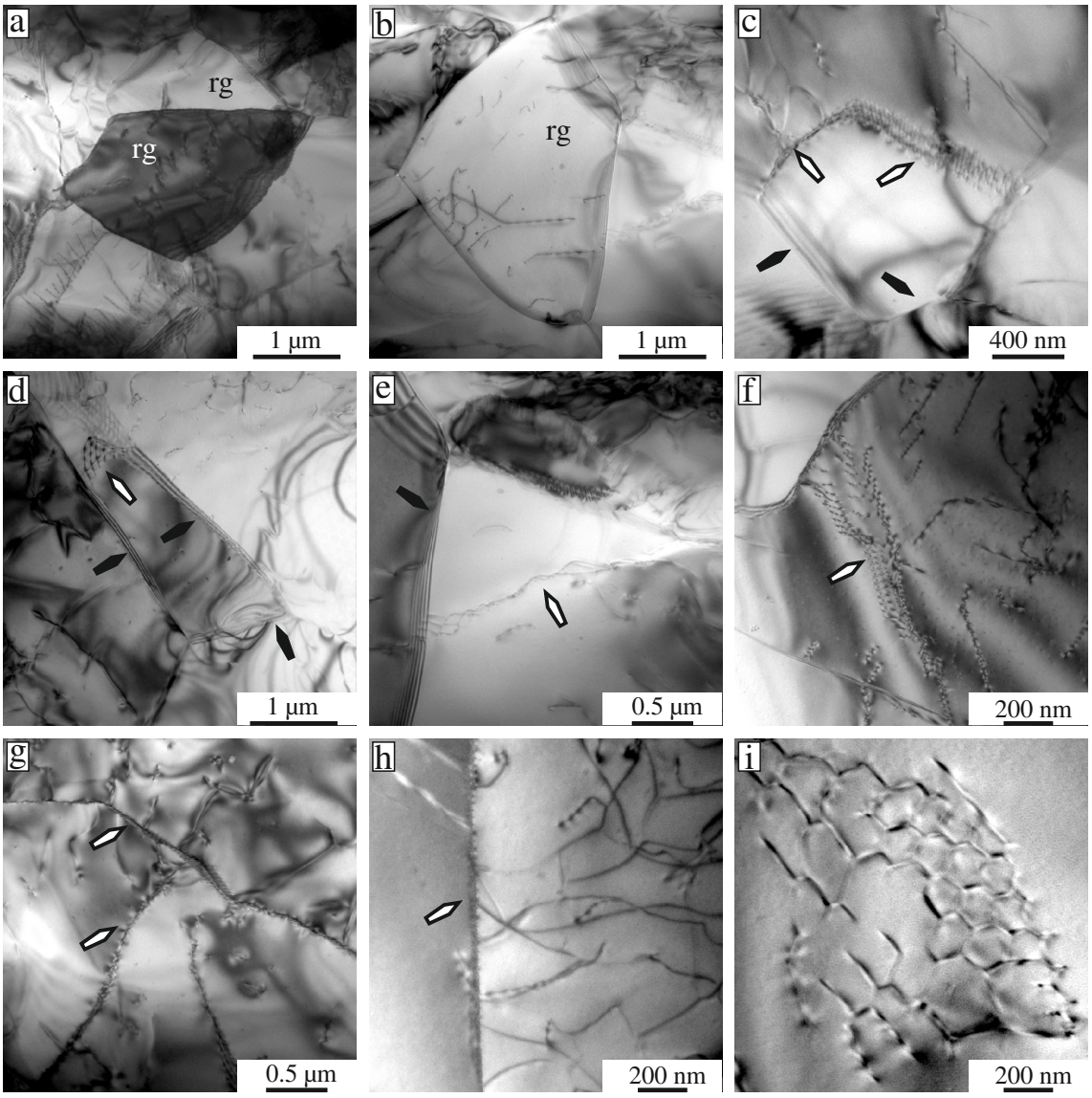

Figure 7.5: Bright field TEM micrographs of new grains in quartz recrystallized zones from Silvretta fault rocks (CT 626, CS24). **(a, b)** Recrystallized grains (rg). **(c–e)** Grains partly bound by HAGBs (black arrows) and LAGBs (white arrows). **(f–h)** Tilt boundaries, as indicated by closely arranged dislocations (white arrows) and (i) twist boundary, indicated by network of *a*-dislocations in the basal plane.

7.4 Discussion

7.4.1 Nucleation and growth

The quartz microfabrics, record recrystallization involving the formation of "new grains" in the sense of grain-size reduction from original coarse grains (Fig. 7.1). The observations of many crystal defects and LAGBs for all observed microstructures, clearly rule out purely cataclastic deformation, but suggest a strong role for crystal-plastic deformation. The formation of new grains from a crystal-plastically deformed microstructure requires the formation of a volume of relative strain-free crystalline material, which is

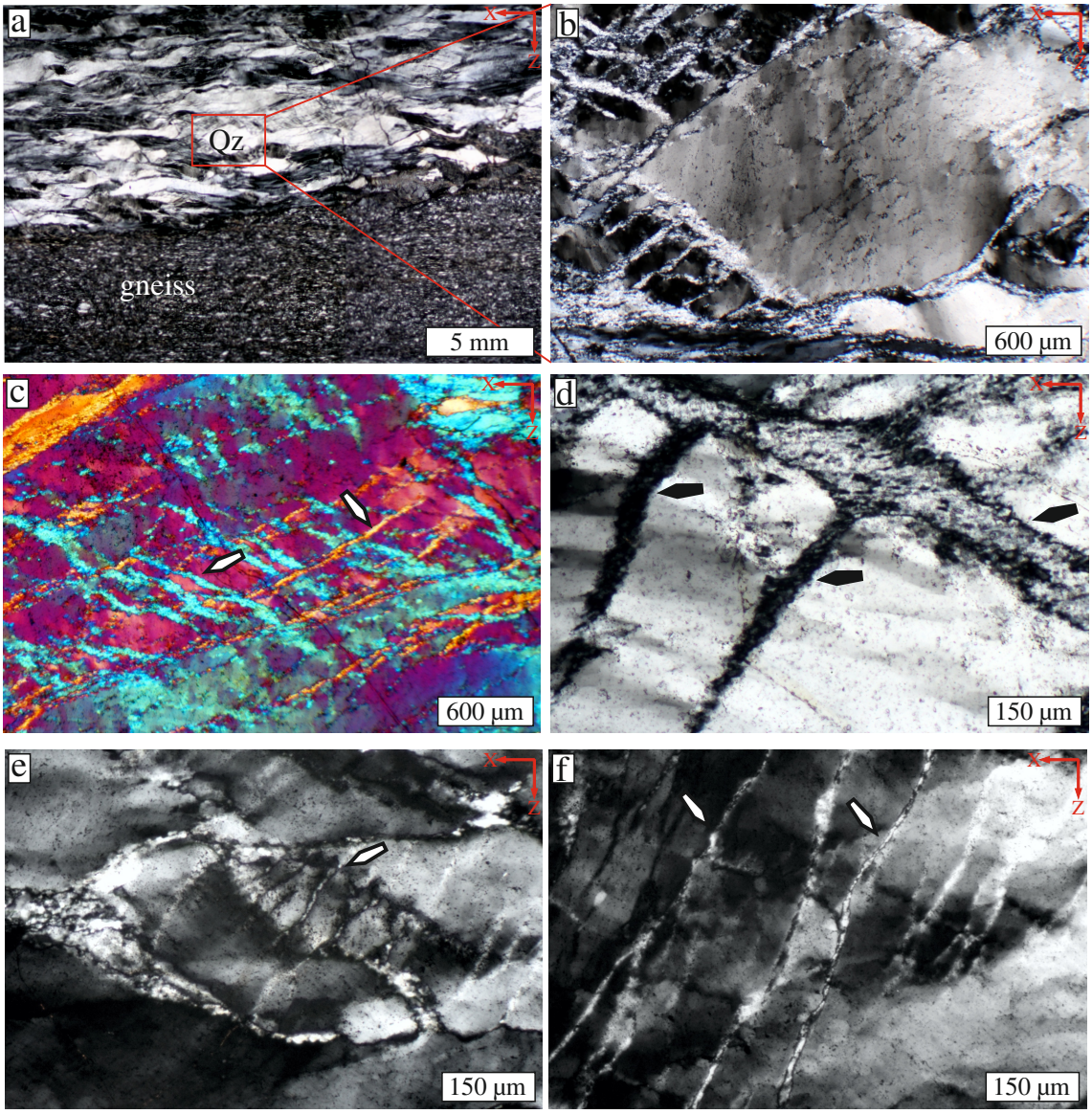

Figure 7.6: Cross-polarized photomicrographs of recrystallized quartz zones in samples from DAV shear zone. **(a)** Overview of quartz vein (qtz) within paragneiss. **(b, c)** Micro-shear zones (KD 86) with recrystallized aggregates in conjugate sets. Note in (c) with the compensator plate inserted, the systematic differences in *c*-axis orientation (arrows) indicated by different compensation colours. **(d)** Note the elongate shape and SPO of new grains in the micro-shear zone (arrow, sample KD 84). **(e, f)** New grains along SWUE (arrows, sample KD 81).

sufficiently large to be able to grow by SIGBM into the deformed material (Humphreys & Hatherly, 2004). Whereas the time and length scales during growth by SIGBM allow experimental studies, microscopy and other techniques, the study on the "nucleation" process is not straightforward and remains poorly understood (Humphreys, 2004). The term "bulging recrystallization" is commonly used to explain the formation of new grains from migrating pre-existing grain boundaries in combination with fracturing and/or sub-grain rotation (e.g. Stipp & Kunze, 2008). This process, however, cannot explain the

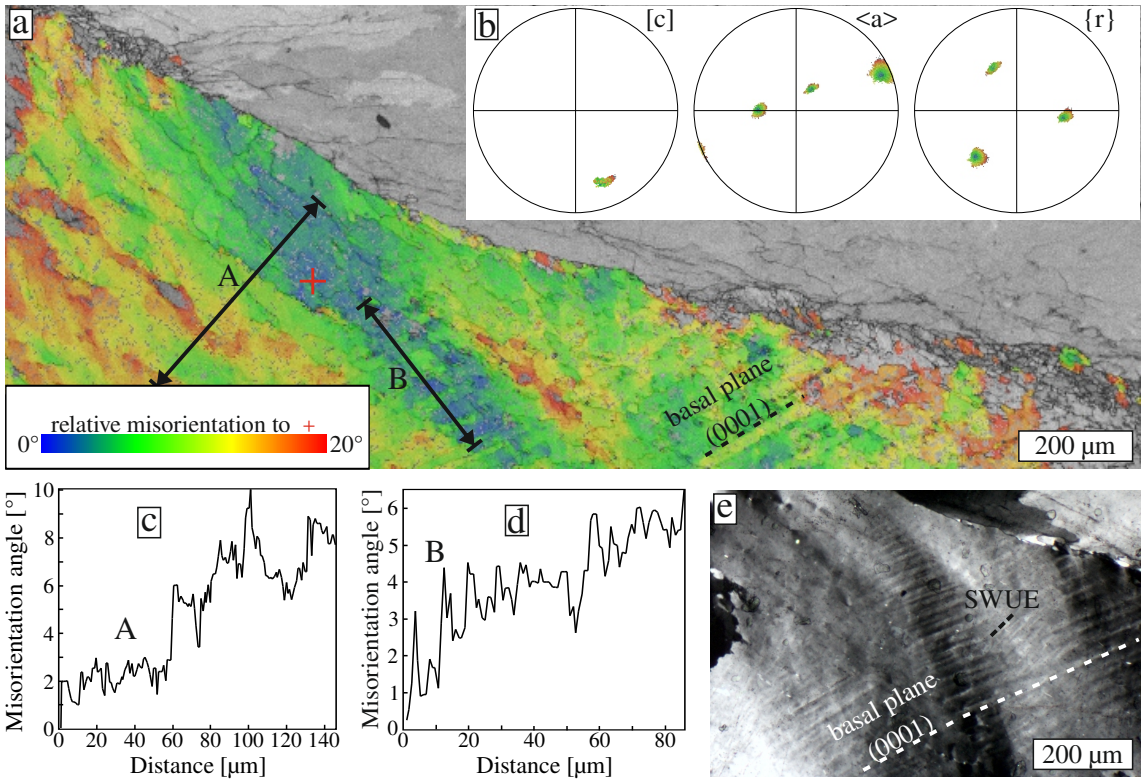

Figure 7.7: EBSD data of subbasal deformation lamellae and SWUE in sample KD1-3 from the DAV shear zone. **(a)** EBSD map showing the relative misorientation to reference point marked by a red cross. **(b)** Stereographic projection of *c*-, *a*-axes and poles to *r*-planes of deformed quartz with colour-coding matching Fig. 8a. **(c, d)** Misorientation angle profiles, profile lines are shown in map (a). **(e)** Crossed-polarized photomicrograph showing SWUE (black dashed line) and deformation lamellae parallel to the basal plane of quartz (white dashed line).

occurrence of zones of fine-grained recrystallized aggregates cutting through large original grains independent of pre-existing grain boundaries (Figs. 7.2; 7.4 & 7.6). In materials sciences, migration of LAGBs and subgrain rotation during dynamic recovery are important processes that create new HAGBs within deformed material, forming a nucleus that eventually grow by SIGBM (Fig. 7.1 c; Humphreys, 2004; Humphreys & Hatherly, 2004). Evidence of subgrain rotation recrystallization, where the orientation of new grains is observed to be close to the orientation of the original host grains, has also been reported for quartz (Hobbs, 1968; Lloyd & Freeman, 1994; Trepmann & Stöckhert, 2009). Hobbs (1968) showed in experiments that new grains formed from a deformed microstructure by subgrain rotation can have a misorientation angle in the range of 20–40°. In the microfabrics described here, subgrain rotation and LAGB migration clearly play an important role for the development of new grains in both shear zones. This interpretation is especially true for quartz from the Silvretta fault rocks, as indicated by the TEM images of grains partly bound by LAGBs and HAGBs, and the general common occurrence of LAGBS (Fig. 7.5 c–i). Yet, the textural differences of the large misorientation angles of new grains (> 40°) and almost random texture of the quartz microfabrics of the Silvretta fault rocks (Figs. 7.3 & 7.4), do not favor an interpretation

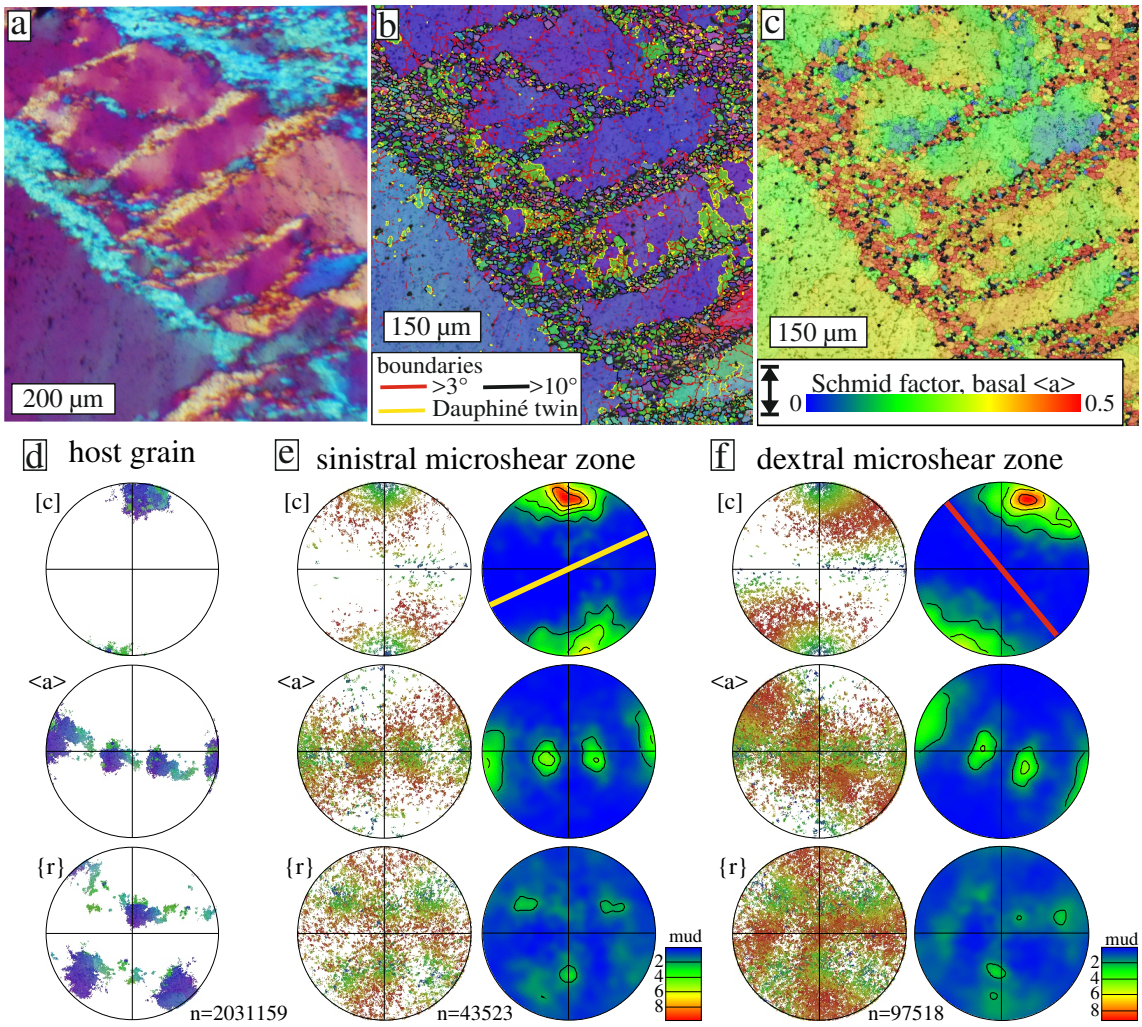

Figure 7.8: EBSD data for recrystallized quartz from DAV shear zone (KD 86). **(a)** Cross-polarized photomicrograph with compensator plate inserted. **(b, c)** Corresponding EBSD maps with colour coding after the inverse pole figure (normal to thin section) and Schmid factor for basal <a> glide (shortening direction vertical), respectively. In (b) HAGB (black lines), LAGBs (red lines) and Dauphiné twin boundaries (yellow lines) are shown. **(d)** Polefigure of *c*-, *a*-axes and poles to *r*-planes of host grain orientation (colour coded after map in b). **(e, f)** Polefigures (colour coded after map in c) and density plots of *c*-, *a*-axes and poles to *r*-planes of dextral (red line) and sinistral (yellow line) micro-shear zones, respectively.

for deformation behavior involving subgrain rotation and LAGB migration alone.

7.4.2 Recrystallization with random texture of new grains (Silvretta fault rocks)

The occurrence of recrystallized grains with orientations not observed in the host grains remains equivocal (Humphreys, 2004), though commonly observed in geomaterials (e.g. Wheeler et al., 2004; Trepmann et al., 2007, 2010; Bestmann et al., 2012). Several possible influences exist:

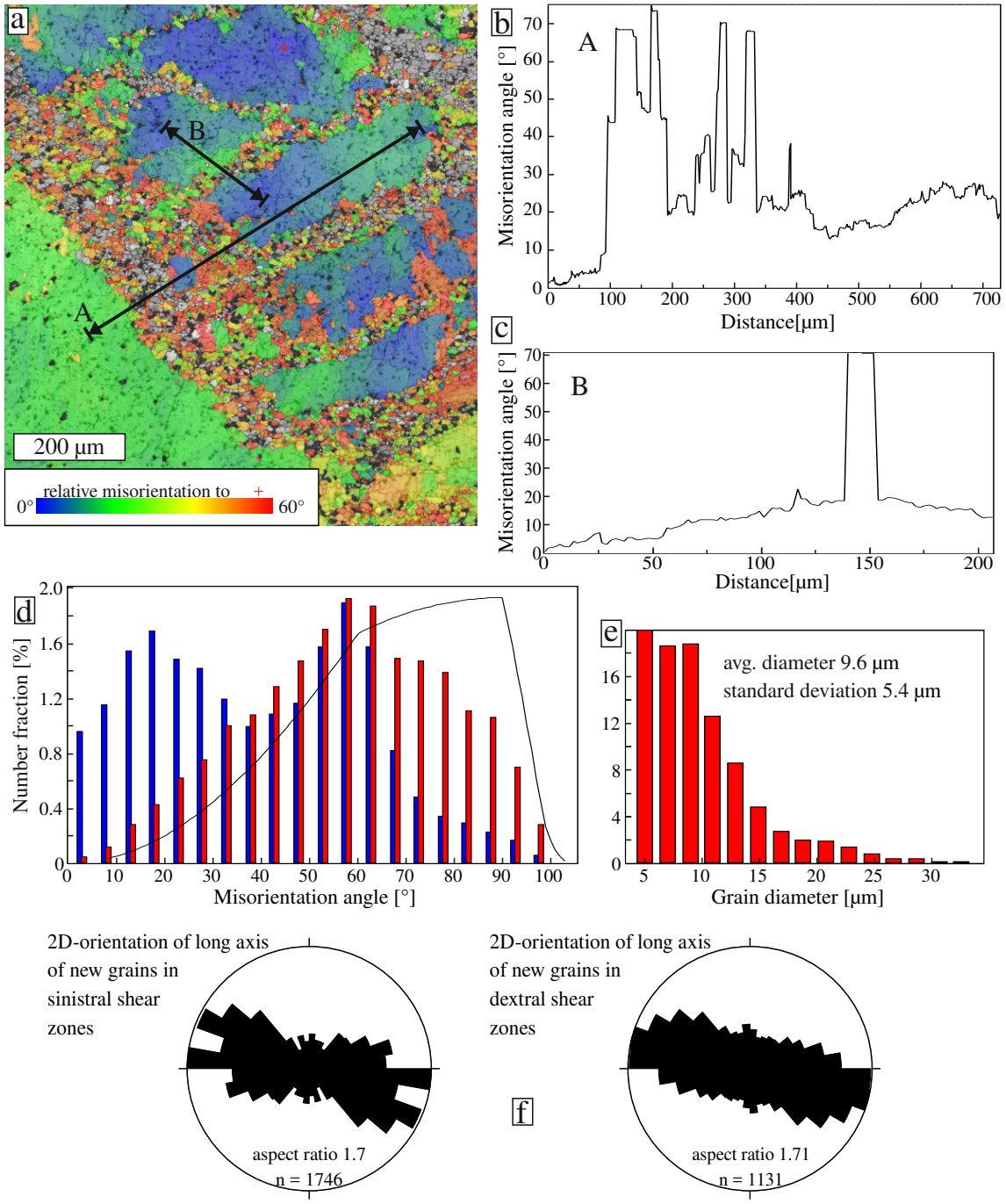

Figure 7.9: EBSD data from map shown in Fig. 9 (KD 86). **(a)** EBSD map showing relative misorientation (up to 60° to reference point marked by a red cross). Lines correspond to misorientation profiles in (b, c). **(b, c)** Misorientation angle profiles, profile lines are shown in map (a). **(d)** Misorientation angle distribution of randomly selected (red) and neighbouring (blue) new grains. Theoretic random distribution is shown by black solid line (Wheeler et al., 2001). **(e)** Grain-size histogram for new grains. **(f)** 2-D orientation of long axis of new grains (10° classes) for new grains in sinistral and dextral shear zones, respectively.

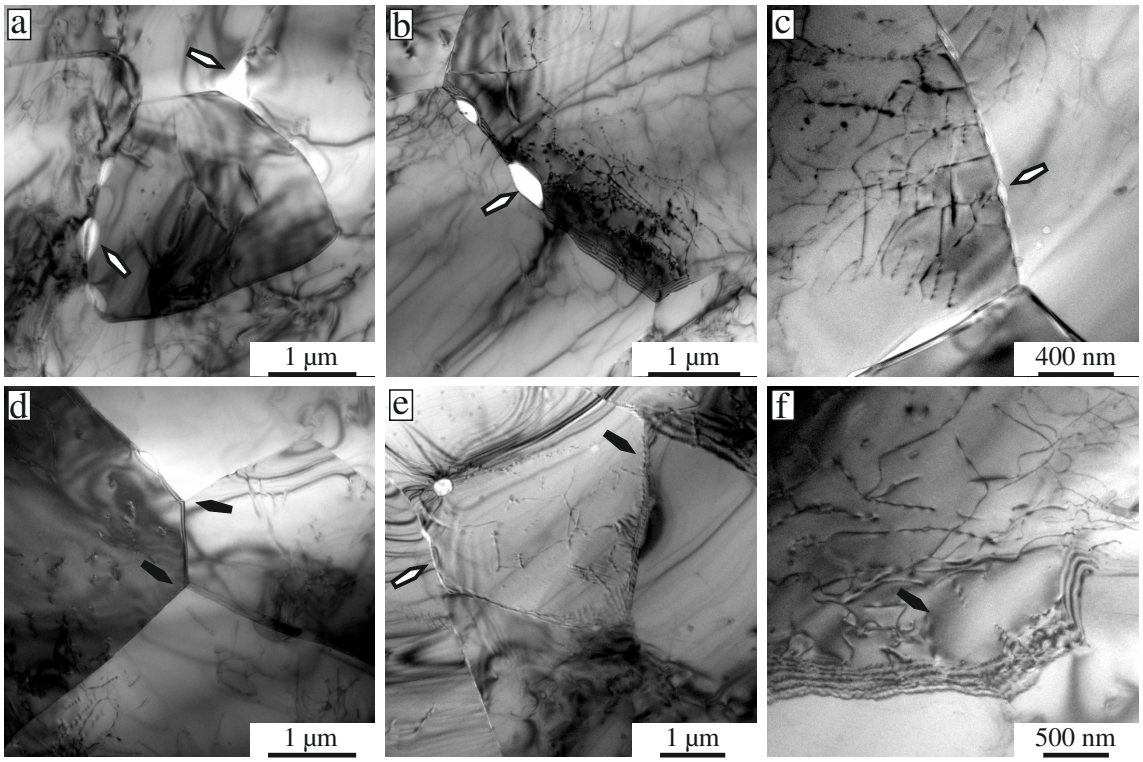

Figure 7.10: Bright field TEM micrographs of quartz micro-shear zones from the DAV samples KD 85, KD 86. **(a)** Recrystallized grain with fluid inclusions along grain boundaries (arrows). **(b, c)** Smoothly curved HAGBs decorated by fluid inclusions (arrows). Moderately high dislocation densities. **(d)** Equilibrium angles enclosed by HAGBs, where three grains meet (arrows). **(e)** Grain partly surrounded by HAGBs decorated with fluid inclusions (white arrow) and LAGBs (black arrow). The straight HAGB decorated with fluid inclusions (white arrow) is interpreted as healed microcrack. **(f)** Dislocation-poor domain surrounded by domain of high dislocation density and LAGBs (black arrow).

Twin boundaries (Humphreys & Hatherly, 2004) and especially Dauphiné twin boundaries can be modified during recrystallization of quartz, resulting in HAGBs with large misorientation angles (Lloyd & Freeman, 1994; Stipp & Kunze, 2008; Pennacchioni et al., 2010). Dauphiné twins are common in natural vein quartz and characterized by misorientation angles of 60° to the host orientation with the *c*-axis being the rotation axis. Dauphiné twin boundaries are common in host grains for both sampled shear zones (Figs. 7.4; 7.8 b, d). Dauphiné twin boundaries can become general HAGBs by dislocation glide and subgrain rotation during dynamic recrystallization, transforming a twin into a recrystallized grain (Lloyd & Freeman, 1994). Indeed, it is inferred here that the large misorientation angles of new grains in misorientation profiles with an abrupt jump (Fig. 7.4 f) result from the influence of Dauphiné twin boundaries. However, large misorientation angles for new grains relative to the host are also commonly unrelated to the Dauphiné twin orientation of the host (Fig. 7.4 a, c). Thus, an influence of Dauphiné twins in the deformed microstructure for the development of new grains is probable but cannot explain the localized, branching aggregates of new grains with almost random texture in deformed host grains of the Silvretta fault rocks alone.

Grain-boundary sliding (Stipp & Kunze, 2008; Bestmann et al., 2012) can destroy initial

present CPO generated by dislocation glide. This process is unlikely here, because neither a shear offset or any other movement along the branching zones of recrystallized grains, nor evidence for a pre-existing CPO is observed. Random texture can form due to initial cataclastic deformation with rigid body rotation of fragments and healing by dissolution-precipitation processes (Vernooij et al., 2006; Bestmann et al., 2012; Kjøll et al., 2015; Goncalves et al., 2016). Evidence for the latter includes microcavities and fluid inclusions along grain boundaries, which are remarkably absent in the quartz samples from the Silvretta fault rocks, as indicated by polarized light microscopy, SEM and TEM (Figs. 7.2–7.5).

Growth of new grains with random texture at low stresses from highly damaged zones generated by low-temperature plasticity at high stress (Fig. 1a) are shown experimentally to form (Trepmann et al., 2007; Trepmann & Stöckhert, 2013). In the deformation experiments from (Trepmann et al., 2007, , their Figs. 7.2 & 7.3) zones with tiny (much smaller in diameter than 1 mm) microlites at random orientations and strongly distorted crystalline structure were observed by TEM after low-temperature plasticity. Also, cellular structures characterized by strain-free domains within crystalline area of high defect density (Fig. 7.1 c) are observed (see Fig. 4 within Trepmann & Stöckhert, 2013). During creep at low stresses, along such zones new grains at random crystallographic orientations (Fig. 7.1 a) grew (Trepmann et al., 2007; Trepmann & Stöckhert, 2013). The microfabric of branching zones of small recrystallized grains cutting through deformed host grains in the samples (Figs. 7.2–7.6), compares very well to these experimental observations for fast rates of stress relaxation, i.e. low stresses during creep (Figs. 5–6 in Trepmann et al., 2007; Figs. 5–7 in Trepmann & Stöckhert, 2013). This characteristic microfabric of fine-grained recrystallized aggregates without marked SPO and CPO, but weak host control, cutting through deformed host grains is thus interpreted to have developed by a sequence of high stress crystal-plasticity and subsequent recrystallization at low stress (Fig. 7.1 a). Stresses and strain rates were initially too great to allow for effective dislocation climb, so localized high-strain zones developed by low-temperature plasticity with some microcracking due to strain hardening. These high-strain zones represent nucleation sites for new grains after stresses relaxed. The new grains grew by SIGBM driven by the reduction in strain energy from dislocation-poor crystalline volumes surrounded by a highly damaged crystalline structure with high defect density. Subgrain rotation and possibly migration of LAGBs create new high-angle grain boundaries, which eventually migrate by SIGBM to from new grains (Fig. 7.1 c). The dependence of the activation energy for grain-boundary migration on misorientation angle might explain the relative high misorientation angles of new grains. A missing CPO and SPO indicate that the new grains were not markedly deformed after their formation. Deformation at low stress was instead concentrated in the host crystals forming the characteristic SWUE.

7.4.3 Recrystallization with CPO of new grains (DAV shear zone)

The quartz microfabrics of the DAV shear zone are characterized by new grains at orientations close to the host orientation, which do show a systematic CPO with high Schmid factors for basal <a> glide (Figs. 7.6–7.9). Some straight HAGBs decorated by fluid inclusions (Fig. 7.10 e) suggest that fracturing did play a role, and that microfractures

healed during subsequent SIGBM. Van Daalen et al. (1999) interpreted very similar micro-shear zones to occur along fractures generated along positive and negative rhomb planes of quartz. They suggested that rigid-body rotation of small fragments along the fractures corresponding to the shear sense of the shear zones caused the observed CPO. Increasing temperatures were interpreted to lead to grain-boundary migration and healing. This latest stage would involve recovery and reduction of dislocations. A subsequent increase in stresses to produce the observed high dislocation density would be required. However, a complex thermal history of deformation at increasing temperature after deformation at low temperature is not evident from any other observations of the DAV shear zone. In the DAV samples, fluid inclusions in quartz, especially along grain boundaries, occurring along with some evidence of healed microcracks (Fig. 7.10). Yet, evidence of a marked influence of precipitation from the fluid phase as suggested from quartz shear zones by Kjøll et al. (2015) and Goncalves et al. (2016), for example, other silicate phases in the recrystallized quartz aggregates, strain shadows or strain caps, are not evident. Instead, the marked CPO, LAGBs and high dislocation densities (Fig. 7.10) indicate the importance of crystal-plastic deformation. It is suggested here, based on the light-microscopic, SEM and TEM observations, that original grains with low Schmid factor for basal <a> glide, the system with the lowest CRSS at greenschist facies conditions (e.g. Hobbs, 1985; Passchier & Trouw, 2005; Law, 2014), were deformed by low-temperature plasticity. Dislocation pile-up along planes of high resolved shear stress lead to local strain concentration with fracturing initiating conjugate highly damaged zones (Fig. 7.1). Along these zones, new grains eventually develop from dislocation-poor domains surrounded by a high dislocation density mainly by subgrain rotation and SIGBM (Fig. 7.10 b & c), and figure 7.10 f may illustrate a recovered late stage. In contrast to the Silvretta quartz microfabrics, however, new grains from the DAV quartz shear zones show evidence of crystal-plastic deformation including a marked CPO, SPO (Figs. 7.6; 7.8 & 7.9) and moderately high dislocation density (Fig. 7.10 b & c). Growth of grains with orientations at high Schmid factor for basal <a> glide is favoured during creep with dynamic subgrain-rotation recrystallization leading to the observed CPO (Fig. 7.1 b). The microfabrics compare very well to the experiments of Trepmann et al. (2007, their Fig. 8) and Trepmann & Stöckhert (2013), in which localized strings of recrystallized grains with SPO, with long axes of grains perpendicular to the shortening direction and CPO, characterized by high Schmid factors for the activated glide system, were produced after low-temperature plasticity during creep, where stresses were kept at a constant level of about 250 MPa (Fig. 7.1 b).

Overall, the main difference for the microfabric of the DAV sample as compared to the microfabric of the Silvretta fault rocks is that the new grains are deformed by dislocation creep. In detail, the formation of the new grain involved two possibilities: (1) The new grains formed by dynamic recrystallization after high-stress crystal- plasticity at relaxing stresses but at a stress level still sufficiently high for effective dislocation creep (Fig. 7.1 b & c). (2) Or, new grains were deformed in a separate subsequent deformation event after a marked hiatus. Such a scenario cannot be ruled out. Yet, because of the good agreement with the experimental results and missing further evidence for two independent deformation events, the first possibility (Fig. 7.1 b) is favored here.

7.4.4 Differences in stress relaxation rates

One important goal for the analyzes of microfabrics of natural fault rocks is to provide quantitative constraints on the stress history. Therefore, experimental calibrations of stress-dependent microstructures, i.e. paleopiezometers, have been widely applied. A prerequisite for the use of paleopiezometer is that the same processes that produce a specific microstructure are found in experiment and nature, which is difficult to prove. Secondly, paleopiezometers require steady-state flow with a steady-state microstructure and no modification after deformation, but deformed grain in natural shear zones may not have experienced such a simple deformation history (Poirier, 1985; White et al., 1985; Trepmann & Stöckhert, 2003, 2009). The most reliable paleopiezometer is commonly thought to be recrystallized grain size, which is inversely proportional to stress during steady-state dislocation creep (Twiss, 1977; Poirier & Guillopé, 1979; Poirier, 1985; White et al., 1985; Stipp & Tullis, 2003). For the microfabrics in the study stresses relaxed during development of new grains, where the prerequisite of steady state flow is clearly not met. Grain-size reduction most probably resulted during early stages of SIGBM after initial low-temperature plasticity. Consequently, the grain size can be expected to be negatively correlated to the accumulated bulk strain during preceding low-temperature plasticity, equivalent to the effects of static recrystallization after cold working in materials sciences, where strain affects the number of nucleation sites (e.g. Nicolas & Poirier, 1976; Humphreys & Hatherly, 2004). SIGBM during later stages at already low stress resulted in a modified coarser grain size. This behavior is thought to be especially true for the Silvretta fault rocks, where the new grains are found to show no marked evidence of deformation by dislocation creep. For the DAV quartz shear zones, though, dynamic subgrain-rotation recrystallization in the regime of dislocation creep is indicated by a CPO, SPO and high dislocation density of new grains. Therefore, for the DAV samples, a recrystallized grain-size paleopiezometer may roughly constrain the differential stress during a late stage of dislocation creep. (Stipp & Tullis, 2003, equation 1) experimentally calibrated the grain size for subgrain rotation recrystallization in the dislocation creep (regimes 2 and 3 of Hirth & Tullis, 1992):

$$D = 10^{3.56+0.27} \cdot \sigma_d^{-1.26+0.13}$$

where σ_d denotes the differential stress in MPa and D the recrystallized grain size in mm.

For the DAV samples, this paleopiezometer yields flow stresses in the range of about 75–300 MPa for the recrystallized grain size of 10 ± 5 mm determined by EBSD, which is consistent with findings of Stöckhert et al. (1999). Similar stress conditions were kept during creep in the experiments of Trepmann et al. (2007) and Trepmann & Stöckhert (2013) resulting in microfabrics that are comparable to those of the DAV shear zone described here. This suggests that after low-temperature plasticity, stresses relaxed to a few hundred MPa, which persisted sufficiently long to accumulated notable strain by dislocation creep. In contrast, for the Silvretta fault rocks, stresses during formation of new grains were too small to accumulate significant strain by dislocation creep.

It is believed here that it is unfortunately not possible to infer quantitative constraints for the initial peak stresses during low-temperature plasticity from the quartz microfab-

rics, given the transient and non-steady state nature of deformation as well as the intense modification of the microfabrics during subsequent creep at relaxing stresses. However, given the relation of the quartz microfabrics of the Silvretta fault rocks to pseudotachylytes, the peak stresses were likely not less than those for the DAV fault rocks, which would mean that the stress relaxation rates are greater for the Silvretta fault rocks when compared to the DAV fault rocks.

Trepmann & Stöckhert (2001) inferred transient peak stresses on the order of 500 MPa at greenschist facies conditions from the orientation distribution of twinned and untwinned jadeite crystals in metagranites from the Sesia zone, which show quartz microfabrics that compare very well to those of the DAV (Trepmann & Stöckhert, 2003). The transient peak stresses for the initial low temperature plasticity of quartz recorded by the DAV fault rocks are therefore assumed to be of the same order of magnitude.

7.4.5 Implications of seismic activity of the fault systems

Flow laws describe the experimentally calibrated stress dependence on strain rate at given ambient conditions (e.g. temperature, pressure) for a specific material (e.g. mineral phases, microfabric) during steady-state deformation (i.e. stress and strain-rate are constant at increasing strain). The flow law that yields the lowest strain rate at given deformation conditions is supposed to control the rheology (Evans & Kohlstedt, 1995). At temperatures above 300 °C, dislocation creep of quartz with dynamic recrystallization is supposed to be the most effective deformation regime, controlling long-term rheology of the middle crust (Hirth & Tullis, 1992, 1994; Kohlstedt et al., 1995; Stöckhert et al., 1999; Hirth et al., 2001). The microstructural evidence of low-temperature plasticity of quartz with microcracking at temperatures above 300 °C suggests that stress-loading rates exceeded the stress relaxation that could be accommodated by long-term dislocation creep.

Stress redistribution from major earthquakes within a seismogenic zone can cause such high stress-loading rates with transient peak stresses that rapidly relax at depth levels just below the seismogenic zone (Ellis & Stöckhert, 2004; Nüchter & Stöckhert, 2008; Nüchter & Ellis, 2010). Also, internal crystal-plastic instabilities during creep that cause strain hardening, can create fast stress loading rates below the seismogenic zone (e.g. Hobbs et al., 1986; Hobbs & Ord, 1988; White, 1996, 2004, 2012). In this latter case, low-temperature plasticity would post-date dislocation creep. Yet, the microstructures in the study area record that low-temperature plasticity pre-dates recrystallization, given that recrystallized grains occur along precursory highly damaged zones generated during low-temperature plasticity. Especially the Silvretta microfabrics, a stage of intense dislocation creep is not recorded. For the DAV-mylonites, however, the evidence of dislocation creep might also imply an influence of crystal-plastic instabilities. Yet, internal stress-loading below the seismogenic zone can trigger earthquakes in the overlying upper crust or even earthquake-like behavior below the seismogenic zone (e.g. Hobbs et al., 1986; Hobbs & Ord, 1988; White, 2012), implying seismic activity for the particular fault system.

For the chosen prominent Silvretta basal thrust, that is the detachment of a major crystalline nappe from its original crystalline basement, seismic activity is consistent

with the widespread occurrence of pseudotachylytes (e.g. Masch & Koch, 1992; Schmutz, 1995). Pseudotachylytes are also recorded for the DAV (Mancktelow et al., 2001) and the steeply inclined sinistral DAV shear zone with some tens of kilometres of horizontal and a few kilometres of vertical component most likely related to seismic activity in shallower parts of the fault system. Thus, the microfabrics that record deformation and recrystallization at relaxing stresses, are interpreted to reflect the stress history related to seismic activity of the fault systems.

Yet, the question arises as to why the recorded stress relaxations rates are so different for the two fault systems. Relaxation after transient peak stresses is probably dependent on far-field tectonic stresses and ambient temperature conditions but clearly also on the deformation mechanisms, which in turn influence stress relaxation rates, causing feedback. The ambient pressure and temperature conditions, the lithology, as well as the deformation mechanism are quite similar for the two compared fault systems. The most prominent difference, however, is the tectonic setting: The Silvretta fault rocks are related to the detachment of the crystalline nappe from its crystalline substratum (Laubscher, 1983; Thöni, 1988; Masch & Koch, 1992; Schmutz, 1995). After detachment, i.e. after formation of the fault rocks, the nappe was transported onto the Penninic units during rather low-stress conditions. The DAV fault rocks, in contrast are related to a steeply dipping strike-slip fault with movement of tens of kilometres of horizontal component and a few kilometres of vertical component (Kleinschrodt, 1987; Schulz, 1989; Ratschbacher et al., 1991; Stöckhert et al., 1999; Mancktelow et al., 2001), where stresses should have stayed moderately high for a longer period of time.

7.5 Conclusion and summary

Quartz microfabrics from the Silvretta fault rocks and DAV shear zone record a switch from low-temperature plasticity at high stress to creep at relaxing stresses and lower greenschist facies conditions. This stress history is interpreted to be related to seismic activity of the host fault systems. For both microfabrics, the development of new grains is dominantly by subgrain rotation and subsequent strain-induced grain-boundary migration in areas of localized high strain developed during initial low-temperature plasticity with associated microcracking. Characteristic differences in the microfabric of new grains are suggested to reflect differences in stress and strain during creep, i.e. different relaxation rates from transient peak stresses. During creep at low stresses, new grains grew from highly damaged zones at almost random crystallographic orientations – as indicated by the quartz microfabrics from Silvretta fault rocks (Figs. 7.2–7.5). Strain is accumulated by dynamic recovery in the host grains resulting in a marked SWUE (Figs. 7.2 d & 7.4), whereas new grains did not accumulate notable strain by dislocation creep. At slow relaxation rates, i.e. during creep at stress levels of a few hundred MPa, formation of new grains along former highly-damaged zones occur with marked SPO and CPO characterized by high Schmid-factor for the favourable glide system, as indicated by the quartz microfabrics from the DAV shear zone (Figs. 7.6–7.10). The characteristic differences in shape and crystallographic orientation relation of new grains provide important information about the deformation and stress histories in natural shear zones from different tectonic regimes.

8 Summary and conclusions

In the first two parts of this thesis mylonitic pegmatites from the Austroalpine basement south of the western Tauern Window ("Pfunderer Berge") were investigated to analyze the deformation behavior of feldspars and to study the formation and age of apatite-allanite/epidote coronas around monazite and xenotime, developed in some of these rocks. To this end, over 100 samples were collected during field work and investigated by (electron) microscopy, microtextural analysis by EBSD and geochronological methods.

8.1 Deformation behavior of feldspar at greenschist-facies conditions

All oberservations presented in chapter 5 confirm that the pegmatites were deformed at greenschist-facies conditions (400–450 °C). At these conditions quartz deformed by dislocation creep producing, in high strain samples, monophase quartz ribbons with a strong CPO. Both albitic plagioclase and K-feldspar show evidence that dislocation creep of feldspar was not effective at these conditions. They were rather deformed by a combination of fracturing, glide and dissolution-precipitation processes.

K-feldspar mostly deformed by microcracking, which leads to grain size reduction and the formation of polyphase aggregates. Additionally albite replaced K-feldspar at it's rim, producing a serrated grain boundary. This replacement happened through an interface-coupled dissolution-precipitation process.

Albite, on the other hand is deformed by a combination of fracturing and dislocation glide. Small, strain-free albite grains surround albite porphyroclasts at sites of high stresses. These aggregates have weak CPOs, which are about the same orientation as that of the replaced porphyroclasts. As evidence of dislocation climb is systematically missing, this microstructure is interpreted to have been formed by the growth of small undeformed nuclei from strongly deformed parts of the former clast. These nuclei grew and replaced deformed parts. In general, these new grains have slightly lower An-contents than the porphyroclasts, indicating an additional but small chemical driving force for the replacement

These processes lead to the development of monophase albite layers, which, together with recrystallized quartz layers, form the mylonite's foliation. This albite matrix deformed by granular flow, combined with overgrowth, forming a SPO, but losing it's CPO. The strength of the SPO is dependent on the overall strain of the samples.

This investigation shows that microstructures, like monophase layers of small grains and small grains surrounding porphyroclasts do not have to be produced by dislocation creep. This is consistent with the fact that in feldspars dislocation climb should not be effective at greenschist-facies conditions.

8.2 Coronas around monazite and xenotime

The corona structures found in the mylonitic pegmatites consist of an inner zone of small isometric apatites and small disseminated allanite and thorite grains (Chapter 6). The outer zone is formed by radiating grains of allanite grading into REE-bearing epidote in

the case of coronas around monazite and only HREE-epidote in the case of xenotime. Electron microprobe measurements showed that the monazite and xenotime cores all have distinct domains with different chemistry and ages.

All measured monazites and xenotimes contain zones which could be dated to ∼ 270–280 Ma, the same as magmatic ages reported for pegmatites from this area (Borsi et al., 1980; Knoll et al., 2018). This shows well that altered monazites and xenotimes still contain age information retrievable by spatially resolved chemical dating. Two other age populations could be found: one at ∼ 170–200 Ma and one with a mean age of 66 ± 6 Ma. The last one corresponds well to the age of 50–60 Ma, which was determined for allanite in one corona by LA-ICP-MS dating. Thus, at least part of the replacement of magmatic monazite by secondary monazite happened during corona formation.

The general microstructure of the coronas can be explained by different nucleation environments for apatite and allanite. Apatite forms by interface-controlled precipitation. Thus apatite nucleates immediately after monazite/xenotime dissolved, using the PO_4-tetrahedra of their lattice. This was corroborated by EBSD measurements, the first ones done on such corona systems. These measurements show that the apatite grains show a weak CPO that is inherited from their monazite/xenotime precursor. The preferential incorporation of LREE by allanite, together with differential solubility of LREE and HREE and restricted transport through the fluid phase lead to the observed REE gradients in the coronas.

By considering the relationship between the mylonitic foliation, it was established that the coronas formed during deformation of the pegmatites. Firstly, the coronas are flattened parrallel to the foliation and secondly, the foliation is deflected by the coronas. Additionally some grains in the outer allanite/epidote zone show signs of deformation. Thus, the coronas' age of 50–60 Ma provides a new marker in the deformation history in the Austroalpine basement south of the western Tauern Window.

8.3 Recrystallization of quartz after low-temperature plasticity

The third part of this thesis (Chapter 7) was concerned with the quartz microstructures of two fault zones in the Austroalpine basement, the Defereggen-Antholz-Vals shear zone and the Silvretta basal thrust. In both samples, coarse grains inside quartz veins are deformed and show lamellar undulating extinction and in the case of the DAV samples also deformation lamellae. These grains are cut by micro-shear zones, often in conjugate sets, in which small recrystallized grains occur. But the microstructures of these small grains differ in some aspects.

In the Silvretta samples, the small grains do not show a marked CPO and no systematic variation of Schmid factors for any glide system. The uncorrelated misorientation angle distribution between the new grains is random and misorientations are often between 40–90°. Transmission electron microscopy shows a low dislocation density inside the new grains, compared to the big grains, and no fluid inclusions were found.

In the DAV samples, the new, small grains in conjugate micro-shear zones show a CPO in such a way that their c-axes are rotated away from the host's c-axis, corresponding to their respective sense of shear, assuming a shortening direction perpendicular to the foliation of the sample. Most of the new grains have orientations with a high Schmid

factor for basal-<a> glide. Misorientation distributions show an excess of small angles for both neighboring and random grain pairs. Under the transmission electron microscope these new grains have a heterogeneously developed, moderately high dislocation density and abundant fluid inclusions decorating high angle grain boundaries.

These differences in microstructure reflect different stress histories. In both cases, new grains were formed by subgrain rotation, associated with microcracking at high transient peak stresses. This is interpreted to be related to seismic activity of the two fault systems. After this phase of low-temperature plasticity the samples experienced different levels of stress relaxation. In the Silvretta case the new grains grew at almost random orientation at conditions of high relaxation rates, i.e. relatively low stresses. On the other hand, the new grains in the DAV samples, the new grains formed during creep at higher stress levels and developed a marked CPO and SPO.

This shows that these differences in microstructure contain crucial information about the deformation history in shear zones and that careful examination of such structures provides inside about stress changes in the seismogenic zone.

8.4 Deformation and reactions at greenschist-facies conditions

The deformation behavior of feldspar and quartz, together with the mineralogy of the deformed pegmatites, shows that the mylonitic foliation was formed at middle greenschist-facies conditions, i.e. 400 ± 50 °C, during the Alpine orogeny. These conditions correspond to the part of the lithosphere just below the seismogenic zone (e.g. Scholz, 2002). During earthquakes transient, very high differential stresses can be induced in this area (Ellis & Stöckhert, 2004; Nüchter & Ellis, 2010). Although the microfabric of the pegmatites does not necessarily reflect very high stresses, the deformation behavior of feldspar at greenschist-facies conditions (Chapter 7) is similar to that of quartz under high stresses (Chapter 5). The deformation is dominated by a combination of microfracturing and dislocation glide, while dislocation creep is not effective. This is commonly known as low-temperature plasticity. In contrast to quartz though, dissolution-precipitation processes are an important factor in the deformation behavior of feldspars.

High stress, episodic deformation related to the seismic circle, as recorded by the quartz fabric of gneisses from the DAV shear zone (Chapter 7) has also been related to localized, episodic fluid flow and the initiation of metamorphic reactions and dissolution-precipitation processes (e.g. Nüchter & Stöckhert, 2008; Billia et al., 2013; Wintsch & Yeh, 2013; Putnis et al., 2017). This episodic fluid availability is indicated by the coronas developed around monazite and xenotime in the mylonitic pegmatites (Chapter 6), whose degree of development is dependent on local fluid availability and which record episodic dissolution of monazite and xenotime as well as precipitation of allanite.

References

Abart, R.; Heuser, D. & Habler, G. (2014). Mechanisms of myrmekite formation: case study from the Weinsberg granite, Moldanubian zone, Upper Austria. *Contributions to Mineralogy and Petrology*, 168(5): 1–15, doi:10.1007/s00410-014-1074-7.

Andrews, J. (1984). Fracture controlled feldspar shape fabrics in deformed quartzofeldspathic rocks. *Journal of Structural Geology*, 6(1-2): 183–188.

Armbruster, T.; Bonazzi, P.; Akasaka, M.; Bermanec, V.; Chopin, C.; Gieré, R.; Heuss-Assbichler, S.; Liebscher, A.; Menchetti, S.; Pan, Y. & Pasero, M. (2006). Recommended nomenclature of epidote-group minerals. *European Journal of Mineralogy*, 2: 551–567, doi:10.1127/0935-1221/2006/0018-0551.

Austin, N.J. & Evans, B. (2007). Paleowattmeters : A scaling relation for dynamically recrystallized grain size. *Geology*, 35(4): 343–346, doi:10.1130/G23244A.1.

Bachmann, F.; Hielscher, R. & Schaeben, H. (2010). Texture Analysis with MTEX – Free and Open Source Software Toolbox. *Solid State Phenomena*, 160: 63–68, doi:10.4028/www.scientific.net/SSP.160.63.

Bachmann, R.; Oncken, O.; Glodny, J.; Seifert, W.; Georgieva, V. & Sudo, M. (2009). Exposed plate interface in the European Alps reveals fabric styles and gradients related to an ancient seismogenic coupling zone. *Journal of Geology*, 114: 1–23, doi:10.1029/2008JB005927.

Bea, F. (1996). Residence of REE, Y, Th and U in granites and crustal protoliths; implications for the chemistry of crustal melts. *Journal of Petrology*, 37(3): 521–552, doi:10.1093/petrology/37.3.521.

Behrmann, J. & Mainprice, D. (1987). Deformation mechanisms in a high-temperature quartz-feldspar mylonite: evidence for superplastic flow in the lower continental crust. *Tectonophysics*, 140(2-4): 297–305, doi:10.1016/0040-1951(87)90236-8.

Bergmann, R.; Chan, R.H.; Hielscher, R.; Persch, J. & Steidl, G. (2016). Restoration of manifold-valued images by half-quadratic minimization. *Inverse Problems and Imaging*, 10(2): 281–304, doi:10.3934/ipi.2016001.

Bestmann, M.; Pennacchioni, G.; Nielsen, S.; Göken, M. & de Wall, H. (2012). Deformation and ultrafine dynamic recrystallization of quartz in pseudotachylyte- bearing brittle faults: A matter of a few seconds. *Journal of Structural Geology*, 38: 21–38, doi:10.1016/j.jsg.2011.10.001.

Billia, M.A.; Timms, N.E.; Toy, V.G.; Hart, R.D. & Prior, D.J. (2013). Grain boundary dissolution porosity in quartzofeldspathic ultramylonites: Implications for permeability enhancement and weakening of mid-crustal shear zones. *Journal of Structural Geology*, 53: 2–14, doi:10.1016/j.jsg.2013.05.004.

Bons, P.D. & den Brok, B. (2000). Crystallographic preferred orientation development by dissolution–precipitation creep. *Journal of Structural Geology*, 22(11-12): 1713–1722, doi:10.1016/S0191-8141(00)00075-4.

Borg, S.; Liu, W.; Pearce, M.; Cleverley, J. & MacRae, C. (2014). Complex mineral zoning patterns caused by ultra-local equilibrium at reaction interfaces. *Geology*, 42(5): 415–418, doi:10.1130/G35287.1.

Borsi, S.; Del Moro, A.; Sassi, F.P.; Visona, D. & Zirpoli, G. (1980). On the existence of Hercynian aplites and pegmatites in the lower Aurina valley (Ahrntal, Austrides, Eastern Alps). *Neues Jahrbuch für Mineralogie*, 11: 501–514.

Borsi, S.; Del Moro, A.; Sassi, F.P.; Zanferrari, A. & Zirpoli, G. (1978). New geopetrologic and radiometric data on the Alpine history of the Austridic continental margin south of the Tauern window (Eastern Alps). *Memorie di Scienze Geologiche*, 32(1): 1–19.

Borsi, S.; Del Moro, A.; Sassi, F.P. & Zirpoli, G. (1973). Metamorphic evolution of the Austridic rocks to the south of the Tauern Window (Eastern Alps). Radiometric and geo-petrologic data. *Mem Soc geol Ital*, 12: 549–571.

Bosse, V.; Boulvais, P.; Gautier, P.; Devidal, J.L.; Cherneva, Z.; Boulvais, P.; Ruffet, G.; Paquette, J.L.; Tiepolo, M.; Bosse, V. & Gerdjikov, I. (2008). Fluid-induced disturbance of the monazite Th–Pb chronometer: In situ dating and element mapping in pegmatites from the Rhodope (Greece, Bulgaria). *Chemical Geology*, 261(3-4): 286–302, doi:10.1016/j.chemgeo.2008.10.025.

Brace, W. & Kohlstedt, D.L. (1980). Limits on lithospheric stress imposed by laboratory experiments. *Journal of Geophysical Research*, 85(B11): 6248–6252.

Brander, L.; Svahnberg, H. & Piazolo, S. (2011). Brittle-plastic deformation in initially dry rocks at fluid-present conditions: transient behaviour of feldspar at mid-crustal levels. *Contributions to Mineralogy and Petrology*, 163(3): 403–425, doi:10.1007/s00410-011-0677-5.

Broska, I. & Siman, P. (1998). The breakdown of monazite in the Wesz-Carpathian Veporic orthogneisses and Tatric granites. *Geologica Carpathica*, 49: 161–167.

Broska, I.; Williams, T.C.; Janák, M. & Nagy, G. (2005). Alteration and breakdown of xenotime-(Y) and monazite-(Ce) in granitic rocks of the Western Carpathians, Slovakia. *Lithos*, 82(1-2): 71–83, doi:10.1016/j.lithos.2004.12.007.

Budzyń, B.; Harlov, D.E.; Kozub-Budzyń, G.A. & Majka, J. (2017). Experimental constraints on the relative stabilities of the two systems monazite-(Ce) – allanite-(Ce) – fluorapatite and xenotime-(Y) – (Y,HREE)-rich epidote – (Y,HREE)-rich fluorapatite, in high Ca and Na-Ca environments under P-T conditions of 200–1000 . *Mineralogy and Petrology*, 111(2): 183–217, doi:10.1007/s00710-016-0464-0.

Budzyń, B.; Harlov, D.E.; Williams, M.L. & Jercinovic, M.J. (2011). Experimental determination of stability relations between monazite, fluorapatite, allanite, and REE-epidote as a function of pressure, temperature, and fluid composition. *American Mineralogist*, 96(10): 1547–1567, doi:10.2138/am.2011.3741.

Budzyń, B. & Jastrzębski, M. (2016). Monazite stability and the maintenance of Th-U-total Pb ages during post-magmatic processes in granitoids and host metasedimentary rocks: A case study from the Sudetes (SW Poland). *Geological Quarterly*, 60(1): 104–121, doi:10.7306/gq.1254.

Bürgmann, R. & Dresen, G. (2008). Rheology of the Lower Crust and Upper Mantle: Evidence from Rock Mechanics, Geodesy, and Field Observations. *Annual Review of Earth and Planetary Sciences*, 36(1): 531–567, doi:10.1146/annurev.earth.36.031207.124326.

Burn, M.; Lanari, P.; Pettke, T. & Engi, M. (2017). Non-matrix-matched standardisation in LA-ICP-MS analysis: General approach, and application to allanite Th-U-Pb dating. *Journal of Analytical Atomic Spectrometry*, 32(7): 1359–1377, doi:10.1039/c7ja00095b.

Burov, E.B. (2007). Plate Rheology and Mechanics, volume 6. ISBN 9780444538031, doi:10.1016/B978-044452748-6.00102-4.

Burov, E.B. (2011). Rheology and strength of the lithosphere. *Marine and Petroleum Geology*, 28(8): 1402–1443, doi:10.1016/j.marpetgeo.2011.05.008.

Derez, T.; Pennock, G.; Drury, M.R. & Sintubin, M. (2014). Low-temperature intracrystalline deformation microstructures in quartz. *Journal of Structural Geology*, 71: 3–23, doi:10.1016/j.jsg.2014.07.015.

Didier, A.; Bosse, V.; Boulvais, P.; Bouloton, J.; Paquette, J.L.; Montel, J.M. & Devidal, J.L. (2013). Disturbance versus preservation of U-Th-Pb ages in monazite during fluid-rock interaction: Textural, chemical and isotopic in situ study in microgranites (Velay Dome, France). *Contributions to Mineralogy and Petrology*, 165(6): 1051–1072, doi:10.1007/s00410-012-0847-0.

Doherty, R.D.; Hughes, D.A.; Humphreys, F.J.; Jonas, J.J.; Jensen, D.J.; Kassner, M.E.; King, W.E.; McNelley, T.R.; McQueen, H.J. & Rollett, A.D. (1997). Current issues in recrystallization: a review. *Materials Science and Engineering*, A238: 219–274.

Döhler, K. (2012). Deformation related to the DAV Fault System in the Eastern Alps south of the Tauern window and west of the Tauferer valley. *Master Thesis. Ludwig-Maximilians universität München.*

Eberlei, T.; Habler, G.; Grasemann, B. & Abart, R. (2014). Upper-greenschist facies intragrain deformation of albite in mylonitic meta-pegmatite and the influence of crystallographic anisotropy on microstructure formation. *Journal of Structural Geology*, 69(PA): 47–58, doi:10.1016/j.jsg.2014.10.001.

Eisbacher, G.H.; Linzer, H.G.; Meier, L. & Polinski, R. (1990). A depth-extrapolated structural transect across the Northern Calcareous Alps of western Tirol. *Ec*, 83(3): 711–725.

Ellis, S. & Stöckhert, B. (2004). Elevated stresses and creep rates beneath the brittle-ductile transition caused by seismic faulting in the upper crust. *Journal of Geophysical Research*, 109: 1–10, doi:10.1029/2003JB002744.

Engi, M. (2017). Petrochronology Based on REE-Minerals: Monazite, Allanite, Xenotime, Apatite BT - Reviews in Mineralogy & Geochemistry. *Reviews in Mineralogy & Geochemistry*, 83: 365–418.

Evans, B. & Kohlstedt, D.L. (1995). Rheology of Rocks, pages 148–165. American Geophysical Union (AGU), ISBN 9781118668108, doi:10.1029/RF003p0148.

Finger, F.; Broska, I.; Roberts, Malcolm, P. & Schermair, A. (1998). Replacement of primary monazite by apatite-allanite-epidote coronas in an amphibolite facies granite gneiss from the eastern Alps. *American Mineralogist*, 83: 248–258.

Fitz Gerald, J. & Stünitz, H. (1993). Deformation of granitoids at low metamorphic grade. I: Reactions and grain size reduction. *Tectonophysics*, 221: 269–297.

Fliervoet, T.F. (1995). Deformation Mechanisms in Fine Grained Quartzo-Feldspathic Mylonites. Ph.D. thesis, Universiteit Utrecht.

Forer, U.; Tropper, P. & Mair, V. (2009). Lithologische Kartierung, Petrologie und Strukturgeologie am Tauernfenster-SÜdrand im Ahrntal (SÜdtirol, Italien). *Geo.Alp*, 6: 62–79.

Förster, H.J. (1998a). The chemical composition of REE-Y-Th-U-rich minerals in peraluminous accessory granites of the Erzgebirge-Fichtelgebirge region, Germany. Part I: The monazite-(Ce)-brabantite solid solution series. *American Mineralogist*, 83: 259–272, doi:10.2138/am-1998-3-409.

Förster, H.J. (1998b). The chemical composition of REE-Y-Th-U-rich minerals in peraluminous accessory granites of the Erzgebirge-Fichtelgebirge region, Germany. Part II: Xenotime. *American Mineralogist*, 83: 1302–1315, doi:10.2138/am-1998-3-409.

Förster, H.J. (2000). Cerite-(Ce) and Thorian Synchysite from the Niederbobritzsch Granite, Erzgebirge, Germany: implications for the differential mobility of the LREE and Th during alteration. *Canadian Mineralogist*, 38: 67–79.

Froitzheim, N.; Schmid, S.M. & Conti, P. (1994). Repeated change from crustal shortening to orogen-parallel extension in the Austroalpine units of Graubünden. *Eclogae Geologicae Helvetiae*, 87(2): 559–612.

Gapais, D. (1989). Shear structures within deformed granites: mechanical and thermal indicators. *Geology*, 17(12): 1144–1147, doi:10.1130/0091-7613(1989)017<1144:SSWDGM>2.3.CO.

Gardner, J.; Wheeler, J.; Wallis, D.; Hansen, L.N. & Mariani, E. (2017). Mineral replacement reactions as a precursor to strain localisation: an (HR-)EBSD approach. In AGU Fall Meeting.

Gieré, R. & Sorensen, S.S. (2004). Allanite and Other REE-Rich Epidote-Group Minerals. *Reviews in Mineralogy and Geochemistry*, 56(1): 431–493, doi:10.2138/gsrmg.56.1.431.

Giuntoli, F.; Lanari, P.; Burn, M.; Kunz, B.E. & Engi, M. (2018). Deeply subducted continental fragments - Part 2: Insight from petrochronology in the central Sesia Zone (western Italian Alps). *Solid Earth*, 9(1): 191–222, doi:10.5194/se-9-191-2018.

Gleason, G.C. & Tullis, J. (1993). Improving flow laws and piezometers for quartz and feldspar aggregates. *Geophysical Research Letters*, 20(19): 2111–2114.

Goncalves, P.; Poilvet, J.C.; Oliot, E.; Trap, P. & Marquer, D. (2016). How does shear zone nucleate? An example from the Suretta nappe (Swiss Eastern Alps). *Journal of Structural Geology*, 86: 166–180, doi:10.1016/j.jsg.2016.02.015.

Goswami-Banerjee, S. & Robyr, M. (2015). Pressure and temperature conditions for crystallization of metamorphic allanite and monazite in metapelites: a case study from the Miyar Valley (high Himalayan Crystalline of Zanskar, NW India). *Journal of Metamorphic Geology*, 33: 535–556, doi:10.1111/jmg.12133.

Grand'Homme, A.; Janots, E.; Seydoux-Guillaume, A.M.; Guillaume, D.; Bosse, V. & Magnin, V. (2016). Partial resetting of the U-Th-Pb systems in experimentally altered monazite: Nanoscale evidence of incomplete replacement. *Geology*, 44(6): 431–434, doi:10.1130/G37770.1.

Grand'Homme, A.; Janots, E.; Seydoux-Guillaume, A.M.; Guillaume, D.; Magnin, V.; Hövelmann, J.; Höschen, C. & Boiron, M. (2018). Mass transport and fractionation during monazite alteration by anisotropic replacement. *Chemical Geology*, (May): 1–18, doi:10.1016/j.chemgeo.2017.10.008.

Groshong, R.H. (1988). Low-temperature deformation mechanisms and their interpretation. *Geological Society of America Bulletin*, 100(9): 1329–1360, doi:10.1130/0016-7606(1988)100<1329.

Handy, M.R. (1989). Deformation regimes and the rheological evolution of fault zones in the lithosphere : the effects of pressure, temperature, grainsize and time. *Tectonophysics*, 163: 119–152.

Hansen, E.C. & Harlov, D.E. (2007). Whole-rock, phosphate, and silicate compositional trends across an amphibolite- to granulite-facies transition, Tamil Nadu, India. *Journal of Petrology*, 48(9): 1641–1680, doi:10.1093/petrology/egm031.

Harlov, D.E.; Wirth, R. & Hetherington, C.J. (2011). Fluid-mediated partial alteration in monazite : the role of coupled dissolution-reprecipitation in element redistribution and mass transfer. *Contributions to Mineralogy and Petrology*, 162: 329–348, doi:10.1007/s00410-010-0599-7.

Hentschel, F.; Trepmann, C.A. & Janots, E. (2019). Deformation of feldspar at greenschist facies conditions-the record of mylonitic pegmatites from the Pfunderer Mountains, Eastern Alps. *Solid Earth*, 10(1): 95–116, doi:10.5194/se-10-95-2019.

Hildyard, R.C.; Prior, D.J.; Mariani, E. & Faulkner, D.R. (2011). Characterization of microstructures and interpretation of flow mechanisms in naturally deformed, fine-grained anhydrite by means of EBSD analysis. *Geological Society, London, Special Publications*, 360(1): 237–255, doi:10.1144/SP360.14.

Hippertt, J. (1998). Breakdown of feldspar, volume gain and lateral mass transfer during mylonitization of granitoid in a low metamorphic grade shear zone. *Journal of Structural Geology*, 20(2-3): 175–193, doi:10.1016/S0191-8141(97)00083-7.

Hirth, G.; Teyssier, C. & Dunlap, W. (2001). An evaluation of quartzite flow laws based on comparisons between experimentally and naturally deformed rocks. *International Journal of Earth Sciences*, 90(1): 77–87, doi:10.1007/s005310000152.

Hirth, G. & Tullis, J. (1992). Dislocation creep regimes in quartz aggregates. *Journal of Structural Geology*, 14(2): 145–159.

Hirth, G. & Tullis, J. (1994). The brittle-plastic transition in experimentally deformed quartz aggregates. *Journal of Geophysical Research: Solid Earth*, 99(B6): 11,731–11,747.

Hobbs, B.E. (1968). Recrystallization of single crystals of quartz. *Tectonophysics*, 6(5): 353–401.

Hobbs, B.E. (1985). The Geological Significance of Microfabric Analysis. In H.R. Wenk, editor, Preferred Orientation in Deformed Metal and Rocks, pages 463–484, Academic Press, San Diego, ISBN 978-0-12-744020-0, doi:https://doi.org/10.1016/B978-0-12-744020-0.50027-4.

Hobbs, B.E. & Ord, A. (1988). Plastic instabilities: Implications for the origin of intermdiate and deep focus earthquakes. *Journal of Geophysical Research*, 93(B9): 10,521–10,540, doi:10.1029/JB093iB09p10521.

Hobbs, B.E. & Ord, A. (2015). Dramatic effects of stress on metamorphic reactions. *Geology Forum*, page e372, doi:10.1130/G37070C.1.

Hobbs, B.E.; Ord, A. & Teyssier, C. (1986). Earthquakes in the Ductile Regime? *Pure and Applied Geophysics*, 124: 309–336.

Hofmann, K.; Kleinschrodt, R.; Lippert, R.; Mager, D. & Stöckhert, B. (1983). Geologische Karte des Altkristallins südlich des Tauernfensters zwischen Pfunderer Tal und Tauferer Tal (Südtirol). *Der Schlern*, 57: 572–590.

Hoinkes, G.; Koller, F.; Rantitsch, G.; Dachs, E.; Höck, V.; Neubauer, F. & Schuster, R. (1999). Alpine metamorphism of the Eastern Alps. *Schweizerische mineralogische und petrographische Mitteilungen*, 79: 155–181.

Hövelmann, J.; Putnis, A.; Geisler, T.; Schmidt, B.C. & Golla-Schindler, U. (2010). The replacement of plagioclase feldspars by albite: Observations from hydrothermal experiments. *Contributions to Mineralogy and Petrology*, 159(1): 43–59, doi:10.1007/s00410-009-0415-4.

Humphreys, F. (2004). Nucleation in Recrystallization. *Materials Science Forum*, 467-470: 107–116, doi:10.4028/www.scientific.net/MSF.467-470.107.

Humphreys, F. & Hatherly, M. (2004). Recrystallization and Related Annealing Phenomena. Pergamon Press, 2nd edition.

Hurford, A.J.; Flisch, M. & Jäger, E. (1989). Unravelling the thermo-tectonic evolution of the Alps : a contribution from fission track analysis and mica dating. In Alpine Tectonics, pages 369–398, The Authors.

Ishii, K.; Kanagawa, K.; Shigematsu, N. & Okudaira, T. (2007). High ductility of K-feldspar and development of granitic banded ultramylonite in the Ryoke metamorphic belt, SW Japan. *Journal of Structural Geology*, 29(6): 1083–1098, doi:10.1016/j.jsg.2007.02.008.

Janots, E.; Engi, M.; Berger, A.; Allaz, J.; Schwarz, J.O. & Spandler, C. (2008). Prograde metamorphic sequence of REE minerals in pelitic rocks of the Central Alps: implications for allanite–monazite–xenotime phase relations from 250 to 610 °C. *Journal of Metamorphic Geology*, (26): 509–526, doi:10.1111/j.1525-1314.2008.00774.x.

Jaoul, O. & Tullis, J. (1984). The effect of varying water contents on the creep behaviour of Heavitree Quartzite. *Journal of Geophysical Research*, 89(B6): 4298–4312, doi:10.1029/JB089iB06p04298.

Jessel, M. (1987). Grain-boundary migration microstructures in a naturally deformed quartzite. *Journal of Structural Geology*, 9(8): 1007–1014.

Jiang, Z.; Prior, D.J. & Wheeler, J. (2000). Albite crystallographic preferred orientation and grain misorientation distribution in a low-grade mylonite: implications for granular flow. *Journal of Structural Geology*, 22(11-12): 1663–1674.

Jordan, P. (1988). The rheology of polymineralic rocks - an approach. *Geologische Rundschau*, 77(1): 285–294, doi:10.1007/BF01848690.

Kelly, N.M.; Harley, S.L. & Möller, A. (2012). Complexity in the behavior and recrystallization of monazite during high-T metamorphism and fluid infiltration. *Chemical Geology*, 322-323: 192–208, doi:10.1016/j.chemgeo.2012.07.001.

Kilian, R. & Heilbronner, R. (2017). Analysis of crystallographic preferred orientations of experimentally deformed Black Hills Quartzite. *Solid Earth*, 8(5): 1095–1117, doi:10.5194/se-8-1095-2017.

Kilian, R.; Heilbronner, R. & Stünitz, H. (2011). Quartz grain size reduction in a granitoid rock and the transition from dislocation to diffusion creep. *Journal of Structural Geology*, 33(8): 1265–1284, doi:10.1016/j.jsg.2011.05.004.

Kjøll, H.; Viola, G.; Menegon, L. & Sørensen, B. (2015). Brittle – viscous deformation of vein quartz under fluid-rich lower greenschist facies conditions. *Solid Earth*, 6: 681–699, doi:10.5194/se-6-681-2015.

Kleinschrodt, R. (1987). Quarzkorngefügeanalyse im Altkristallin südlich des westlichen Tauernfensters (Südtirol, Italien). *Erlanger geologische Abhandlungen*, 114: 1–82.

Knoll, T.; Schuster, R.; Huet, B.; Mali, H.; Onuk, P.; Horschinegg, M.; Ertl, A. & Giester, G. (2018). Spodumene pegmatites and related leucogranites from the austroalpine unit (eastern alps, central europe): Field relations, petrography, geochemistry, and geochronology. *Canadian Mineralogist*, 56(4): 489–528, doi:10.3749/canmin.1700092.

Kohlstedt, D.L.; Evans, B. & Mackwell, S. (1995). Strength of the lithosphere: Constraints imposed by laboratory experiments. *Journal of Geophysical Research*, 100(B9): 17,587–17,602, doi:10.1029/95JB01460.

Korolyuk, V. & Lepezin, G. (2009). The coefficients of heterovalent NaSi-CaAl interdiffusion in plagioclases. *Russian Geology and Geophysics*, 50(12): 1146–1152, doi:10.1016/j.rgg.2009.11.013.

Krakow, R.; Bennett, R.J.; Johnstone, D.N.; Vukmanovic, Z.; Solano-Alvarez, W.; Lainé, S.J.; Einsle, J.F.; Midgley, P.A.; Rae, C.M. & Hielscher, R. (2017). On three-dimensional misorientation spaces. *Proceedings. Mathematical, physical, and engineering sciences*, 473(2206): 20170,274, doi:10.1098/rspa.2017.0274.

Kroll, H. & Ribbe, P. (1983). Lattice Parameters, Composition and Al, Si Oder in Alkali Feldspars. In P.H. Ribbe, editor, Reviews in Mineralogy: Feldspar Mineralogy, chapter 3, pages 57–99, The Mineralogical Society of America.

Kruhl, J.H. (1987). Preferred lattice orientations of plagioclase from amphibolite and greenschist facies rocks near the lnsubric Line (Western Alps). *Tectonophysics*, 135: 233–242.

Kruse, R. & Stünitz, H. (2001). Dynamic recrystallization processes in plagioclase porphyroclasts. *Journal of Structural Geology*, 23: 1781–1802.

Küster, M. & Stöckhert, B. (1999). High differential stress and sublithostatic pore fluid pressure in the ductile regime — microstructural evidence for short-term post-seismic creep in the Sesia Zone , Western Alps. *Tectonophysics*, 303: 263–277.

Laubscher, H. (1983). Detachment, shear, and compression in the central Alps. In Contributions to the Tectonics and Geophysics of Mountain Chains, Geological Society of America, ISBN 9780813711584, doi:10.1130/MEM158-p191.

Law, R.D. (2014). Deformation thermometry based on quartz c-axis fabrics and recrystallization microstructures: A review. *Journal of Structural Geology*, 66: 129–161, doi:10.1016/j.jsg.2014.05.023.

Lister, G. & Hobbs, B.E. (1980). The simulation of fabric development during plastic deformation and its application to quartzite: the influence of deformation history. *Journal of Structural Geology*, 2(3): 355–370.

Lloyd, G.E. & Freeman, B. (1994). Dynamic recrystallization of quartz under greenschist conditions. *Journal of Structural Geology*, 16(6): 867–881.

Lo Pò, D.; Braga, R.; Massonne, H.J.; Molli, G.; Montanini, A. & Theye, T. (2016). Fluid-induced breakdown of monazite in medium-grade metasedimentary rocks of the Pontremoli basement (Northern Apennines, Italy). *Journal of Metamorphic Geology*, 34: 63–84, doi:10.1111/jmg.12171.

Maggetti, M. & Flisch, M. (1993). Evolution of the Silvretta Nappe, pages 469–484. Springer, Berlin, Heidelberg, ISBN 978-3-642-84640-3, doi:10.1007/978-3-642-84640-3_28.

Mainprice, D.; Bachmann, F.; Hielscher, R. & Schaeben, H. (2015). Descriptive tools for the analysis of texture projects with large datasets using MTEX: strength, symmetry and components. *Geological Society London, Special Publications*, 409(1): 251–271.

Mair, P.; Tropper, P.; Harlov, D.E. & Manning, C.E. (2017). The solubility of CePO4 monazite and YPO4 xenotime in KCl-H2O fluids at 800°C and 1.0 GPa: Implications for REE transport in high-grade crustal fluids. *American Mineralogist*, 102(12): 2457–2466, doi:10.2138/am-2017-6172.

Majka, J. & Budzyń, B. (2006). Monazite breakdown in metapelites from Wedel Jarlsberg Land, Svalbard - preliminary report. *Mineralogia Polonica*, 37(1): 61–69.

Mancktelow, N.S.; Meier, A.; Viola, G.; Müller, W.; Fügenschuh, B.; Seward, D. & Villa, I.M. (1999). The Periadriatic and adjacent fault systems in the Eastern Alps south and west of the Tauern Window. *Tübinger Geowissenschaftliche Arbeiten, Series A*, 52: 7–9.

Mancktelow, N.S.; Stöckli, D.; Grollimund, B.; Müller, W.; Fügenschuh, B.; Viola, G.; Seward, D. & Villa, I.M. (2001). The DAV and Periadriatic fault systems in the Eastern Alps south of the Tauern window. *International Journal of Earth Sciences*, 90(3): 593–622, doi:10.1007/s005310000190.

Marone, C. & Scholz, C.H. (1988). The depth of seismic faulting and the upper transition from stable to unstable slip regimes. *Geophysical Research Letters*, 15(6): 621–624.

Marshall, D. & Mclaren, A. (1977). Deformation mechanisms in experimentally deformed plagioclase feldspars. *Physics and chemistry of minerals*, 370(August 1976): 351–370, doi:10.1007/BF00308845.

Masch, L. & Koch, N. (1992). Formation of Alpine mylonites and pseudotachylytes at the base of the Silvretta nappe, Eastern Alps. *Tectonophysics*, 204: 289–306.

Mclaren, A. & Pryer, L.L. (2001). Microstructural investigation of the interaction and interdependence of cataclastic and plastic mechanisms in Feldspar crystals deformed in the semi-brittle ® eld. *Tectonophysics*, 335(1-2): 1–15.

Mehl, L. & Hirth, G. (2008). Plagioclase preferred orientation in layered mylonites: Evaluation of flow laws for the lower crust. *Journal of Geophysical Research: Solid Earth*, 113(5): 1–19, doi:10.1029/2007JB005075.

Menegon, L.; Pennacchioni, G. & Spiess, R. (2008). Dissolution-precipitation creep of K-feldspar in mid-crustal granite mylonites. *Journal of Structural Geology*, 30(5): 565–579, doi:10.1016/j.jsg.2008.02.001.

Menegon, L.; Pennacchioni, G. & Stünitz, H. (2006). Nucleation and growth of myrmekite during ductile shear deformation in metagranites. *Journal of Metamorphic Geology*, 24(7): 553–568, doi:10.1111/j.1525-1314.2006.00654.x.

Menegon, L.; Stünitz, H.; Nasipuri, P.; Heilbronner, R. & Svahnberg, H. (2013). Transition from fracturing to viscous flow in granulite facies perthitic feldspar (Lofoten, Norway). *Journal of Structural Geology*, 48: 95–112, doi:10.1016/j.jsg.2012.12.004.

Mercolli, I. & Oberhänsli, R. (1988). Variscan tectonic evolution in the Central Alps: a working hypothesis. *Schweizerische mineralogische und petrographische Mitteilungen*, 68: 491–500.

Montardi, Y. & Mainprice, D. (1987). A transmission electron microscopic study of the natural plastic deformation of calcic plagioclase (An 68-70). *Bulletin de Mineralogie*, 110: 1–14.

Montel, J.M.; Michèle Veschambre, S.F.; Nicollet, C. & Provost, A. (1996). Electron-microprobe dating of monazite: The story. *Chemical Geology*, 131: 37–53, doi:10.1016/j.chemgeo.2017.11.001.

Mukai, H.; Austrheim, H.; Putnis, C.V. & Putnis, A. (2014). Textural Evolution of Plagioclase Feldspar across a Shear Zone: Implications for Deformation Mechanism and Rock Strength. *Journal of Petrology*, 55(8): 1457–1477, doi:10.1093/petrology/egu030.

Müller, W.; Mancktelow, N.S. & Meier, M. (2000). Rb-Sr microchrons of synkinematic mica in mylonites: an example from the DAV fault of the Eastern Alps. *Earth and Planetary Science Letters*, 180: 385–397.

Nicolas, A. & Poirier, J.P. (1976). Crystalline plasticity and solid state flow in metamorphic rocks. Wiley, New York.

Norberg, N.; Neusser, G.; Wirth, R. & Harlov, D.E. (2011). Microstructural evolution during experimental albitization of K-rich alkali feldspar. *Contributions to Mineralogy and Petrology*, 162(3): 531–546, doi:10.1007/s00410-011-0610-y.

Nüchter, J.A. & Ellis, S. (2010). Complex states of stress during the normal faulting seismic cycle: Role of midcrustal postseismic creep. *Journal of Geophysical Research*, 115: 1–15, doi:10.1029/2010JB007557.

Nüchter, J.A. & Stöckhert, B. (2008). Coupled stress and pore fluid pressure changes in the middle crust: Vein record of coseismic loading and postseismic stress relaxation. *Tectonics*, 27: 1–23, doi:10.1029/2007TC002180.

Olesen, N.Ø. (1987). Plagioclase fabric development in a high-grade shear zone, Jotunheimen, Norway. *Tectonophysics*, 142(2-4): 291–308, doi:10.1016/0040-1951(87)90128-4.

Olsen, T.S. & Kohlstedt, D.L. (1984). Analysis of dislocations in some naturally deformed plagioclase feldspars. *Physics and Chemistry of Minerals*, 11(4): 153–160, doi:10.1007/BF00387845.

Ondrejka, M.; Putiš, M.; Uher, P.; Schmiedt, I.; Pukančik, L. & Konečný, P. (2016). Fluid-driven destabilization of REE-bearing accessory minerals in the granitic orthogneisses of North Veporic basement (Western Carpathians, Slovakia). *Mineralogy and Petrology*, pages 1–20, doi:10.1007/s00710-016-0432-8.

Ondrejka, M.; Uher, P.; Putiš, M.; Broska, I.; Bačík, P.; Konečný, P. & Schmiedt, I. (2012). Two-stage breakdown of monazite by post-magmatic and metamorphic fluids: An example from the Veporic orthogneiss, Western Carpathians, Slovakia. *Lithos*, 142-143: 245–255, doi:10.1016/j.lithos.2012.03.012.

Passchier, C.W. & Trouw, R.A. (2005). Microtectonics. Springer Berlin Heidelberg, Berlin, Heidelberg, ISBN 978-3-662-08736-7, doi:10.1007/978-3-662-08734-3.

Paterson, M. (1987). Problems in the extrapolation of laboratory rheological data. *Tectonophysics*, 133(1-2): 33–43, doi:10.1016/0040-1951(87)90278-2.

Paterson, M. & Luan, F. (1990). Quartzite rheology under geological conditions. *Geological Society, London, Special Publications*, 54(1): 299–307, doi:10.1144/gsl.sp.1990.054.01.26.

Pennacchioni, G.; Menegon, L.; Leiss, B.; Nestola, F. & Bromiley, G. (2010). Development of crystallographic preferred orientation and microstructure during plastic deformation of natural coarse-grained quartz veins. *Journal of Geophysical Research*, 115(B12): B12,405, doi:10.1029/2010JB007674.

Petrík, I.; Broska, I.; Lipka, J. & Siman, P. (1995). Granitoid Allanite-(Ce): Substitution Relations, Redox Conditions and Ree Distributions (on an Example of I-Type Granitoids, Western Carpathians, Slovakia). *Geologica Carpathica*, 46(2): 79–94.

Petrík, I. & Konečný, P. (2009). Metasomatic replacement of inherited metamorphic monazite in a biotite-garnet granite from the Nízke Tatry Mountains, Western Carpathians, Slovakia: Chemical dating and evidence for disequilibrium melting. *American Mineralogist*, 94(7): 957–974, doi:10.2138/am.2009.2992.

Pfiffner, A.O. (2015). Geologie der Alpen. UTB.

Pfiffner, O. & Ramsay, J. (1982). Constraints on geological strain rates: Arguments from finite strain states of naturally deformed rocks. *Journal of Geophysical Research*, 87(B1): 311–321, doi:10.1029/JB087iB01p00311.

Piazolo, S.; Bons, P.D.; Jessel, M.; Evans, L. & Passchier, C.W. (2002). Dominance of microstructural processes and their effect on microstructural development: insights from numerical modelling of dynamic recrystallization. In Deformation Mechanisms, Rheology and Tectonics: Current Status and Future Perspectives, pages 149–170, Geological Society, London.

Platt, J.P. & Behr, W. (2011a). Grainsize evolution in ductile shear zones: Implications for strain localization and the strength of the lithosphere. *Journal of Structural Geology*, 33: 537–550, doi:10.1016/j.jsg.2011.01.018.

Platt, J.P. & Behr, W. (2011b). Lithospheric shear zones as constant stress experiments. *Geology*, 39(2): 127–130, doi:10.1130/G31561.1.

Plümper, O. & Putnis, A. (2009). The Complex Hydrothermal History of Granitic Rocks: Multiple Feldspar Replacement Reactions under Subsolidus Conditions. *Journal of Petrology*, 50(5): 967–987, doi:10.1093/petrology/egp028.

Poirier, J.P. (1985). Creep of crystals: High-temperature deformation processes in metals, ceramics and minerals. Cambridge University Press, Cambridge, ISBN 9780521261777, doi:https://doi.org/10.1017/CBO9780511564451.

Poirier, J.P. & Guillopé, M. (1979). Deformation induced recrystallization of minerals. *Bulletin de Mineralogie*, 102: 67–74.

Prior, D.J. & Wheeler, J. (1999). Feldspar fabrics in a greenschist facies albite-rich mylonite from electron backscatter diffraction. *Tectonophysics*, 303: 29–49.

Putnis, A. (2008). Mineral sciences. Cambridge University Press.

Putnis, A. (2009). Mineral Replacement Reactions. *Reviews in Mineralogy and Geochemistry*, 70(1): 87–124, doi:10.2138/rmg.2009.70.3.

Putnis, A. & Austrheim, H. (2010). Fluid-Induced Processes: Metasomatism and Metamorphism. *Frontiers in Geofluids*, 11: 254–269, doi:10.1002/9781444394900.ch18.

Putnis, A.; Jamtveit, B. & Austrheim, H. (2017). Metamorphic Processes and Seismicity: the Bergen Arcs as a Natural Laboratory. *Journal of Petrology*, 58(10): 1871–1898, doi:10.1093/petrology/egx076.

Pyle, J.M. & Spear, F.S. (2000). An empirical garnet (YAG) - xenotime thermometer. *Contributions to Mineralogy and Petrology*, 138: 51–58, doi:10.1007/PL00007662.

Pyle, J.M.; Spear, F.S.; Rudnick, R.L. & McDonough, W.F. (2001). Monazite–Xenotime–Garnet Equilibrium in Metapelites and a New Monazite–Garnet Thermometer. *Journal of Petrology*, 42(11): 2083–2107, doi:10.1016/0022-328X(90)80211-H.

Raimondo, T.; Payne, J.; Wade, B.; Lanari, P.; Clark, C. & Hand, M. (2017). Trace element mapping by LA-ICP-MS : assessing geochemical mobility in garnet. *Contributions to Mineralogy and Petrology*, 172: 1–22, doi:10.1007/s00410-017-1339-z.

Ratschbacher, L.; Merle, O.; Davy, P. & Cobbold, P. (1991). Lateral extrusion in the eastern Alps, Part 1: Boundary conditions and experiments scaled for gravity. *Tectonics*, 10(2): 245–256, doi:10.1029/90TC02622.

Ree, J.H. (1990). High temperature deformation of octachloropropane: dynamic grain growth and lattice reorientation. In Deformation Mechanisms, Rheology and Tectonics, pages 363–368, The Geological Society of London.

Ree, J.H.; Kim, H.S.; Han, R. & Jung, H. (2005). Grain-size reduction of feldspars by fracturing and neocrystallization in a low-grade granitic mylonite and its rheological effect. *Tectonophysics*, 407(3-4): 227–237, doi:10.1016/j.tecto.2005.07.010.

Ribbe, P. (1983). The Chemistry, Structure and Nomenclature of Feldspars. In P.H. Ribbe, editor, Reviews in Mineralogy: Feldspar Mineralogy, chapter 1, pages 1–19, The Mineralogical Society of America.

Rosenberg, C.L. & Stünitz, H. (2003). Deformation and recrystallization of plagioclase along a temperature gradient : an example from the Bergell tonalite. *Journal of Structural Geology*, 25: 389–408.

Rubie, D.C. (1990). Mechanisms of reaction-enhanced deformability in minerals and rocks. In Deformation processes in minerals, ceramics and rocks, ISBN 978-94-011-6829-8, 978-94-011-6827-4.

Rutter, E.H. & Brodie, K.H. (1991). Lithosphere rheology-a note of caution. *Journal of Structural Geology*, 13(3): 363–367, doi:10.1016/0191-8141(91)90136-7.

Rybacki, E. & Dresen, G. (2004). Deformation mechanism maps for feldspar rocks. *Tectonophysics*, 382(3-4): 173–187, doi:10.1016/j.tecto.2004.01.006.

Satsukawa, T.; Ildefonse, B.; Mainprice, D.; Morales, L.F.; Michibayashi, K. & Barou, F. (2013). A database of plagioclase crystal preferred orientations (CPO) and microstructures – implications for CPO origin, strength, symmetry and seismic anisotropy in gabbroic rocks. *Solid Earth*, 4(2): 511–542, doi:10.5194/se-4-511-2013.

Schmid, S.M. (1994). Textures of geological materials: computer model predictions versus empirical interpretations based on rock deformation experiments and field studies. In H. Bunge; S. Siegesmund; W. Skrotzki & K. Weber, editors, Textures of Geological Materials., pages 279–301, DGM Informationsgesellschaft.

Schmid, S.M. & Casey, M. (1986). Complete fabric analysis of some commonly observed quartz C-axis patterns. *Geophysical Monograph Series*, 36: 263–286.

Schmid, S.M.; Fügenschuh, B.; Kissling, E. & Schuster, R. (2004). Tectonic map and overall architecture of the Alpine orogen. *Eclogae Geologicae Helvetiae*, 97(1): 93–117, doi:10.1007/s00015-004-1113-x.

Schmid, S.M.; Scharf, A.; Handy, M.R. & Rosenberg, C.L. (2013). The Tauern Window (Eastern Alps, Austria): a new tectonic map, with cross-sections and a tectonometamorphic synthesis. *Swiss Journal of Geosciences*, 106(1): 1–32, doi:10.1007/s00015-013-0123-y.

Schmutz, H. (1995). Geologische Untersuchungen im SW-Teil des Unterengadiner Fensters, Teil II: Die makroskopische Geometrie der Pseudotachylite in der Silvretta-Decke am NW-Rand des Unterengadiner Fensters. *Beitr. geol. Kt. Schweiz, NF*, 166: 73–123.

Scholz, C.H. (1998). Earthquakes and friction laws. *Nature*, 391: 37–42.

Scholz, C.H. (2002). The Mechanics of Earthquakes and Faulting 2nd edition. Cambridge University Press, 2nd edition, ISBN 0521652235.

Schulz, B. (1989). Jungalpidische Gefügeentwicklung entlang der Defereggen-Antholz-Vals-Linie (Osttirol, Österreich). *Jahrbuch der geologischen Bundesanstalt*, 132(4): 775–789.

Schulz, B. (1994). Microstructural Evolution of Metapelites from the Austroalpine Basement North of Staller Sattel During Pre-Alpine and Alpine Deformation and Metamorphism (Eastern Tyrol, Austria). *Jahrbuch der geologischen Bundesanstalt*, 137(1): 197–212.

Schulz, B.; Steenken, A. & Siegesmund, S. (2008). Geodynamic evolution of an Alpine terrane - the Austroalpine basement to the south of the Tauern Window as a part of the Adriatic Plate (eastern Alps). *Geological Society London, Special Publications*, 298: 5–44, doi:10.1144/SP298.2.

Schuster, R. (2004). THE AUSTROALPINE CRYSTALLINE UNITS IN THE EASTERN ALPS. *Ber. Inst. Erdwiss. K.-F.-Univ. Graz*, 9: 30–36.

Schuster, R. & Stüwe, K. (2008). Permian metamorphic event in the Alps. *Geology*, 36(8): 603, doi:10.1130/G24703A.1.

Schweinehage, R. (2000). Metamorphite der Silvrettadecke/Ostalpen: thermobarometrische und geochemische Untersuchungen zur präalpidischen Entwicklung. Ph.d. thesis, Universität Stuttgart, doi:http://dx.doi.org/10.18419/opus-691.

Seydoux-Guillaume, A.M.; Montel, J.M.; Bingen, B.; Bosse, V.; Parseval, P.D.; Paquette, J.l.; Janots, E. & Wirth, R. (2012). Low-temperature alteration of monazite : Fluid mediated coupled dissolution – precipitation, irradiation damage, and disturbance of the U-Pb and Th-Pb chronometers. *Chemical Geology*, 330-331: 140–158, doi:10.1016/j.chemgeo.2012.07.031.

Seydoux-Guillaume, A.M.; Paquette, J.L.; Wiedenbeck, M.; Montel, J.M. & Heinrich, W. (2002). Experimental resetting of the U-Th-Pb systems in monazite. *Chemical Geology*, 191: 165–181.

Shaocheng, J. & Mainprice, D. (1988). Natural deformation fabrics of plagioclase: implications for slip systems and seismic anisotropy. *Tectonophysics*, 147(1-2): 145–163, doi:10.1016/0040-1951(88)90153-9.

Shelley, D. (1979). Plagioclase preferred orientation, Foreshore Group metasediments, Bluff, New Zealand. *Tectonophysics*, 58: 279–290.

Shelley, D. (1989). Plagioclase and quartz preferred orientations in a low-grade schist: the roles of primary growth and plastic deformation. *Journal of Structural Geology*, 11(8): 1029–1037, doi:10.1016/0191-8141(89)90053-9.

Shelley, D. (1994). Spider texture and amphibole preferred orientations. *Journal of Structural Geology*, 16(5): 709–717.

Shigematsu, N. & Tanaka, H. (2000). Dislocation creep of fine-grained recrystallized plagioclase under low-temperature conditions. *Journal of Structural Geology*, 22(1): 65–79, doi:10.1016/S0191-8141(99)00132-7.

Siegesmund, S.; Heinrichs, T.; Romer, R.L. & Doman, D. (2006). Age constraints on the evolution of the Austroalpine basement to the south of the Tauern Window. *International Journal of Earth Sciences*, 96(3): 415–432, doi:10.1007/s00531-006-0115-5.

Simpson, C. & Wintsch, R. (1989). Evidence for deformation-induced K-feldspar replacement by myrmekite. *Journal of Metamorphic Geology*, 7: 261–275, doi:10.1111/j.1525-1314.1989.tb00588.x.

Sinha, S.; Alsop, G.I. & Biswal, T. (2010). The evolution and significance of microfracturing within feldspars in low-grade granitic mylonites: A case study from the Eastern Ghats Mobile Belt, India. *Journal of Structural Geology*, 32(10): 1417–1429, doi:10.1016/j.jsg.2010.07.006.

Skrotzki, W. (1994). Mechanisms of texture development in rocks. *Textures of geological materials*, pages 167–186.

Sláma, J.; Košler, J.; Condon, D.J.; Crowley, J.L.; Gerdes, A.; Hanchar, J.M.; Horstwood, M.S.; Morris, G.A.; Nasdala, L.; Norberg, N.; Schaltegger, U.; Schoene, B.; Tubrett, M.N. & Whitehouse, M.J. (2008). Plešovice zircon - A new natural reference material for U-Pb and Hf isotopic microanalysis. *Chemical Geology*, 249(1-2): 1–35, doi:10.1016/j.chemgeo.2007.11.005.

Smith, J. (1983a). Phase Equilibria of Plagioclase. In P.H. Ribbe, editor, Reviews in Mineralogy: Feldspar Mineralogy, chapter 9, pages 223–239, The Mineralogical Society of America.

Smith, J. (1983b). Some Chemical Properties of Feldspars. In P.H. Ribbe, editor, Reviews in Mineralogy: Feldspar Mineralogy, chapter 12, pages 281–296.

Spear, F.S. & Pyle, J.M. (2002). Apatite, Monazite, and Xenotime in Metamorphic Rocks. *Reviews in Mineralogy and Geochemistry*, 48(1): 293–335, doi:10.2138/rmg.2002.48.7.

Spiess, R.; Cesare, B.; Mazzoli, C.; Sassi, R. & Sassi, F.P. (2010). The crystalline basement of the Adria microplate in the eastern Alps: a review of the palaeostructural evolution from the Neoproterozoic to the Cenozoic. *Rendiconti Lincei*, 21(S1): 31–50, doi:10.1007/s12210-010-0100-6.

Spry, A.H. (1969). Metamorphic Textures. Pergamon Press, ISBN 1483160289.

Steenken, A.; Siegesmund, S.; Heinrichs, T. & Fügenschuh, B. (2002). Cooling and exhumation of the Rieserferner Pluton (Eastern Alps, Italy/Austria). *International Journal of Earth Sciences*, 91(5): 799–817, doi:10.1007/s00531-002-0260-4.

Stipp, M. & Kunze, K. (2008). Dynamic recrystallization near the brittle-plastic transition in naturally and experimentally deformed quartz aggregates. *Tectonophysics*, 448: 77–97, doi:10.1016/j.tecto.2007.11.041.

Stipp, M.; Stünitz, H.; Heilbronner, R. & Schmid, S.M. (2002). The eastern Tonale fault zone: a 'natural laboratory' for crystal plastic deformation of quartz over a temperature range from 250 to 700 °C. *Journal of Structural Geology*, 24: 1861–1884.

Stipp, M. & Tullis, J. (2003). The recrystallized grain size piezometer for quartz. *Geophysical Research Letters*, 30(21): 2088, doi:10.1029/2003GL018444.

Stöckhert, B. (1982). Deformation und retrograde Metamorphose im Altkristallin S' des westlichen Tauerfensters (Südtirol). Ph.D. thesis, Universität Erlangen-Nürnberg.

Stöckhert, B. (1984). K-Ar determinations on muscovites and phengites from deformed pegmatites, and the minimum age of Old Alpine deformation in the Austridic basement to the South of the western Tauern Window (Ahrn valley, Southern Tyrol, Eastern Alps). *Neues Jahrbuch für Mineralogie/Abhandlungen*, 150(2): 103–120.

Stöckhert, B. (1985). Pre-Alpine history of the Austridic basement to the south of the western Tauern Window (Southern Tyrol, Italy) - Caledonian versus Hercynian event. *Neues Jahrbuch für Geologie und Paläontologie/Monatshefte*, 10: 618–642.

Stöckhert, B. (1987). Das Uttenheimer Pegmatit-Feld (Ostalpines Altkristallin, Südtirol) Genese und alpine Überprägung. *Erlanger geologische Abhandlungen*, 114: 83–106.

Stöckhert, B.; Brix, M.R.; Kleinschrodt, R.; Hurford, A.J. & Wirth, R. (1999). Thermochronometry and microstructures of quartz - a comparison with experimental flow laws and predictions on the temperature of the brittle-plastic transition. *Journal of Structural Geology*, 21: 351–369.

Stünitz, H. (1998). Syndeformational recrystallization – dynamic or compositionally induced? *Contributions to Mineralogy and Petrology*, 131: 219–236.

Stünitz, H. & Fitz Gerald, J. (1993). Deformation of granitoids at low metamorphic grade. II : Granular flow in albite-rich mylonites. *Tectonophysics*, 221: 299–324.

Stünitz, H.; Fitz Gerald, J. & Tullis, J. (2003). Dislocation generation, slip systems, and dynamic recrystallization in experimentally deformed plagioclase single crystals. *Tectonophysics*, 372(3-4): 215–233, doi:10.1016/S0040-1951(03)00241-5.

Suzuki, K. & Kato, T. (2008). CHIME dating of monazite, xenotime, zircon and polycrase: Protocol, pitfalls and chemical criterion of possibly discordant age data. *Gondwana Research*, 14(4): 569–586, doi:10.1016/j.gr.2008.01.005.

Thöni, M. (1981). Degree and evolution of the Alpine metamorphism in the Austro Alpine Unit W of the Hohe Tauern in the light of K/Ar and Rb/Sr age determinations on micas. *Jahrbuch der geologischen Bundesanstalt*, 124: 111–174.

Thöni, M. (1988). Rb-Sr isotopic resetting in mylonites and pseudotachylites: implications for the detachment and thrusting of the Austroalpine basement nappes in the Eastern Alps. *Jahrbuch der geologischen Bundesanstalt*, 131: 169–201.

Trepmann, C.A. (2002). Microstructural Criteria for Synseismic Loading and Postseismic Creep in the Uppermost Plastosphere: An Example From the Sesia Zone, Western Alps. Ph.D. thesis.

Trepmann, C.A.; Hsu, C.; Hentschel, F.; Döhler, K.; Schneider, C. & Wichmann, V. (2017). Recrystallization of quartz after low-temperature plasticity – The record of stress relaxation below the seismogenic zone. *Journal of Structural Geology*, 95: 77–92, doi:10.1016/j.jsg.2016.12.004.

Trepmann, C.A.; Lenze, A. & Stöckhert, B. (2010). Static recrystallization of vein quartz pebbles in a high-pressure – low-temperature metamorphic conglomerate. *Journal of Petrology*, 32: 202–215, doi:10.1016/j.jsg.2009.11.005.

Trepmann, C.A. & Stöckhert, B. (2001). Mechanical twinning of jadeite - an indication of synseismic loading beneath the brittle-plastic transition. *International Journal of Earth Sciences*, 90: 4–13, doi:10.1007/s005310000165.

Trepmann, C.A. & Stöckhert, B. (2003). Quartz microstructures developed during non-steady state plastic flow at rapidly decaying stress and strain rate. *Journal of Structural Geology*, 25(12): 2035–2051, doi:10.1016/S0191-8141(03)00073-7.

Trepmann, C.A. & Stöckhert, B. (2009). Microfabric of folded quartz veins in metagreywackes: dislocation creep and subgrain rotation at high stress. *Journal of Metamorphic Geology*, 27: 555–570, doi:10.1111/j.1525-1314.2009.00842.x.

Trepmann, C.A. & Stöckhert, B. (2013). Short-wavelength undulatory extinction in quartz recording coseismic deformation in the middle crust – an experimental study. *Solid Earth*, 4: 263–276, doi:10.5194/se-4-263-2013.

Trepmann, C.A.; Stöckhert, B. & Chakraborty, S. (2004). Oligocene trondhjemitic dikes in the Austroalpine basement of the Pfunderer Berge, Südtirol – level of emplacement and metamorphic overprint. *European Journal of Mineralogy*, 16(4): 641–659, doi:10.1127/0935-1221/2004/0016-0641.

Trepmann, C.A.; Stöckhert, B.; Dorner, D.; Hamidzadeh Moghadam, R.; Küster, M. & Röller, K. (2007). Simulating coseismic deformation of quartz in the middle crust and fabric evolution during postseismic stress relaxation — An experimental study. *Tectonophysics*, 442: 83–104, doi:10.1016/j.tecto.2007.05.005.

Tröger, W. (1982). Optische Bestimmung der gesteinsbildenden Minerale. Teil I: Bestimmungstabellen. Schweizerbart'sche Verlagsbuchhandlung, 5. edition.

Tsurumi, J.; Hosonuma, H. & Kanagawa, K. (2003). Strain localization due to a positive feedback of deformation and myrmekite-forming reaction in granite and aplite mylonites along the Hatagawa Shear Zone of NE Japan. *Journal of Structural Geology*, 25(4): 557–574, doi:10.1016/S0191-8141(02)00048-2.

Tullis, J. (1983). Deformation of Feldspars. In P.H. Ribbe, editor, Reviews in Mineralogy: Feldspar Mineralogy, chapter 13, pages 297–323, The Mineralogical Society of America.

Tullis, J. & Yund, R.a. (1977). Experimental deformation of the dry Westerly granite. *Journal of Geophysical Research*, 82(36), doi:10.1029/JB082i036p05705.

Tullis, J. & Yund, R.A. (1985). Dynamic recrystallization of feldspar : A mechanism for ductile shear zone formation. *Geology*, 13: 238–241.

Tullis, J. & Yund, R.A. (1987). Transition from cataclastic flow to dislocation creep of feldspar: Mechanisms and microstructures. *Geology*, 15: 606–609.

Tullis, J. & Yund, R.A. (1991). Diffusion creep in feldspar aggregates : experimental evidence. *Journal of Structural Geology*, 11(9): 987–1000.

Tullis, J. & Yund, R.A. (1992). The Brittle-Ductile Transition In Feldspar Aggregates : An Experimental Study. *International Geophysics*, 51: 89–117.

Tullis, J.; Yund, R.A. & Farver, J. (1996). Deformation-enhanced fluid distribution in feldspar aggregates and implications for ductile shear zones. *Geology*, 24(1): 63–66, doi:10.1130/0091-7613(1996)024<0063:DEFDIF>2.3.CO;2.

Tullis, T. & Tullis, J. (1986). Experimental Rock Deformation Techniques, pages 297–324. American Geophysical Union (AGU), ISBN 9781118664353, doi:10.1029/GM036p0297.

Twiss, R.J. (1977). Theory and Applicability of a Recrystallized Grain Size Paleopiezometer. *Pure and Applied Geophysics*, 115: 227–244.

Upadhyay, D. & Pruseth, K.L. (2012). Fluid-induced dissolution breakdown of monazite from Tso Morari complex, NW Himalayas: evidence for immobility of trace elements. *Computers and Geosciences*, 164: 303–316, doi:10.1007/s00410-012-0739-3.

Van Daalen, M.; Heilbronner, R. & Kunze, K. (1999). Orientation analysis of localized shear deformation in quartz fibres at the brittle-ductile transition. *Tectonophysics*, 303: 83–107.

Vernooij, M.G.; den Brok, B. & Kunze, K. (2006). Development of crystallographic preferred orientations by nucleation and growth of new grains in experimentally deformed quartz single crystals. *Tectonophysics*, 427(1-4): 35–53, doi:10.1016/j.tecto.2006.06.008.

Villa-Vialaneix, N.; Montel, J.M. & Seydoux-Guillaume, A.M. (2013). NiLeDAM: Monazite Datation for the NiLeDAM team. *package version 0.1*, page R.

Voll, G. (1976). Recrystallization of Quartz, Biotite and Feldspars from Erstfeld to the Leventina Nappe, Swiss Alps, and its Geological Significance. *Schweizerische mineralogische und petrographische Mitteilungen*, 56: 641–647.

Wagner, R.; Rosenberg, C.L.; Handy, M.R.; Mobus, C. & Albertz, M. (2006). Fracture-driven intrusion and upwelling of a mid-crustal pluton fed from a transpressive shear zone-The Rieserferner Pluton (Eastern Alps). *Geological Society of America Bulletin*, 118(1-2): 219–237, doi:10.1130/B25842.1.

Wang, Y. & Marino, E. (1992). Dynamic model of oscillatory zoning of trace elements in calcite: Double layer, inhibition, and self-organization. *Geochimica et Cosmochimica Acta*, 56: 587–596.

Wassmann, S. & Stöckhert, B. (2013). Tectonophysics Rheology of the plate interface — Dissolution precipitation creep in high pressure metamorphic rocks. *Tectonophysics*, 608: 1–29, doi:10.1016/j.tecto.2013.09.030.

Wheeler, J. (2009). The preservation of seismic anisotropy in the Earth's mantle during diffusion creep. *Geophysical Journal International*, 178(3): 1723–1732, doi:10.1111/j.1365-246X.2009.04241.x.

Wheeler, J.; Jiang, Z.; Prior, D.J. & Tullis, J. (2004). Dynamic recrystallisation of quartz. *Materials Science Forum*, 467-470: 1243–1250, doi:10.4028/www.scientific.net/MSF.467-470.1243.

Wheeler, J.; Prior, D.J.; Jiang, Z.; Spiess, R. & Trimby, P. (2001). The petrological significance of misorientations between grains. *Contributions to Mineralogy and Petrology*, 141(1): 109–124, doi:10.1007/s004100000225.

White, J.C. (1996). Transient discontinuities revisited: pseudotachylyte, plastic instability and the influence of low pore fluid pressure on deformation processes in the mid-crust. *Journal of Structural Geology*, 18(12): 1471–1486.

White, J.C. (2004). Instability and localization of deformation in lower crust granulites, Minas fault zone, Nova Scotia, Canada. In G.I. Alsop; R. Holdsworth; K. McCaffrey & M. Hand, editors, Flow Processes in Faults and Shear Zones., pages 25–37, The Geological Society of London.

White, J.C. (2012). Paradoxical pseudotachylyte - Fault melt outside the seismogenic zone. *Journal of Structural Geology*, 38: 11–20, doi:10.1016/j.jsg.2011.11.016.

White, S. (1975). Tectonic deformation and recrystallisation of Oligoclase. *Contributions to Mineralogy and Petrology*, 50: 287–304, doi:10.1007/BF00394854.

White, S.; Burrows, S.; Carreras, J.; Shaw, N. & Humphreys, F. (1980). On mylonites in ductile shear zones. *Journal of Structural Geology*, 2(1): 175–187, doi:10.1016/0191-8141(80)90048-6.

White, S.; Drury, M.R. & Ion, S. (1985). Large strain deformation studies using polycrystalline magnesium as a rock analogue. Part I: grain size paleopiezometry in mylonite zones. *Physics of the Earth and Planetary Interiors*, 40: 201–207.

Whitney, D. & Evans, B.W. (2009). Abbreviations for names of rock-forming minerals. *American Mineralogist*, 95(1): 185–187, doi:10.2138/am.2010.3371.

Williams, M.L. & Jercinovic, M.J. (2012). Tectonic interpretation of metamorphic tectonites : integrating compositional mapping , microstructural analysis and in situ monazite dating. *Journal of Metamorphic Geology*, 30: 739–752, doi:10.1111/j.1525-1314.2012.00995.x.

Williams, M.L.; Jercinovic, M.J. & Hetherington, C.J. (2007). Microprobe Monazite Geochronology: Understanding Geologic Processes by Integrating Composition and Chronology. *Annual Review of Earth and Planetary Sciences*, 35(1): 137–175, doi:10.1146/annurev.earth.35.031306.140228.

Wing, B.A.; Ferry, J.M. & Harrison, T.M. (2003). Prograde destruction and formation of monazite and allanite during contact and regional metamorphism of pelites: petrology and geochronology. *Contributions to Mineralogy and Petrology*, 145: 228–250, doi:10.1007/s00410-003-0446-1.

Wintsch, R.P. & Yeh, M.W. (2013). Oscillating brittle and viscous behavior through the earthquake cycle in the Red River Shear Zone: Monitoring flips between reaction and textural softening and hardening. *Tectonophysics*, 587: 46–62, doi:10.1016/j.tecto.2012.09.019.

Wölfler, A.; Frisch, W.; Fritz, H.; Danišik, M. & Wölfler, A. (2015). Ductile to brittle fault zone evolution in Austroalpine units to the southeast of the Tauern Window (Eastern Alps). *Swiss Journal of Geosciences*, (108): 239–251, doi:10.1007/s00015-015-0193-0.

Yund, R.A. (1986). Interdiffusion of NaSi-CaAl in peristerite. *Physics and Chemistry of Minerals*, 13(1): 11–16, doi:10.1007/BF00307308.

Yund, R.A. & Tullis, J. (1991). Compositional changes of minerals associated with dynamic recrystallizatin. *Contributions to Mineralogy and Petrology*, 108(3): 346–355, doi:10.1007/BF00285942.

Appendix

A1 List of all samples

Sample	Locality	Coordinates	Elevation	Orientation	Description	Outcrop	Thin sections
FH1	Sambock	46°51'15.8" N 11°53'43.7" E	2382 m	336/65	Pegmatit	vor Plattform mit Panorama-Schild	a, b
FH2	Uttenheim	46°52'12.2" N 11°56'22.6" E	1129 m	–	oligozäner Gang, Schieferung wie Gangwand, FH3	Straßenaufschluss, direkt nach hoher Wand und 2 gemauerten Abschnitten	x
FH3	Uttenheim	46°52'12.2" N 11°56'22.6" E	1129 m	–	Kontakt olig. Gang mit Pegmatit, Schieferung in Gang parallel zu Kontakt (146/55)	"	–
FH4	Uttenheim	46°52'12.2" N 11°56'22.6" E	1129 m	152/35	Pegmatit, gelblich verwittert, sehr fein geschiefert: Scherzone	„	a, b
FH5	Uttenheim-Süd	46°52'26.2" N 11°56'0.8" E	1443 m	250/20	Pegmatit, fein geschiefert, Turmalin in Qz-reichen Lagen	„	a, b, c, TEM
FH6	Uttenheim-Süd	46°52'26.2" N 11°56'0.8" E	1443 m	263/17	Pegmatit, massig am Aufschluss, Muskovit jedoch fein	„	–
FH7	Uttenheim-Süd	46°51'40.2" N 11°55'47.0" E	1597 m	350/70	sehr feinkörniger Gang, leicht flaserige Schieferung	Straßenaufschluss, eine Kurve vor Einfahrt zu Hof	x
FH8	Uttenheim-Süd	46°51'39.4" N 11°55'54.7" E	1608 m	54/40	grobkörniger Pegmatit mit Granat	Straßenaufschluss, direkt an Einfahrt zu Hof	–
FH9	Uttenheim	46°52'12.2" N 11°56'22.6" E	1129 m	148/28	Pegmatit, gröber, über Scherzone FH4	Straßenaufschluss, direkt nach hoher Wand und 2 gemauerten Abschnitten	a, b
FH10	Mühlbach	46°50'48.5" N 11°58'24.7" E	1447 m	355/70	Pegmatit, Kontakt zu Paragneis parallel zu Schieferung	Straßenaufschluss, vor Ortseingangsschild	a, b
FH11	Putzenhöhe	46°51'52.8" N 11°51'50.7" E	2429 m	210/80	Pegmatit in Quarzit	kurz nach Gipfel auf der rechten Seite	–
FH12	Eidechs-spitze	46°52'10.2" N 11°45'37.9" E	2564 m	60/70	Pegmatit, kleiner Körper, knollig, unregelmäßig, Lagerung ok?	auf linker seite kurz vor dem direkten Gipfelaufstieg, leuchtet stark weiß	–
FH13	Eidechs-spitze	46°52'12.7" N 11°45'33.6" E	2617 m	354/16	Pegmatit, unterhalb von Qz-Gang, stark geschiefert, gut messbar	auf linker seite kurz vor dem direkten Gipfelaufstieg, über FH12, leuchtet stark weiß	a, b, TEM
FH14	Plattneralm/ Pfunders	46°52'56.9" N 11°43'48.9" E	1561 m	200/28	Pegmatit, recht stark verwittert	Wanderweg 21, nach gerodetem Waldstück	a, b, TEM
FH15	Plattneralm/ Pfunders	46°52'57.3" N 11°43'43.3" E	1548 m	324/15	dunkler, schiefriger Gneis	Wanderweg 21, direkt nach übergang zu altem Fahrweg	–
FH16	Plattneralm/ Pfunders	46°52'57.3" N 11°43'43.3" E	1548 m	334/38	Marmor, Wechselfolge mit schiefrigem Gneis	„	–
FH17	Plattneralm/ Pfunders	46°52'56.4" N 11°43'41.8" E	1539 m	50/18	Pegmatit, recht stark verwittert, zwischen Wurzeln, wirklich anstehend?	Wanderweg 21, direkt vor übergang zu altem Fahrweg, vor Geländer	–
FH18	Sambock	46°51'17.1" N 11°53'44.8" E	2396 m	336/73	Pegmatit, etwas zerklüftet	kleiner Aufschluss, direkt am Gipfelkreuz	–
FH19	Sambock	46°51'25.8" N 11°53'47.8" E	2382 m	125/35	Pegmatit, Schieferung/Bänderung, aber Glimmer nicht unbedingt parallel	nach Sambock, im Westhang, nach 1. Schuttfeld	–
FH20	Sambock	46°51'29.0" N 11°53'48.1" E	2372 m	332/79	Pegmatit, sehr feinkörnig, enthält aber Hellglimmer	nach 1. Schuttfeld, auf dem Grat	–
FH21	Sambock	46°51'31,9" N 11°53'48.2" E	2393 m	350/76	Pegmatit, grobkörnig, stark gebändert	auf dem 2. Grat	a, b
FH22	Sambock	46°51'45,9" N 11°53'48.3" E	2447 m	70/20	Pegmatit, sehr grobkörnig, grob gebändert, andere Aufschlüsse zeigen kaum Schieferung	kurz vor Ende des Sambockgrates, vor Gipfelschuttfeld	–
FH23	Sambock	46°51'52.1" N 11°53'35.9" E	2428 m	148/79	Pegmatit, grob gebändert, aber mit Biotit, Gneis direkt daneben	Grat Richtung Plattner Spitze, kurz vor Weg 67 ins Tal zurück	a, b

Sample	Locality	Coordinates	Elevation	Orientation	Description	Outcrop	Thin sections
FH24	Sambock	46°51’52.1" N 11°53’35.9" E	2428 m	289/79	Biotitgneis, O’Fläche leicht schräg zu Schieferung	Grat Richtung Plattner Spitze, kurz vor Weg 67 ins Tal zurück	–
FH25	Weitental	46°51’12.0" N 11°42’48.6" E	1447 m	354/24	Pegmatitgang rechts von Scherzone, siehe Skizze	erster Aufschluss, Scherzone & Quelle	x
FH26	Weitental	46°51’12.0" N 11°42’48.6" E	1447 m	340/26	Mylonit, extrem feine Schieferung, siehe Skizze	”	x
FH27	Weitental	46°51’13.0" N 11°42’52.1" E	1447 m	302/15	Pegmatit, in Bänderung mit Gneis	kleiner Aufschluss mit roter Kreuz-Markierung	a, b
FH28	Weitental	46°51’18.0" N 11°42’57.9" E	1447 m	98/39	Pegmatit,Schieferung recht wellig, etwas bröselig	großer Aufschluss vor Linkskurve	–
FH29	Weitental	46°51’18.0" N 11°42’57.9" E	1447 m	114/40	Pegmatit, Schieferung recht wellig, besser als FH28	rechts von FH28, am Ende des Aufschlusses	–
FH30	Weitental	46°51’20.8" N 11°42’55.5" E	1447 m	174/60	Pegmatit, Turmalin nicht zu sehen	–	–
FH30b	Weitental	46°51’20.8" N 11°42’55.5" E	1447 m	–	Pegmatit, mit Turmalin und Biotit?	–	–
FH31	Putzenhöhe	46°51’53.4" N 11°51’49.7" E	2487 m	150/77 & 88/53	Kalksilikatfels? Gefaltet, Schenkel gemessen, siehe Foto	Grünbachspitze, Nordhang	-
FH32	Putzenhöhe	46°51’53.4" N 11°51’49.7" E	2487 m	138/70	Schiefer?, leicht grünlich	"	x
FH33	Putzenhöhe	46°51’54.1" N 11°51’35.3" E	2425 m	82/35	Pegmatit, große hellrote Granate, am selben Aufschluss auch 142/13 gemessen	Grat zu Zwölferspitze	–
FH34	Mühlbach	46°51’36.7" N 11°58’9.1" E	1347 m	304/86	Pegmatitkörper, nicht geschiefert?, von beiden Seiten von gut geschiefertem Gneis begrenzt	kurz vor Hof	x
FH35	Weitental	46°51’12.0" N 11°42’48.6" E	1447 m	lose	lagiger Aufbau von Pegmatit und Paragneis, Krenulation	erster Aufschluss, Scherzone & Quelle	a, b
FH36	Weitental	46°51’12.0" N 11°42’48.6" E	1447 m	016/36	dunkler Quarzit, Knittelung nd starke Lineation	"	a, b, c
FH37	Weitental	46°51’12.0" N 11°42’48.6" E	1447 m	330/10 L: 60/0	stark geschieferter, feinkörniger Pegmatit	"	–
FH38	Weitental	46°51’12.6" N 11°42’50.2" E	1447 m	354/38	Pegmatitband in Gneisen mit Scherbändern	kurz nach der Quelle am Weg	–
FH39	Weitental	46°51’15.0" N 11°42’54.7" E	1449 m	012/65 L: 102/2	geschieferter Pegmatit mit Granat	Weg	a, b
FH40/b	Weitental	46°51’20.5" N 11°42’55.5" E	1452 m	beide lose	stark geschiefert mit Turmalin & Granat(?), b: mit Nebengestein	"	–
FH41a,b,c	Weitental	46°51’12.9" N 11°42’50.6" E	1448 m	alle lose	kaum geschiefert, mit Nebengestein	Weg, Wasserfall	–
FH43	Mühlbach	46°51’36.7" N 11°59’9.5" E	1293 m	180/80	Rand von Pegmatitkörper, schwach geschiefert, mit Granat	Straßenaufschluss	–
FH44	Mühlbach	46°51’36.7" N 11°59’9.5" E	1293 m	174/60	in leicht diskordantem Gang im Schiefer neben Intrusion, stark geschiefert	"	x
FH45	Mühlbach	46°51’41.5" N 11°58’10.4" E	1315 m	–	Pegmatitlage in Anatexit, Schieferung geht quer über Faltung von Anatexit	", kurz vor Hof	a, b
FH46	Uttenheim	46°52’13.7" N 11°56’21.7" E	1043 m	174/60	grobkörniger Pegmatit mit viel HlGl & Turmalin	"	–
FH47	Uttenheim	46°52’10.4" N 11°56’23.9" E	1054 m	–	recht grober, stark geschieferter Pegmatit mit Qz-Gang	", direkt nach B2	–
FH48	Putzenhöhe	46°51’46.3" N 11°51’45.6" E	2319 m	lose	leicht geschieferter Pegmatit mit großem Granat	letzter Anstieg zum Gipfel	–
FH49	Putzenhöhe	46°51’46.3" N 11°51’45.6" E	2319 m	lose	schwach geschieferter, grober Pegmatit mit Qz-Band	"	–
FH50	Putzenhöhe	46°51’49.3" N 11°51’47.1" E	2385 m	lose	riesenkörniger, zerbrochner Fsp-reicher Pegmatit	"	x
FH51	Putzenhöhe	46°51’53.1" N 11°51’52.1" E	2436 m	lose	feinkörniger (schwach geschiefert) mit Übergang zu grobkörnigem (ungeschiefert) Pegmatit	Ostgrat	–

Sample	Locality	Coordinates	Elevation	Orientation	Description	Outcrop	Thin sections
FH52	Putzenhöhe	46°51’52.5" N 11°51’52.1" E	2418 m	lose	?oligozäner Gang? An Übergang zu Pegmatit und Gneis	"	–
FH53	Putzenhöhe	46°51’52,5" N 11^{circ}51’52,1" E	2418 m	lose	gut foliierter Pegmatit mit großem Granat	"	–
FH54	Putzenhöhe	46°51’51,8" N 11^{circ}52’2,1" E	2422 m	lose	feinkörniger Gang	"	–
FH55	Putzenhöhe	46°51’52,6" N 11^{circ}52’4,1" E	2421 m	lose	Paragneis an Kontakt zu Pegmatit, mit Qz-Gang	"	–
FH56	Putzenhöhe	46°51’52,6" N 11^{circ}52’4,1" E	2421 m	lose	Paragneis, lagig, mit Falte	"	–
FH57	Putzenhöhe	46°51’49" N 11^{circ}56’23,9" E	2360 m	lose	mylonitischer Pegmatit mit Qz-Gängen	"	–
FH58	Putzenhöhe	46°51’45,1" N 11^{circ}51’45,3" E	2257 m	lose	Granat-Aggregat in Pegmatit	letzter Anstieg zum Gipfel	–
FH59	Putzenhöhe	46°51’37" N 11^{circ}51’33,5" E	2257 m	lose	Paragneis mit Pegmatitband (parallel zu S1), verfaltet und 2. Schieferung & Turmalin (im Gneis!)	direkt südlich des Grünbachsees	–
FH60	Putzenhöhe	46°51’37" N 11°51’33.5" E	2257 m	lose	foliierter Pegmatit	"	–
FH61	Bruggalm	46°53’7,7" N 11^{circ}54’19,8" E	1472 m	lose	foliierter Pegmatit mit Granat & Kontakt	Waldweg	a, b
FH62	Bruggalm	46°53’7,7" N 11^{circ}54’19,8" E	1472 m	lose	foliierter Pegmatit mit Granatschlieren	"	a, b
FH63	Bruggalm	46°53’7,7" N 11^{circ}54’19,8" E	1472 m	lose	nicht foliierter Pegmatit mit Turmalin & Granat	"	
FH64	Bruggalm	46°53’7,7" N 11^{circ}54’19,8" E	1472 m	lose	oligozäner Gang mit Qz-Gang	"	–
FH65	Bruggalm	46°53’6,8" N 11^{circ}54’20,2" E	1523 m	lose	helles geschiefertes Gestein, verwittert recht porös	"	–
FH66	Bruggalm	46°53’6,8" N 11°54’20,2" E	1523 m	lose	Pegmatitgang mit Faltung im Nebengestein	"	–
FH67	Bruggalm	46°53’6,4" N 11°54’18,9" E	1493 m	lose	foliierter Pegmatit mit einer gröberen Lage	"	–
FH68	Bruggalm	46°53’3,6" N 11°54’18,3" E	1548 m	lose	?anatektischer? Gneis mit Biotit	Fahrweg westlich der Bruggalm	–
FH69	Bruggalm	46°53’3,5" N 11°54’18,2" E	1535 m	lose	Pegmatit mit Turmalin, ohne Schieferung	"	–
FH70	Bruggalm	46°52’47,7" N 11°54’19,8" E	1686 m	124/48	Pegmatit aus Scherzone	"	–
FH82	Bruggalm	46°53’8,7" N 11°54’18,8" E	1472 m	lose	deformierter Pegmatitgang	Waldweg	–
FH83	Bruggalm	46°53’8,7" N 11°54’18,8" E	1472 m	lose	grünlicher Schiefer	"	x
FH84	Putzenhöhe	46°51’53,2" N 11°51’25,6" E	2339 m	182/58	foliierter Pegmatit	Westgrat	–
FH85	Putzenhöhe	46°51’52,1" N 11°51’17,6" E	2348 m	170/88	grober, foliierter Pegmatit mit starker Phasentrennung	"	–
FH86	Putzenhöhe	46°51’51,5" N 11°51’14,4" E	2367 m	348/78	foliierter Pegmatit mit Granat	"	–
FH87	Putzenhöhe	46°51’54,4" N 11°51’2,6" E	2367 m	lose	deutliche SPO von Qz/Fsp-Aggr, aber keine penetrative Schieferung ???	"	–

Sample	Locality	Coordinates	Elevation	Orientation	Description	Outcrop	Thin sections
FH88	Putzenhöhe	46°51’57,1" N 11°50’57,6" E	2367 m	lose	2 Bereiche: 1x stark geschiefert ? Recht dunkel und 1x grob und ohne Foliation, vllt Scherzone	"	–
FH89	Putzenhöhe	46°51’57,9" N 11°50’56,4" E	2361 m	lose	foliierter Pegmatit mit starker Phasentrennung	"	–
FH90	Putzenhöhe	46°51’59.8" N 11°50’50" E	2358 m	lose	sehr heller, fein bis kaum foliierter Pegmatit mit Granat	"	b
FH91	Putzenhöhe	46°52’3.1" N 11°50’45.3" E	2322 m	140/38	dunkler Schiefer mit Kontakt zu foliiertem Pegmatit oder hellem Schiefer ???	"	x
FH92	Putzenhöhe	46°52’5.2" N 11°50’44.7" E	2324 m	lose	fein foliierter Pegmatit, recht hell	"	–
FH93	Putzenhöhe	46°52’5.2" N 11°50’44.8" E	2322 m	lose	stark foliierter Pegmatit, aber schwache Lineation	"	–
FH94	Putzenhöhe	46°52’8.2" N 11°50’42.5" E	2310 m	lose	foliierter Pegmatit mit starker Lineation	"	a
FH97	Mutenock	46°51’44,3" N 11°49’39,2" E	2141 m	–	schwach foliierter Pegmatit	Felswand nördlich des eingezäunten Bereiches	–
FH98	Mutenock	46°51’45,3" N 11°49’41,2" E	2168 m	–	grober, an manchen stellen geschieferter Pegmatit, Lineation auf glimmerreichen Flächen	Felswand nördlich des eingezäunten Bereiches	–
FH99	Mutenock	46°51’38,9" N 11°49’27,6" E	2186 m	–	dunkler, leicht grünlicher Schiefer mit faserigem Mineral	westliche Steilstufe	–
FH100	Mutenock	46°51’35,8" N 11°49’20,7" E	2217 m	350/84	Quarzit/Paragneis	"	–
FH101	Mutenock	46°51’35,8" N 11°49’20,7" E	2217 m	352/88	foliierter, recht dunkkler Pegmatit mit Turmalin	"	–
FH102	Mutenock	46°51’39" N 11°49’18,2" E	2215 m	lose	sehr schwach foliierter Pegmatit	"	–
FH103	Mutenock	46°51’42,9" N 11°49’19,2" E	2216 m	348/79	stark foliierter Pegmatit (oder Quarzit???), mit grünlichen Qz-Aggr. und Kontakt zu dunklem Schiefer	"	–
FH104	Mutenock	46°51’42,9" N 11°49’19,2" E	2216 m	–	foliierter Pegmatit	"	–
FH105	Bruggalm	46°53’4,2" N 11°54’2,7" E	1697 m	290/34 L: 217/11	schwach foliierter, heller Pegmatit mit deutlicher Lineation, als 3 cm dicke Lage in Paragneis	Fahrweg westlich der unteren Bruggalm	x
FH106	Bruggalm	46°53’4,2" N 11°54’2,7" E	1697 m	324/36 L: 54/7	feinkörniger, heller Pegmatit, als dünne Lage (7-10 mm) konkordant in Paragneis	"	–
FH107	Bruggalm	46°53’4,2" N 11°54’2,7" E	1697 m	–	massiger Pegmatit aus dicker Lage (10 cm) in Gneis	"	–
FH108	Bruggalm	46°53’4,2" N 11°54’2,7" E	1697 m	–	Pegmatitlage (2 cm) in Paragneis, leicht verfaltet	"	–
FH109	Bruggalm	46°53’4,2" N 11°54’2,7" E	1697 m	–	massiger Pegmatit mit geschiefertem Nebengestein	"	–
FH110	Bruggalm	46°53’4,2" N 11°54’2,7" E	1697 m	–	massiger Pegmatit mit geschiefertem Nebengestein	"	–
FH111	Bruggalm	46°53’4,2" N 11°54’2,7" E	1697 m	–	lokaler Scherkörper: foliierter Pegmatit	"	–
FH120	Weitental	46°51’12.0" N 11°42’48.6" E	1447 m	356/25, Scherband: 32/80	Pegmatit, direkt aus Scherkörper	erster Aufschluss, Scherzone & Quelle	–
FH121	Weitental	46°51’12.0" N 11°42’48.6" E	1447 m	–	Paragneis mit Qz-Gang & Scherband	"	x
FH122	Weitental	46°51’12.0" N 11°42’48.6" E	1447 m	–	Pegmatit, direkt an Kontakt zu Scherband	"	x
FH123	Weitental	46°51’12.0" N 11°42’48.6" E	1447 m	48/50	angrenzender Gneis in Scherband	"	a, b
FH124	Weitental	46°51’12.6" N 11°42’50.2" E	1448 m	265/5 L: 65/5	Pegmatit	10 m rechts von Quelle	a, b

Sample	Locality	Coordinates	Elevation	Orientation	Description	Outcrop	Thin sections
FH125	Weitental-Süd	46°50'52.0" N 11°42'30.5" E	1413 m	–	mylonitischer Pegmatit	–	x
FH126	Weitental-Süd	46°50'52.0" N 11°42'30.5" E	1413 m	315/45	mylonitischer Pegmatit	–	x
FH127	Weitental-Süd	46°50'42.7" N 11°42'20.1" E	1379 m	–	mylonitischer Pegmatit	"	–
FH128	Weitental-Süd	46°50'40.9" N 11°42'46.1" E	1204 m	–	mylonitischer Pegmatit	"	x
FH129	Weitental-Ost	46°51'3.9" N 11°44'0.5" E	1129 m	–	Mylonit	"	a, b, c
FH130	Weitental-Ost	46°51'3.9" N 11°44'0.5" E	1129 m	–	Mylonit	"	a, b
CT599	Vals	46°52'33" N 11°37'28" E	–	–	Pegmatit mit Turmalin	–	a, b, c
KD75	Sambock	46°51'37.9" N 11°53'49.3" E	2351 m	–	stark geschieferter Pegmatit	–	a, TEM
UP3	Uttenheim	46°52'27.2" N 11°56'0.4" E	–	–	grobkörniger Pegmatit mit Turmalin	–	x

A2 Overview of the pegmatites' microstructure

Sample	Locality	Coordinates	Modal analysis	Mode of clasts	Fsp. matrix microstructure	Quartz microstructure
CT599	Vals	46°52'33" N 11°37'28" E	Qz: 10 %, Ab: 60 %, Kfs: 20 %, Trm: 10 %, Ms: < 1 %	Ab: 20 % Kfs: 80 %	Type B (long axis 35 μm, aspect ratio $\sim$ 2.3)	layers, several mm long, grain size < 20 μm
KD75	Sambock	46°51'37.9" N 11°53'49.3" E	Qz: 20 %, Ab: 65 %, Kfs: 15 %, Ms: 5 %	Ab: 20 % Kfs: 80 %	Type A (grain diameter $\sim$ 10 μm)	layers, several mm long, grain size $\sim$ 50 μm
UP3	Uttenheim	46°52'27.2" N 11°56'0.4" E	Qz: 10 %, Ab: 80 %, Kfs: 5 %, Trm: 5 %, Ms: < 1 %	Ab: 90 % Kfs: 10 %	Type A (grain diameter 17 μm)	irregular aggregates; grain size 100s of μm, sutured grain boundaries, long (10 μm), straight segments
FH1	Sambock	46°51'15.8" N 11°53'43.7" E	Qz: 30 %, Ab: 50 %, Kfs: 5 %, Ms: 15 %	Ab: 90 % Kfs: 10 %	no fsp matrix developed	irregularly aggregates, grain size 30–300 μm, sutured grain boundaries, undulous extinction
FH4	Uttenheim	46°52'12.2" N 11°56'22.6" E	Qz: 50 %, Ab: 50 %	Ab: 100 % Kfs: 0 %	no fsp matrix developed	isolated grains (50–150 μm)
FH5	Uttenheim-Süd	46°52'26.2" N 11°56'0.8" E	Qz: 15 %, Ab: 55 %, Kfs: 25 %, Ms: 5 %	Ab: 50 % Kfs: 50 %	Type A (grain diameter 15 μm)	irregular aggregates; grain size 100s of μm, sutured grain boundaries, long (10 μm), straight segments
FH9	Uttenheim	46°52'12.2" N 11°56'22.6" E	Qz: 15 %, Ab: 50 %, Kfs: 30 %, Ms: 5 %	Ab: 50 % Kfs: 50 %	intermediate (long axis 32 μm, aspect ratio 1.1–1.8)	irregular aggregates, grain size 30–400 μm, sutured grain boundaries, undulous extinction
FH10	Mühlbach	46°50'48.5" N 11°58'24.7" E	Qz: 30 %, Ab: 45 %, Kfs: 15 %, Ms: 10 %	Ab: 65 % Kfs: 35 %	intermediate (long axis 26 μm, aspect ratio 1–2)	irregular aggregates, grain size 30–400 μm, sutured grain boundaries, undulous extinction
FH13	Eidechs-spitze	46°52'12.7" N 11°45'33.6" E	Qz: 10 %, Ab: 80 %, Kfs: 10 %, Ms: <1 %	Ab: 85 % Kfs: 15 %	Type B (long axis 37 μm, aspect ratio $\sim$ 2.1)	layers, recrystallized grains < 20μm in diameter and $\sim$ 5 μm in shear bands
FH14	Plattneralm/ Pfunders	46°52'56.9" N 11°43'48.9" E	Qz: 30 %, Ab: 30 %, Kfs: 30 %, Ms: 10 %	Ab: 20 % Kfs: 80 %	no fsp matrix developed	layers; < 1mm long; grain size 20–300 μm, suture grain boundaries
FH21	Sambock	46°51'31,9" N 11°53'48.2" E	Qz: 15 %, Ab: 65 %, Kfs: 15 %, Ms: 5 %	Ab: 85 % Kfs: 15 %	Type B (long axis 31 μm, aspect ratio $\sim$ 2.1)	irregular aggregates, grain size 30–500 μm, sutured grain boundaries, undulous extinction
FH27	Weitental	46°51'13.0" N 11°42'52.1" E	Qz: 20 %, Ab: 650 %, Kfs: 5 %, Ms: 10 %	Ab: 95 % Kfs: 5 %	Type B (long axis 36 μm, aspect ratio $\sim$ 2.3)	layers, several mm long and 20–30 μm wide, recrystallized grains < 20μm in diameter and $\approx$ 5 μm in shear bands and along fractures
FH30	Weitental	46°51'20.8" N 11°42'55.5" E	Qz: 30 %, Ab: 40 %, Kfs: 20 %, Ms: 10 %	Ab: 50 % Kfs: 50 %	Type B (long axis 32 μm, aspect ratio $\sim$ 1.9)	irregular aggregates, grain size 30–300 μm, sutured grain boundaries, undulous extinction
FH39	Weitental	46°51'15" N 11°42'54.7" E	Qz: 10 %, Ab: 55 %, Kfs: 25 %, Ms: 10 %	Ab: 30 % Kfs: 70 %	Type B (long axis 30 μm, aspect ratio $\sim$ 2.2)	layers, several mm long, few tens of μm wide, recrystallized grains < 20μm in diameter

Sample	Locality	Coordinates	Modal analysis	Mode of clasts	Fsp. matrix microstructure	Quartz microstructure
FH44	Mühlbach	46°51'36.7" N 11°59'9.5" E	Qz: 30 %, Ab: 60 %, Kfs: 5 %, Ms: 5 %	Ab: 90 % Kfs: 10 %	no fsp matrix developed	irregular aggregates, grain size 30–300 μm, sutured grain boundaries, undulous extinction
FH45	Mühlbach	46°51'41.5" N 11°58'10.4" E	Qz: 15 %, Ab: 80 %, Kfs: 5 %, Ms: $<$ 1 %	Ab: 5 % Kfs: 95 %	no fsp matrix developed	irregular aggregates, grain size 30–500 μm, sutured grain boundaries, undulous extinction
FH47	Uttenheim	46°52'10.4" N 11°56'23.9" E	Qz: 30 %, Ab: 40 %, Kfs: 20 %, Ms: 10 %	Ab: 55 % Kfs: 45 %	Type A (grain diameter 18 μm)	irregular aggregates; coarse grained (400 μm), sutured grain boundaries with 10 μm long, straight segments
FH60	Putzenhöhe	46°51'37" N 11°51'33.5" E	Qz: 15 %, Ab: 65 %, Kfs: 10 %, Ms: 10 %	Ab: 75 % Kfs: 25 %	Type A (grain diameter 20 μm)	layers, $<$ 1mm long, grain size 50–300 μm, sutured grain boundaries
FH90	Putzenhöhe	46°51'59.8" N 11°50'50" E	Qz: 10 %, Ab: 60 %, Kfs: 20 %, Ms: 10 %	Ab: 60 % Kfs: 40 %	no fsp matrix developed	layers; $<$ 1mm long, grain size 50–300 μm, sutured grain boundaries
FH94	Putzenhöhe	46°52'8.2" N 11°50'42.5" E	Qz: 20 %, Ab: 50 %, Kfs: 25 %, Ms: 5 %	Ab: 35 % Kfs: 65 %	intermediate (long axis 27 μm, aspect ratio 1–1.7)	layers; $<$ 1mm long, grain size 50 – 300 μm, $\sim$ 10 μm in shear bands

A3 Conditions of electron microprobe measurements and chemical dating presented in chapter 6

Element	Standard	Line	Monazite 15 kV, 200 nA	Allanite 15 kV, 20 nA	Xenotime 15 kV, 200 nA	Thorite 15 kV, 150 nA	Apatite 15 kV, 20 nA
Si	Rhodonite	Kα	240 s	60 s	160/240 s	80 s	60 s
Al	$Y_3Al_5O_{12}$	Kα	–	60 s	–	–	–
Fe	Hematite	Kα	–	60 s	–	–	60 s
Mn	Rhodonite	Kα	–	60 s	–	–	80 s
Na	Albite	Kα	–	–	–	–	60 s
Ca	Apatite	Kα	60 s	60 s	120 s	100 s	40 s
P	Apatite	Kα	60 s	–	40/20 s	100 s	40 s
F	CaF_2	Kα	–	–	–	–	40 s
S	ZnS	Kα	160 s	–	120 s	–	120 s
Cl	Tugtupite	Kα	–	–	–	–	80 s
As	GaAs	Lα	160 s	–	160 s	–	80 s
Mg	MgO	Kα	–	80 s	–	–	–
Sr	Celestine	Lα	–	100 s	–	–	100 s
Ti	TiO_2	Kα	–	80 s	–	–	–
Th	ThO_2	Mα	160 s	100 s	160/300 s	20 s	80 s
U	UO_2	Mβ	300 s	100 s	160 s	20 s	80 s
Pb	Crocoite	Mβ	480 s	100 s	360/480 s	300 s	80 s
Y	YPO_4	Lα	160 s	200 s	40/20 s	120 s	120 s
La	$LaPO_4$	Lα	350 s	80 s	–	–	120 s
Ce	$CePO_4$	Lα	350 s	80 s	–	100 s	100 s
Pr	$PrPO_4$	Lβ	350 s	80 s	–	–	100 s
Nd	$NdPO_4$	Lα	350 s	80 s	350/220 s	–	100 s
Sm	$SmPO_4$	Lβ	350 s	80 s	60/80 s	–	100 s
Gd	$GdPO_4$	Lβ	350 s	80 s	60/80 s	100 s	–
Dy	$DyPO_4$	Lα	–	–	60/80 s	100 s	–
Ho	$HoPO_4$	Lβ	–	–	120 s	–	–
Er	$ErPO_4$	Lα	–	–	60/80 s	–	–
Yb	$YbPO_4$	Lα	–	–	60/80 s	–	–

Acknowledgements

Foremost, I want to thank my supervisor Claudia Trepmann for the initiation of this project and the many hours she spent discussing important issues in the field and at the university. She was an immense help during the evaluation of my results and writing of this thesis.

Many thanks go to Emilie Janots, whose knowledge of metamorphic reactions and the behavior of REE helped especially with my work on corona structures. She helped understanding many issues in the field and was always open for questions, even though she worked only partly in Munich during the time of my thesis.

Valérie Magnin is greatly acknowledged for doing most of the microprobe analysis and age calculations of xenotime and monazite, together with Emilie Janots. I thank Pierre Lanari for his important help dating allanite with the ICP-MS at the university of Bern. Namvar Jahanmehr is acknowledged for preparing many thin sections. Special thanks go to Patrick Eschenbacher and Dominique Mackensen for helping me with fieldwork.

I want to thank my colleagues Lina Seybold, Alex Reul, Benedikt Röska, Korbinian Schiebel, Kristian Bader and many more, who provided many great moments of distraction from my work.

Lastly, I want to thank my other friends, especially Giustina, and all members of my family for giving me all the necessary support during the last four years.